Michael Rudolf Henzinger

Bedding of segmental linings at hard rock TBM tunnels

Doctoral Thesis

Department of Civil Engineering

Graz University of Technology

Reviewers:

Em.Univ.-Prof. Dipl.-Ing. Dr.mont. Wulf Schubert

Institute of Rock Mechanics and Tunnelling

Graz University of Technology

Professor Dr. Giovanni Barla

Former Professor of Rock Mechanics

Politecnico di Torino, Italy

Graz, March 2019

Affidavit

I declare that I have authored this thesis independently, that I have not used other than the declared sources/resources, and that I have explicitly indicated all material which has been quoted either literally or by content from the sources used. The text document uploaded to TUGRAZonline is identical to the present doctoral thesis.

Date

Signature

Dedicated to my Parents.

Bei der Durchführung selbst regieren dann naturgemäß Meister und Mineure, denn sie sind die einzigen, die einige Erfahrung besitzen. Ist nun bei diesen Leuten einer dabei, der im Tunnelbau (nicht im Bergbau) grau geworden ist, so geht meist alles gut, denn er ersetzt durch sein Gefühl für den Berg und seine Bauerfahrung das, was in dem ganzen Gebäude fehlt, nämlich die Zusammenarbeit der einzelnen Fachgruppen.

L. v. Rabcewicz

Acknowledgements

I assumed this section is to be by far the easiest to write – I have been proven wrong. Remembering the last five years, I realize what I experienced, what I learned and what a great time I had.

The person who gave me the chance to proof myself and trusted me is Prof. Dr. Wulf Schubert, the head of the Institute of Rock Mechanics and Tunnelling during my employment. I went into his office asking if there is a doctoral position available at the Institute. The response was as precise as short that there is a job opening in a couple of months. After having mixed feelings I applied for the mentioned position and was prepared for some hard time job interview but it turned out to be a comfortable talk between two like-minded individuals. The only question I still remember was if I still want to do a doctoral thesis. The answer was obviously yes. At that time I didn't know what I was getting into. With his capability to cope with my temper he managed to trigger ambitiousness I wasn't aware of. Not a single day passed at the Institute which I didn't enjoy. Thank you Wulf!

Prof. Dr. Giovanni Barla was of great importance, not only due to his great tunnelling competence but also due to his empathy. He also made life for me a lot easier by being present at numerous conferences giving me the chance of meeting him on a regular basis. Because of him I experienced additional confidence during my thesis. Thank You.

I cannot overstress the importance of Dr. Nedim Radončić, a former doctoral student at the Institute of Rock Mechanics and Tunnelling. It was during the preparation of my master thesis at the Koralmtunnel in 2013, when I accidentally slipped and lost equilibrium during the inspection of the TBM cutterhead. After a short slide, I landed softly on the geotechnical supervisor of the Koralmtunnel, Nedim. It was the beginning of an excellent friendship. Rado, thanks.

Manuel Lagger has the ability to cope with my daily moods when I am under a ridiculous amount of stress and giving me the encouragement to finish my thesis by saying the right things at the right time. When only talking wasn't enough, he always took his time for an after-work conversation/beer at Rosi's. Being the first student writing a thesis under my supervision, he demonstrated great patience giving me the ability to improve my supervising capabilities.

Bujinski (alias Andreas Buyer) has proven to be an excellent colleague and counterpart (in terms of work place alignment) being able to start every day with a smile. I admire him for his capabilities of managing to be a great father, great programmer (whatever language you name) and a great friend at the same time.

The head of our Laboratory, Dr. Manfred Blümel supported me at every step during

my laboratory testing programme with his inside knowledge.

Solid as a rock has been the friendship with Sabsi and Kuchn (alias Sabrina Gollmayr and Michael Kiechl). They have shown me the greatest loyalty and patience in their friendship whenever I needed them. Thanks!

Magdalena Gogl, a former high school classmate of mine, turned out to be my central contact point for talking about blunders and other awkward experiences. She never hesitated to make fun of me. At the same time she cheered me up and helped through every tough situation with the right amount of beer. Thank you.

To all those friends and companions which couldn't be mentioned at this point, I would like to express my deepest gratitude for all the beautiful moments, mountaineering experiences, trips and evenings. Especially to the one person who gave me hope for a silver lining during the final stage of my thesis, I owe you my sincerest admiration, respect and gratitude. With your help I was able to tackle difficult tasks, both in the Alps and in my thesis. Through you I experienced true joy that lasts. THANK YOU!

My deepest gratitude goes to my Family. They have always given me their tireless and undoubting support throughout my life. My father, an immensely experienced geotechnical engineer has taught me the practical approaches for geotechnics and always had an open ear for my problems, both professionally and personally. My mother and sister taught me that there is more in life besides being excellent teachers. Not a single day has passed, where I didn't enjoy the feeling having a family like mine.

Grinzens, March 2019 Michael Henzinger

Abstract

The use of lining segments at TBM shield driven tunnels represents the state-of-the-art in both alpine and shallow tunnels. These are used regardless of the ground type. Due to the advanced state of development and the relatively simple manufacturability, segments usually consist of a reinforced concrete construction. The design of the segments is based on simple numerical models, taking simplified external load assumptions into account. In contrast, the backfill material receives only little attention. The backfill serves as load transfer medium between the surrounding rock mass and the segmental lining. Usually a cement suspension or a pea gravel/pea gravel–mortar mixture is used, depending on the ground condition.

The present thesis focuses on the application of pea gravel as bedding material between the rock mass and the segmental lining. In particular, the area of the segmental lining behind the shield tail is observed. Due to the relocation behaviour of pea gravel, an unfavourable bedding situation is triggered, which must be taken into account during the design of the segmental lining.

In the first part of this thesis, the deformation and relocation behaviour of pea gravel, both in laboratory tests and analogue models on the construction site as well as on site situation within the annular gap is investigated. The tests provide valuable information on the elastoplastic behaviour of pea gravel and on the relocation behaviour as well as on the actual distribution within the annular gap behind the shield tail.

In a further part deformation measurements of installed rings of segments are systematically evaluated in order to draw conclusions on the deformation characteristic after leaving the shield tail. Here, different rock mass types are considered separately.

In the third part, two different concepts for improving the bedding situation of the lining segments after leaving the shield tail are presented. One of these systems is tested as a bedding improvement measure at a current tunnel project. With the help of the known deformation characteristics and evaluation methodology of the displacement measurements described in the previous part, the bedding effect is depicted.

In the final part of the thesis a numerical study is conducted with the aim to confirm the deformation behaviour of the segments with and without bedding improvement measures. In the used model, the relevant rock mass and support parameters, excavation processes and construction components used are considered in order to obtain the most realistic possible results.

Kurzfassung

Der Einsatz von Tübbingen zur Ausbruchssicherung bei Schildvortrieben stellt sowohl im alpinen Einsatz, als auch bei seichtliegenden Tunnelbauwerken den Stand der Technik dar. Diese werden unabhängig von der Art des Baugrundes verwendet. Auf Grund des fortgeschrittenen Entwicklungsstandes und der relativ einfachen Herstellbarkeit bestehen Tübbinge zumeist aus einer bewehrten Betonkonstruktion. Die Bemessung der Tübbinge beruht auf einfachen numerischen Modellen, unter Berücksichtigung von vereinfachten äußeren Lastannahmen. Dem Hinterfüllmaterial, welches den Kontakt zwischen Gebirge und Auskleidung gewährleisten soll, wird nur wenig Aufmerksamkeit geschenkt. Die Ringspaltverfüllung besteht aus einer Zementsuspension oder einem Perlkies/Perlkies–Mörtel Gemisch, abhängig vom Baugrund.

Die vorliegende Arbeit konzentriert sich auf den Einsatz von Perlkies als Bettungsmaterial zwischen Gebirge und Ausbau. Im Speziellen steht der Bereich des Tübbingausbaus nach Verlassen des Schildschwanzes im Fokus. Auf Grund des Umlagerungsverhaltens von Perlkies kommt es zu einem teilgebetteten Zustand, welcher bei der Bemessung des Tübbingausbaus berücksichtigt werden muss.

Im ersten Teil der Arbeit wird das Verformungs- und Umlagerungsverhalten von Perlkies, sowohl mittels Laborversuchen und Analogmodellen auf der Baustelle, als auch im eingebauten Zustand im Tunnel untersucht. Die Versuche liefern einerseits wertvolle Informationen zum elastoplastischen Verhalten von Perlkies und andererseits zum Umlagerungsprozess, sowie zur tatsächlichen Verteilung im Ringspalt hinter dem Schildschwanz.

In einem weiteren Teil werden Veschiebungsmessungen von Tübbingringen systematisch ausgewertet, um eine Aussage über die typische Verformungscharakteristik nach Verlassen des Schildschwanzes treffen zu können. Hierbei werden unterschiedliche Gebirgstypen getrennt betrachtet.

Im dritten Teil werden zwei unterschiedliche Konzepte zur Verbesserung der Bettung der Tübbinge nach Verlassen des Schildschwanzes vorgestellt. Eines dieser Systeme kommt bereits testweise als bettungsverbessernde Maßnahme an einem aktuellen Tunnelprojekt zum Einsatz. Mit Hilfe der im vorhergehenden Teil beschriebenen Verformungscharakteristik und Auswertemethodik der Verschiebemessungen wird der Bettungserfolg aufgezeigt.

Im letzten Teil der Arbeit wird eine Numerikstudie mit dem Ziel, die Verformung der Tübbinge mit und ohne bettungsverbessernde Maßnahmen zu ermitteln durchgeführt. Im verwendeten Modell werden die relevanten Gebirgs- und Ausbauparameter, Vortriebsprozesse und verwendeten Bauelemente berücksichtigt, um möglichst realistische Ergebnisse zu erzielen.

Contents

1 Introduction

During the last century the number of mechanized driven tunnels in rock masses with high overburden significantly increased for infrastructure projects with large excavation diameters. Prior to this development, tunnel boring machines have been successfully applied at hydropower projects with smaller dimensions under hard rock conditions. Due to their increasing level of automation and the capability of higher advance rates, tunnel boring machines seem to provide a competent advance method for large projects with simple geometries.

With shielded tunnel boring machines, the support behind the shield consists of two major elements. The segmental lining and the backfill of the annular gap. In collaboration, they have to support the surrounding rock mass and provide a stable bearing structure for the tunnel boring machine. The lining segments usually consist of precast reinforced concrete elements. Recent developments have shown that using fibre reinforced concrete could be a promising alternative for these elements. In hard rock conditions the annular gap is usually backfilled with a fine grained and closely graded material referred to as “pea gravel”. Pea gravel serves as a load transfer medium between the rock mass and the segmental lining. Since the segmental lining is not self bearing, a complete backfill is of upmost importance for proper support action and the stability of the excavation.

In order to overcome bedding deficiencies within the annular gap during the excavation procedure, a relatively high amount of reinforcement is required. It has been noted that due to its deformational behaviour, pea gravel forms a distinct cone behind the shield tail. This effect is even more pronounced when double shielded tunnel boring machines are applied due to the sudden regripping process after a boring stroke has been completed. Hence, a mostly unknown and unfavourable bedding situation has to be accounted for within the first segment rings behind the shield tail. This thesis deals with the investigation of this bedding situation, the mechanical properties of pea gravel and various methods to improve the bedding.

2 Overview of the State of the art and Objectives

To understand the importance of the bedding of segmental linings, an overview of the components of the support as well as procedural influences of shielded tunnel boring machines is hereinafter provided. Evaluating and summarizing existing approaches, knowledge and findings to investigate the bedding situation in hard rock conditions shall provide an overview of the state of the art. Existing design improvements with due attention given to an unfavourable bedding condition will be evaluated regarding their applicability for the given situation. A clear differentiation with respect to prior research will be presented. Based on the state of the art, a definition of objectives is possible and the cornerstone for the discussion of the findings presented in this thesis is given. The review of the state of the art will address following aspects:

1. The description of a shielded excavation tunnel advance.
2. The interaction of the support and the rock mass.
3. Summary of design concepts to improve the described shortcomings regarding the immediate bedding of the segmental lining.
4. Overview of analytical and numerical approaches to evaluate the system behaviour.

2.1 Structural features of a hard rock TBM driven excavation with segmental lining

Depending on the excavation method, the support system and the manageable ground conditions, tunnel boring machines are classified into individual types. Due to the individual terminology which has been used over the years for similar principles, the nomenclature used in this thesis is based on the classification given in the following Austrian Standards and Guidelines:

- ÖNORM B 2203-2 (2005),
- Richtlinie Schildvortrieb (2009) and
- Richtlinie für die geotechnische Planung von Untertagebauten mit kontinuierlichem Vortrieb (2013)

Figure 1 illustrates the different types of tunnel boring machines. Since this thesis

focuses on the bedding of lining segments under hard rock conditions, the Single Shield TBM and the Double Shield TBM which fulfill this condition, have been highlighted.

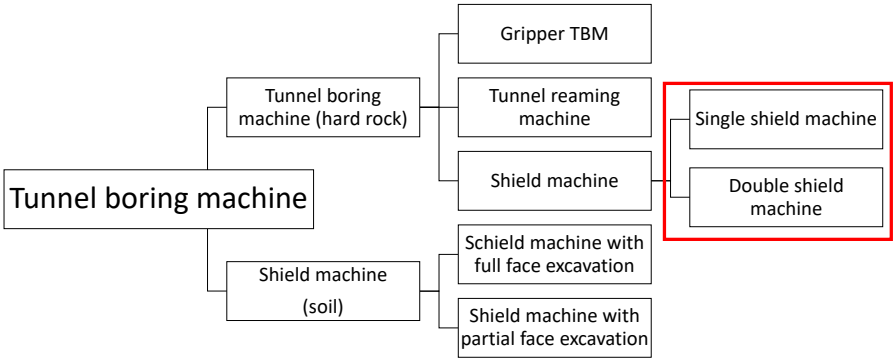

Figure 1: Classification of tunnel boring machines.

For full face excavation under hard rock conditions the Gripper TBM, the Single Shield TBM and the Double Shield TBM can be used. The basic principle of tunnel boring machines was developed during the industrialisation mid 19th century. Due to the need for a nonhazardous excavation method, the Shield machine as we know it today, was introduced first by J. Price in 1896 for the excavation in soil. More than 50 years later James S. Robbins developed the first Gripper TBM. This was the first time the cutterhead was only equipped with disc cutters. Open type Gripper TBMs have their limitations in changing rock mass conditions. Especially in rock masses with the need for a high amount of support, the advance rate decreases. Hence, in 1972 Carlo Grandori invented the Double Shield TBM (⌀ 4.32 m) which should have overcome the disadvantages of a Gripper TBM. In 1980 the hard rock Shield TBM was introduced by converting a Gripper TBM to a Single Shield TBM (⌀ 11.5 m) with segmental lining (Maidl, 2008; Grandori & Antonini, 1994; Vigl et al., 1999).

While Double Shield TBMs have shown a good applicability for hydropower tunnels with diameters up to 6 m, they tend to become less reliable when used for tunnels with larger diameters. TOne of the reasons is the shield length (up to 2 diameters) leading to a large unsupported longitudinal span length with an increasing potential of shield jamming. Thus, when rock mass conditions do not allow the use of a Gripper TBM, Single Shield TBMs with its compact design and shorter shield length prove to be a suitable compromise between advance rates and unforeseen standstills.

Due to the steady development and improvement in TBM tunnelling, this advance method has proven to be a good alternative for conventional tunnelling as far as ground conditions allow it. Following advantages compared to conventional tun-

nelling can be mentioned:

- High degree of mechanisation.
- High excavation profile accuracy when stable ground conditions are encountered.
- Lower personnel expenditures.
- Higher advance rates possible.
- Increased safety especially with Shield TBMs.
- Installation of support during ongoing advance (Double Shield TBM).

2.1.1 Shielded hard rock TBMs

The basic principle of shielded hard rock TBMs is adopted from the application in soil. Despite the subordinate need for face support, the main difference is found in the used cutting tools mounted on the cutterhead. Under hard rock conditions the cutterhead is equipped with disc cutters which are pressed against the face and rolled in concentric tracks. While the cutterhead rotates, they break out chips from the tunnel face and a constant advance rate during the "boring" process is achieved.

2.1.1.1 Single Shield TBM

Single Shield TBMs (see Figure 2) are applicable for fractured rock masses where the use of Grippers is not possible. The shield extends from the cutterhead to the segmental lining and protects the workers, the main bearing and the thrust cylinders from disintegrating blocks. Furthermore, the segmental lining can be installed using erectors within the protection of the shield. Depending on the ground conditions, different segment types can be applied. While installing a full ring of segments, the advance is halted. The thrust force needed for the cutterhead advance is initiated by the main thrust cylinders pushing against the installed segmental lining.

2.1.1.2 Double Shield TBM

The Double Shield TBM (see Figure 3) can be applied under the same rock conditions as the Single Shield TBM with the limitation that due to the increased shield length, a longer stand-up time of the rock mass is required. The basic principle derives from the Single Shield TBMs with some adaptations. The shield consists of two parts, the Front Shield and Gripper Shield. Both of them are connected via the main thrust cylinders. The main advantage in comparison to the Single Shield TBM is the possibility of maintaining the advance during the installation of the

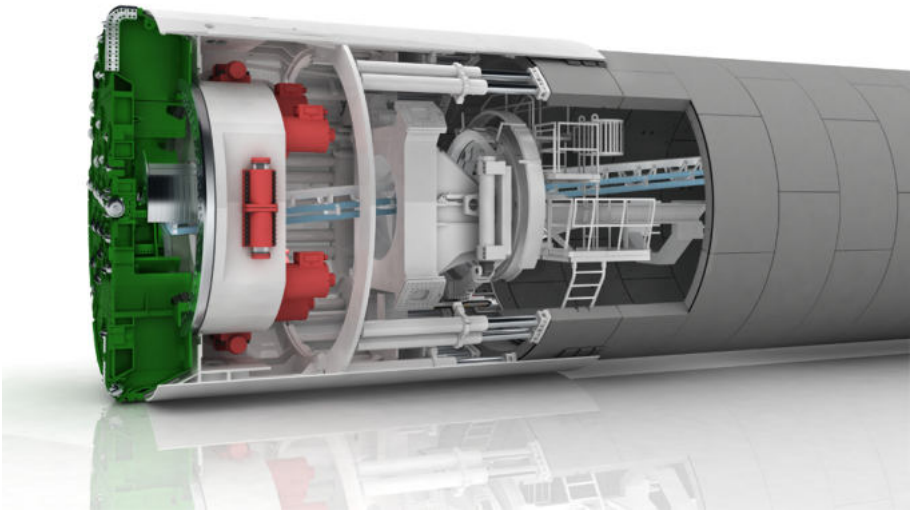

Figure 2: Shematic view of a Single Shield TBM (taken from Herrenknecht AG, 2012).

segmental lining, using the front thrust cylinders. This requires the Grippers to be extended. The only stand still during operation occurs during the regripping process, when the front cylinders have to be retracted. When the rock mass quality decreases, the TBM changes to Single Shield mode where only the auxiliary thrust cylinders are used to produce the necessary thrust force of the cutterhead. Hence, with good rock mass quality the TBM does not necessarily need lining segments .

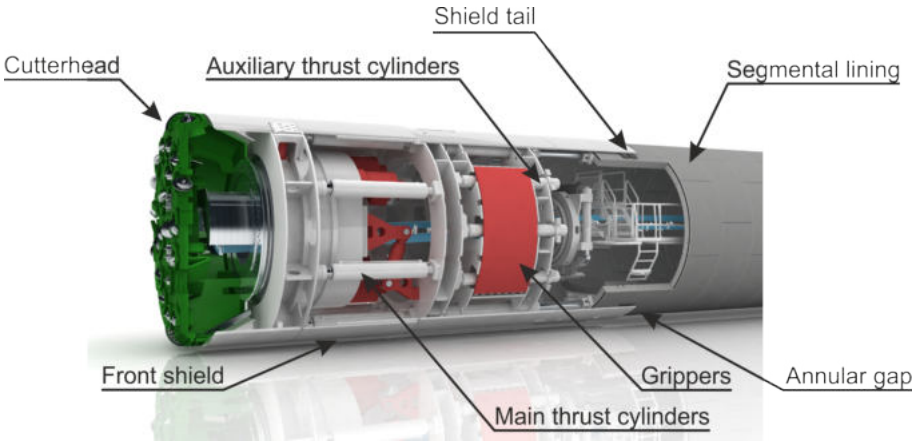

Figure 3: Shematic view of a Double Shield TBM (taken from Herrenknecht AG, 2012).

2.1.2 Support at Shield TBMs in hard rock

The support at Shield TBM driven tunnels under hard rock can be divided into three successive areas as shown in Figure 4.

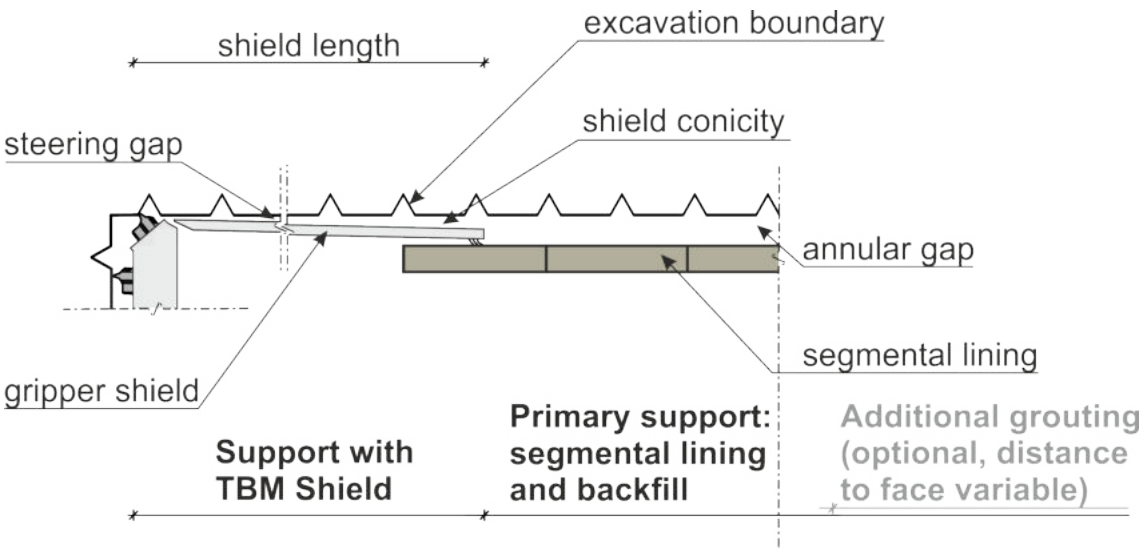

Figure 4: Schematic view of the support at Shield TBMs.

2.1.2.1 Support with the TBM Shield

The TBM shield is intended to protect the workers and the critical machinery parts from rock breaks outs. Since the shield reaches up to approx. 15 m in length, rock masses exhibiting large displacements can lead to contact between ground and shield. This results in high frictional forces which can exceed the maximum thrust force of the TBM. To avoid this effect, the size of the steering gap which is determined by the difference of the cutterhead radius and the Shield radius has to be chosen carefully. For short sections of high deformation potential, the cutterhead can be equipped with an overcut mechanism. By shifting the calibre disc cutters outwards, the diameter of the excavation profile can be increased to a limited extent.

2.1.2.2 Primary support – segmental lining and backfill

The primary support consists of two components. The segmental lining which is installed at the end of the shield and the backfill which is consequently placed in the free space between the segments and the rock mass. Together they act as primary support.

Segmental lining The segmental lining consists of several single lining segments. They are prefabricated either at the construction site or at a manufacturing plant. Thus, the encountered rock mass conditions have to be evaluated well before the excavation in order to be able to produce and install the proper support. Hence, the adaptability of the support to the encountered ground behaviour type is limited.

Segments can be made of steel, cast iron, steel reinforced concrete and steel fibre reinforced concrete. Lining segments are usually made of precast and reinforced

concrete due to its broad applicability and cheaper production (Wagner, 1964; Distelmeier, 1975).

Since the segmental lining is assembled by several segments forming individual rings with a length between 1 and 2 m, joints are formed at the contact areas between two segments. These can be differentiated in longitudinal joints (contact between two segments of the same ring) and radial joints (contact between different rings). The joints play a major role in the deformational behaviour of the support.

Requirements for the design, calculation and the production of reinforced lining segments in Austria are given in the Guideline for Concrete Segmental Lining System (2011).

Backfill For backfilling materials two different options are available, depending on the encountered ground conditions. When tunnelling in hard rock, the annular gap is usually filled with pea gravel or a mixture of pea gravel and mortar. Regulations regarding requirements of the bedding material can be found in ÖNORM EN 12620 (2014),. Furthermore, the Guideline for Concrete Segmental Lining System (2011) offers basic design rules for lining segments as well as information on the influence of different bedding materials.

The applied backfill has to embed the segmental lining into the surrounding ground and thus allow stress transfer. In addition, all loads resulting from uplift, thrust force and the weight of the TBM acting on the support have to be transferred into the surrounding ground. With shallow overburden, the support has to be immediately activated, as the segments leave the shield in order to limit surface settlements.

In competent rock masses the annular gap is usually filled with pea gravel. Grain size distributions between 4 and 16 mm are generally applicable. Nevertheless, practical applications have shown that a homogeneous bedding distribution can be improved by limiting the range from 8 to 11 mm (Guideline Concrete Segmental Lining System, 2011). In order to avoid blockages within the annular gap, the percentage of undersized grains should be kept below 10 %. During the TBM advance a relocation of pea gravel within the annular gap occurs, leading to an inhomogeneous bedding and stiffness distribution at the first rows of lining segments close to the shield. Due to the instantaneous advance of the TBM, several parallel acting working steps and limited time, a fully backfilled annular gap might not be established after every ring closure.

Pea gravel is pneumatically injected radially into the annular gap. Starting at the invert, the annular gap is filled stepwise up to the crown area. Due to the frictional resistance mortar is added in the invert area through ports in the shield.

When applying pea gravel in hard rock driven tunnels, following advantages arise compared to mortar:

- Immediate stable conditions since a load bearing grain structure is established immediately.
- Drainage of water bearing formations is established along the annular gap.
- Lower requirements on the shield tail sealing since the potential of pea gravel filling the gap between shield and ground is lower than with mortar. Hence, pea gravel does generally not bypass to the cutterhead through the steering gap.
- Pea gravel backfill is simple to execute and well proven for smaller shield diameters.
- No specific requirements for pea gravel when water bearing formations are encountered.

Nevertheless, the use of pea gravel bears some disadvantages, which have to be mentioned.

- The backfilling with pea gravel is under poor rock mass conditions is limited. Rock breakouts may lead to blocking of the injection openings and thus to bedding deficiencies.
- Possible unbedded areas have to be additionally injected with mortar in order to allow for a stable load bearing structure.
- The amount of pea gravel needed for the backfilling process is high. The use of an artificial product is not economic. Hence, a natural deposit should be in close vicinity of the site, which is not always the case.

In order to achieve the bedding of the segmental lining at TBM driven tunnels in hard rock, the following procedure is usually adopted:

1. Injection of pea gravel in the invert if possible. Due to the limited distribution of a solid grain structure, only a small area of the segments is covered.
2. Grouting of the invert up to 30° to 60° to each side in order to guarantee a full contact between lining and rock mass.
3. Stepwise backfilling of the sidewalls as soon as possible up to the crown.
4. Checking of the backfilling results by opening the injection openings.
5. Additional injection of mortar if needed.

2.1.2.3 Additional grouting of the annular gap (optional)

Depending on the geological and project specific boundary conditions, additional grout may be added to the pea gravel at a later time. Thus, the annular gap is grouted at a certain distance to the TBM Shield tail or after completion of the tunnel drive. This procedure provides the following advantages:

- Drainage of formation water and relief of pressure on the lining prior to the grouting.
- Production of a complete and uniform bedding.
- Prevent pea gravel from relocating when single segments are removed (i.e. opening of a cross passage).
- Sealing of open joints within the lining to prevent water ingress into the tunnel.

The necessity of an additional grouting depends on the boundary conditions and requirements of the individual project. Especially when it comes to headrace tunnels in hydropower projects, the subsequent grouting of the annular gap as well as the surrounding rock mass is necessary (Seeber, 1999).

2.1.3 Unfavourable bedding condition behind the shield tail

Due to the operational procedure at the working area of a TBM, a fully backfilled annular gap might not be established after every ring installation. This leads to an unfavourable distribution of the pea gravel, leaving the segmental lining partially without bedding.

The rapid advance of the shield tail of a Double Shield TBM after a boring stroke has been completed, increases the unbedded area by removing the abutment of the backfilled material in the annular gap. This leads to a shear failure of the pea gravel and to its relocation within the annular gap. Therefore, the position of the backfill within the annular gap is unknown and can be estimated only. The shape of the relocation wedge is approximated by the angle of repose of pea gravel.

Bedding deficiencies within the annular gap primarily occur during the primary backfilling process behind the shield tail. Hence, the rings immediately after leaving the shield tail are mostly affected. If not bedded properly, an unfavourable load transfer within the segmental lining and possible tensile cracks due to bending can be the result (Grübl, 1998). To guarantee the serviceability of the support a relatively high reinforcement ratio is necessary. Therefore, from a static point of view the applied reinforcement within the lining segments is solely necessary for the first rings behind the shield tail up to a fully bedded support.

Segmental linings can develop sufficient resistance only when properly bedded. Therefore it is necessary to obtain the bedding of a full lining ring as soon as possible to avoid unfavourable stress distributions.

With increasing tunnel diameters the bedding with pea gravel becomes more difficult. Weber (2003) mentioned serious displacements in the lining due to backfilling with pea gravel amongst other influences with Double Shield TBMs with a diameter of 10 m.

At the Wienerwald tunnel (Single Shield hard rock TBM, $\varnothing = 10.68$ m) cracks appeared in the crown segments due to an insufficient bedding at the side walls behind the shield tail (Zwittnig et al., 2008; Daller et al., 2016). Investigations have shown, that the load bearing capacity of lining segments is mainly influenced by the quality of the bedding at the sidewall segments. Additional loads acting on the crown segments can lead to a failure of the support. Limits for displacement measurements have to be reconsidered since they are reached at a low distance behind the shield tail. Hence, chord length measurements using theodolites have been used in order to asses the deformational behaviour of the lining.

During the Single Shield hard rock TBM advance at the Tunnelkette Perschling ($\varnothing = 13.03$ m) an extension of the crown segment chord length was monitored (Bach et al., 2008; Benedikt et al., 2016). Investigations have shown, that a distinct relocation process of pea gravel during the stroke leads to an unfavourable bedding distribution. Hence, the stability of the segmental lining right behind the shield tail is solely maintained by the thrust forces. In order to avoid further deformations and to guarantee an early bedding of the side wall segments a mortar – pea gravel mixture had to be injected.

2.2 Overview of support systems for bedding improvements

A yielding support system, as is common with sequentially excavated tunnels, with TBM driven tunnels is difficult to realize. Several concepts have been proposed, trying to cope with faulted ground conditions. In order to be able to overcome the temporary state of an unfavourable bedding condition, the support also has to guarantee a force fitting contact between the lining and the rock mass. Hence, existing design concepts have to be evaluated due to their applicability for an unfavourable bedding situation.

In general, lining systems dealing with highly deformable ground conditions can be separated depending on the application of the resistance and the yielding principle Kovári (1998). The resistance principle demands an increase of the lining capacity. The focus of the yielding principle is to create a deformable system and to develop the necessary bearing capacity while the rock mass and the support

deforms towards equilibrium (Schubert, 1996).

The resistance principle is based on increasing the bearing resistance of the segmental lining. This can be obtained by either, increasing the thickness of the segments, replacing normal strength concrete with (U)HPC (high/ultra high performance concrete), adding a second segmental ring or placing an inner lining after the excavation is completed (Mezger et al., 2017). The prefabrication of (U)HPC lining segments involves higher requirements and needs to the manufacturing process than the use of concrete of normal strength (Dehn, 2003). The high brittleness bears potential for spalling due to deformations at joints (Maidl et al., 2013). The issue of an asymmetric loading of the segmental lining due to block break outs or an irregular bedding condition increases the required bearing capacity (Radončić, 2011). Hence, the use of the resistance principle is not applicable for incompletely bedded segmental linings.

Support systems based on the yielding principle can be subdivided into radially and tangentially deformable systems (Figure 5) (Cantieni & Anagnostou, 2009). With tangentially deformable systems yielding elements are placed in the longitudinal joints between the segments. While the rock mass is deforming radially, the circumferential length of the segmental lining. Radially deformable lining systems develop resistance with the ongoing closure of the annular gap. Hence, the circumferential length of the lining is not altered during this process.

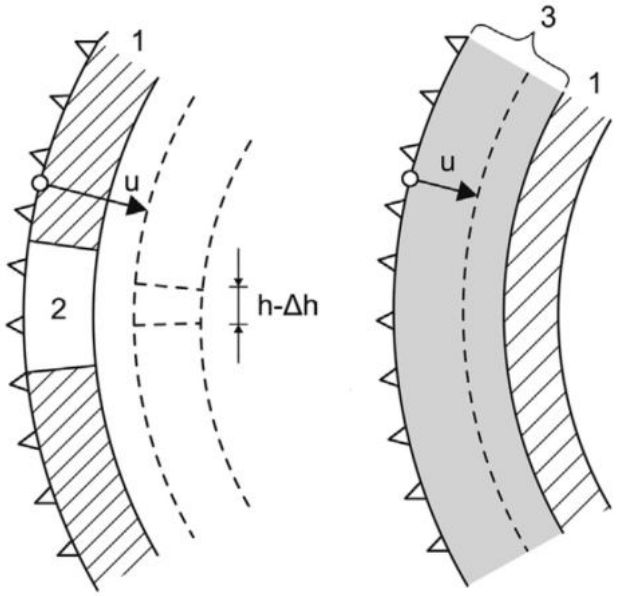

(a) Tangential deformable lining. (b) Radial deformable backfill material.

Figure 5: Types of deformable support systems (1 – lining, 2 – compressible element, 3 – compressible layer; taken from Mezger et al., 2018).

2.2.1 Tangential Systems

The basic principle of tangentially deformable systems derives from applications in conventional tunnelling, where they are already state of the art. Lenk (1931) proposed the use of timber layers between single rigid support elements.

Brunar & Powondra (1985) presented the first concept for a ductile segmental lining support systems using yielding elements which has been applied at the Ibbenbüren coalmine. The yielding principle is characterised by a ductile steel inner cylinder, an outer steel ring and ball bearings (see Figure 6). Under axial load, the ball bearings cause longitudinal grooves along the inner steel cylinder. Despite the successful implementation, the system was not applied again in following projects due to the high production costs and the fact that it was technically not possible at that time to install yielding elements behind the shield tail (Baumann & Zischninsky, 1994).

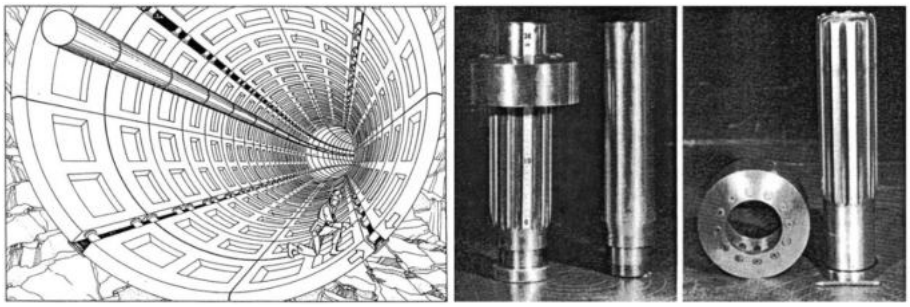

Figure 6: Meypo yielding elements (taken from Brunar & Powondra, 1985).

Strohäusl (1996) proposed placing deformable plastic elements along the longitudinal joints. This element consists of chambers which can be filled with compressible concrete and thus allows yielding in circumferential direction. Additionally the annular gap would be backfilled with a deformable grouting.

The applicability of Lining Stress Controllers for lining segments has been mentioned by Moritz (1999) (see Figure 7). Further investigations, based on numerical simulations (Moritz, 2011a) state that the solution yields promising results for tunnels with large deformations. Due to the fact that the segmental lining is installed in its fully hardened condition, the initial stiffness of yielding elements is insignificant. Hence, a simplified and cheaper version of the LSC elements is possible than for a shotcrete lined tunnel.

The yieldable “WABE” system has been proposed by the “Bochumer Eisenhütte” (Podjadtke & Weidig, 2010) with elements along the longitudinal joints (see Figure 8). Like the LSC elements those have been introduced to conventional tunnelling but never been tested at lining segments yet.

Tangential yieldable systems provide a wide range of applicability for ground conditions with large deformations. Due to the reduced stiffness and overall stability

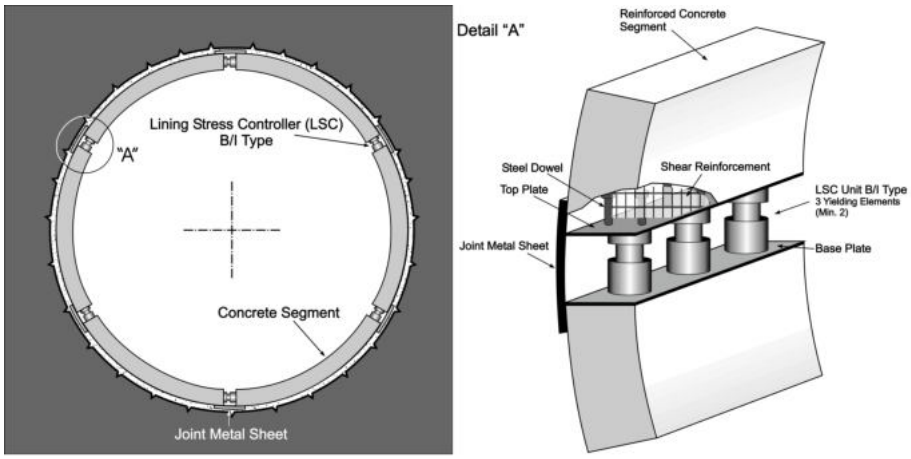

Figure 7: Longitudinal joints with LSC elements (taken from Moritz, 1999).

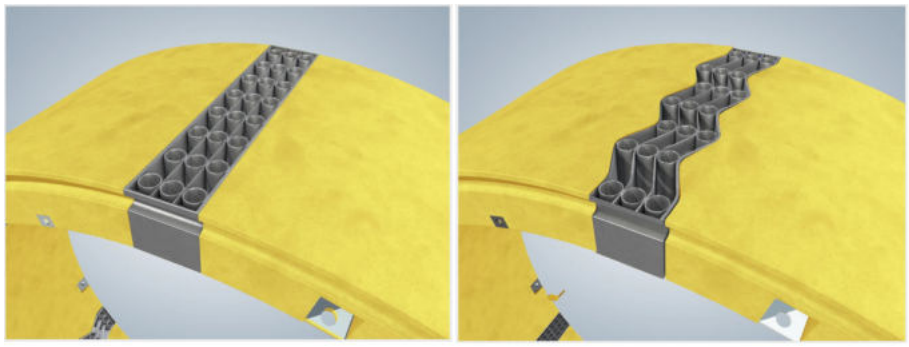

Figure 8: Longitudinal joints with WABE elements (taken from Podjadtke & Weidig, 2010).

the use for unfavourable bedding situations has to be evaluated carefully.

2.2.2 Radial Systems

Radially deformable systems can be placed within the annular gap after full ring closure is established. Hence, for the manipulation of lining segments no additional requirements arise. Haws & Mackenzie (1979) first patented the idea of a radial yieldable annular gap filling.

The first solution has been introduced by Vigl (2003) where a so called "convergence-compatible (CO-CO)" segmental lining is installed (see Figure 9). The concept features ribs on the outward facing surface of the lining elements. The idea originates from the approach proposed by Rabcewicz (1944) when tunnel linings in conventional tunnels used to be rigid. The system allows highly deformable rock masses to deform into the space between the ribs. During further research (Vigl et al., 2007) the approach was tested with respect to segment material technology, load deformation behaviour as well as geometrical boundary conditions. The research has shown promising results concerning the capability of dealing with highly deformable rock masses, however, the system has not been tested on site

yet. The issue of the initial bedding situation has not been resolved with this approach Schneider & Spiegl (2010).

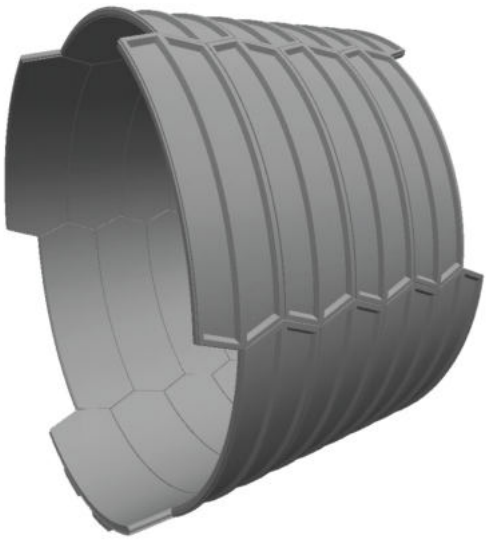

Figure 9: “Convergence-Compatible Segmental Lining System” (taken from Vigl, 2003).

Compressive mortar replacing pea gravel within the annular gap, has been presented by Schneider et al. (2005) with the brand name “COMPEX” and Billig et al. (2007) with the name “DeCo-Grout” in independent research projects. The systems replace the pea gravel by a compressible mortar – polystyrene mixture (see Figure 10). Both systems have been tested at the Jenbach tunnel with low overburden. With regard to logistical aspects, the system was reported to be successfully applicable (Gamper et al., 2009). No further evaluation of the overall deformational behaviour of the segmental lining has been provided within this report.

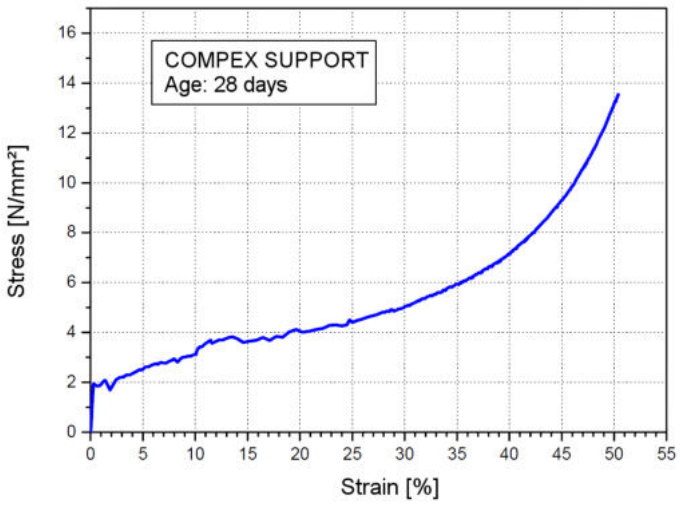

Figure 10: Load deformation curve for old COMPEX mortar (age 28 days, restricted lateral expansion) (taken from Schneider et al., 2005).

The radial yielding principle seems to provide a sufficient support for the first rings

behind the shield tail. According to Schneider & Spiegl (2010) pea gravel has to be replaced with mortar when encountering poor rock mass conditions in order to overcome the insufficient bedded state behind the shield tail. The issue of mortar bypassing the steering gap towards the cutterhead or rock joints has not been treated in a satisfactory manner.

2.3 Prediction of system behaviour in hard rock conditions

Compared to structures like bridges, buildings or construction pits the assessment of the system behaviour in tunnelling is far more difficult. The main influencing parameters are the geometrical and the mechanical properties of the support. Besides that, the excavation method, the excavation sequence and the generally inhomogeneous nature of the rock mass, as well as ground water, stress condition, play an important role. Applying the observational method in tunnelling offers a successful approach in order to overcome uncertainties during the design phase by monitoring the system behaviour and adapting the support as needed (Peck, 1969; Austrian Society for Geomechanics, 2010). When tunnelling with shield TBMs, the adaptability on site is more difficult. The design of the segmental lining is subject to the designer and cannot be adapted after production. Hence, different types of segments have to be provided in advance. These usually differ in the amount of reinforcement and concrete type, hardly in their geometry. The application of different segment types requires an early identification of ground types with different requirements regarding the support, since several rings have to be on the TBM in order to maintain a continuous advance. Additionally to changing the lining type, grout can be injected into the annular gap (when pea gravel is otherwise used) at a certain distance behind the cutterhead or an optional inner shell for single shell constructions can be installed. Both approaches do not increase the immediate support resistance.

At present, various approaches for the support design exist. By evaluating the forces acting on the lining, the design almost solely affects the segmental lining. The backfill layer is usually considered as an integral part of the surrounding ground mass. To date, issues connected to the backfill in the annular gap for hard rock conditions are not satisfactorily addressed.

2.3.1 Empirical methods

The use of empirical models due to their simple applicability is still very common. Empirical models in hard rock tunnelling are represented by rock mass classification systems generally known as Q, RMR and GSI system. The required rock support is derived from single indices. The so called Q_{TBM} value (Barton, 1999) was adapted from the original Q rating system (Barton et al., 1974) and serves

as a basis for the lining design, the penetration as well as the advance rate, neglecting the cutting process, unforeseen standstills, logistic difficulties and support working steps. Hence, the Q_{TBM} system not only inherits the shortcomings of its predecessor like the SRF-value but might even make it difficult to use the engineering judgement further by adding more indices to the rock mass and the operational procedure (Palmstrom & Broch, 2006; Anagnostou & Pimentel, 2012).

2.3.2 Analytical methods

One of the first approaches to calculate the section forces within linings was presented by Hewett & Johannesson (1922) using a continuum ring with horizontal deformability and applying the vertical (soil) reactions. Thrust force, shear force and bending moment were analytically computed for a given cross section at any given point in the lining. At this early stage of development, the deflection of the lining was disregarded. Hence, the approach leads to an uneconomical design (Bull, 1946).

Bull (1946) extended this approach (Hewett & Johannesson, 1922) by introducing a partially elastic bedded circular ring using single discrete fields. Vertical deflections at the crown caused by the ground load on the tunnel structure were implemented. Forces acting on the structure were separated into active and passive parts. The passive forces were determined by the ground and structure elasticity. Since the loads are only applied at the upper part of the tunnel structure, vertical equilibrium is solely reached by the invert bedding reaction. Therefore, the calculation method overestimates the bending moments (Schulze & Duddeck, 1964b; Meldner, 1975).

Schulze & Duddeck (1964a) introduced a continuous and completely bedded model approach. The assumed earth pressure loads were updated and additional assumptions were introduced. Loads in the crown and invert exceeding the loads in the side walls at the initial stage lead to high bending moments. Therefore, Windels (1966) later updated the analytical approach with the theory of second order to provide more accurate results.

Due to the decisive influence of longitudinal joints on the overall deformation pattern, Hain & Falter (1975) introduced bending moment coupling springs between adjacent beam elements. The approach used the earlier derived differential equations for buckling (Hain, 1968).

The developed analytical approaches were very time consuming due to the high number of unknowns. Hence, the static system were kept as simple as possible. At this stage, the development of computer based calculations helped to overcome this dilemma. Wissmann (1968) successfully introduced a computer based 2D framework program for arbitrarily formed tunnel shells. On this basis Meldner (1975) investigated the deformation behaviour of segmental linings on the basis of

the Schulze & Duddeck (1964a) calculation scheme. He also implemented longitudinal joints (Hain & Falter, 1975) and was the first to couple several rings by connecting radial joints using spring elements.

At the same time Muir Wood (1975) introduced a method to account for the longitudinal joints by reducing the flexural rigidity of a tunnel shell. The method can be considered for approximations avoiding the implementation of longitudinal joints. At present, the formulation due to its easy applicability represents a wide spread method for the pre dimensioning of tunnel shells:

$$I_e = I_j + I \cdot \left(\frac{4}{m}\right)^2 \tag{1}$$

where:
- I_e ..... effective second moment of inertia [m^4]
- I_j ..... second moment of inertia at the joint [m^4]
- I ..... second moment of inertia of the unjointed ring [m^4]
- m ..... number of segments ($m > 4$; keystone is only accounted if longer than 20% of normal segment in circumferential length)

The equation can be considered for a simple pre-design when using numerical simulations.

The German EBT recommendations (Deutsche Gesellschaft für Erd- und Grundbau, 1980) represents the first document which generally recommends the bedded beam model method as standardised procedure for the design of the segmental lining in soil. The importance of the radial bedding is highlighted and simplified equivalent bedding moduli for the subgrade reaction are given. Ahrens et al. (1982) provide a detailed investigation of the lining using numerical simulations. Stresses within the shell of different continuum approaches mentioned above and the bedded beam model method are compared.

The ITA Guidelines for the Design of Tunnels (1988) discuss the application boundaries between numerical methods and the bedded beam model. In order to provide a distinct boundary between the two methods, the stiffness ratio β has been introduced. The stiffness ratio represents the ratio between the ground stiffness and the flexural rigidity of the lining which is defined as follows:

$$\beta = \frac{E_s \cdot R^3}{E_c \cdot I_c} \tag{2}$$

where:
- E_s ..... deformation stiffness modulus of the ground [MPa]
- R ..... radius of lining [m]
- $E_c \cdot I_c$ ..... bending stiffness of the lining [MPa $\cdot$ m^4/m]

A low value for β relates to a rigid lining and/or weak ground. In return a high value represents a very deformable lining and/or a very stiff ground. For values above 120 MPa, a considerable load redistribution between lining and ground mass occurs (Guidelines for the Design of Tunnels, 1988). For a given concrete stiffness of $E_c = 30$ GPa and a lining thickness to radius ratio of ($d/R = 0.1$) the stiffness ratio β can be calculated to $\beta = 0.4 \cdot E_s$ [MPa] (Behnen et al., 2015). Hence, depending on the ground properties the stiffness modulus may reach 1000 MPa or higher. For the application of the bedded beam model method the values for β shall be smaller than 200 (ITA working group on general approaches to the design of tunnels, 1988).

The ITA Guidelines for the Design of Shield Tunnel Lining (2000) present an overview of several applicable methods for the design of segmental tunnel linings without any preference. These contain multiple analytical solutions, the bedded beam model, as well as numerical methods. Empirical approaches have been neglected. The Guideline provides detailed information on the boundary conditions of the individual methods without recommending any specific method.

2.3.3 Analytical methods - Bedded beam model method

The bedded beam model method replaces the statical system of the segmental lining with rigid beam elements. The interaction between adjacent segments is taken into account with single spring elements with the corresponding spring stiffness for translation and rotation. The ground – lining interaction is represented with radial and tangential springs. A given load case, defined on the basis of the in-situ state of stress or by considering a load case(e.g. block load) is applied on the nodal points of the statical system. With computational routines equilibrium is reached and the section forces calculated. With the section forces the design of the segmental lining can be evaluated using a basic 2D statical system.

Within this representation the radial springs play a crucial role for the determination of the section forces. These incorporate the response of the surrounding ground as well as the backfill layer for any given load case. Usually a linear coefficient of the subsoil reaction or "bedding modulus – k_r" for all stress magnitudes is provided. With increasing radial deformation the radial stress can be expressed as:

$$\sigma_r = k_r \cdot u_r \tag{3}$$

where:
- σ_r ..... radial stress acting on the lining [MPa]
- k_r ..... bedding modulus [MPa/m]
- u_r ..... radial deformation of the spring element [m]

With the closed-form solution for the elastic plate with a circular hole presented by Lamé (1852) the simplified radial deformation in relation to the internal pressure

p_i is given by:

$$u_r = \frac{p_i \cdot r_0}{E} \cdot (1 + \nu) \tag{4}$$

where:
- u_r ..... radial deformation displacement of the spring element [m]
- p_i ..... internal radial pressure [MPa]
- E ..... Young's modulus [MPa]
- ν ..... Poisson's ratio [-]

By replacing σ_r with the internal pressure p_i in equation 3 and substituting u_r in Equation 4 k_r can be calculated with the following equation:

$$k_r = f \cdot \frac{E_s}{r} \qquad \text{for } f = \frac{1 - 2 \cdot \nu}{1 - \nu} \tag{5}$$

where:
- k_r ..... bedding modulus [MPa/m]
- E_s ..... constrained modulus [MPa]
- r ..... tunnel radius [m]k_r
- f ..... correction factor [-]
- ν ..... Poisson's ratio [-]

It can be seen that the correction factor f is solely influenced by the Poisson's ratio. Nevertheless, in practical applications generalized values between 0.5 and 1 are used.

Equation 6 is widely adopted in soil applications. When using mortar as backfill material it is also applied under hard rock conditions. Since it is derived from the basic formulation by Lamé (1852) it solely applies for a continuous, homogeneous, isotropic and linearly elastic medium and primary stress free conditions.

When pea gravel as backfilling material is applied, an extended approach is used based on a layered ground model. With this approach the annular gap and the surrounding ground are treated as individual layers, using the half space theory (see Figure 11) as follows:

$$k_r = \frac{1}{\frac{d_{ag}}{E_{s,ag}} + \frac{d_rm}{E_{s,rm}}} \tag{6}$$

where:
- k_r ..... bedding modulus [MPa/m]
- d_{ag} ..... width of the annular gap [m]
- d_{rm} ..... influence depth of the rock mass [m]
- $E_{s,ag}$ ..... constrained modulus of backfilled material [MPa]
- $E_{s,rm}$ ..... constrained modulus of the rock mass [MPa]

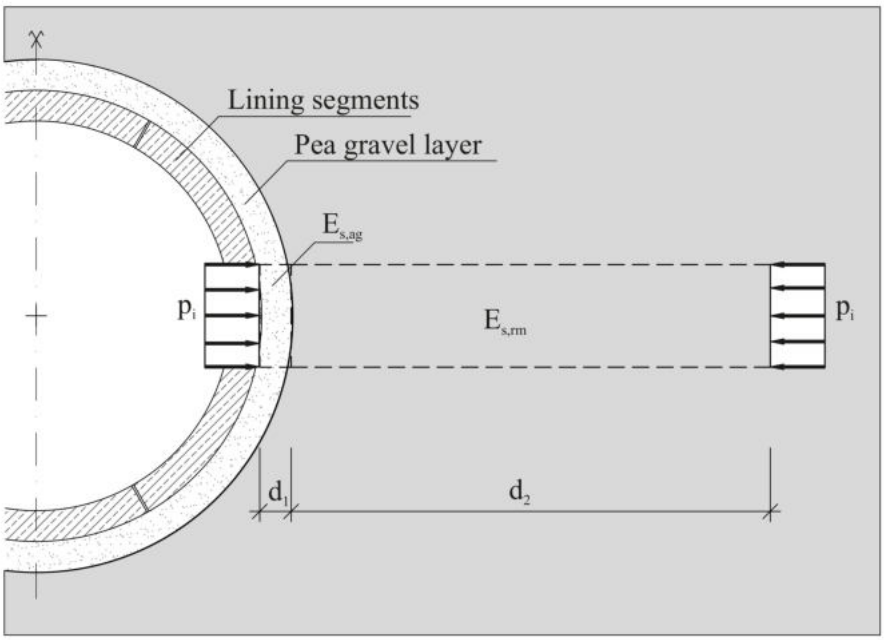

Figure 11: Approach for the determination of the bedding modulus including pea gravel (taken from Preschan, 2018).

Within this approach the influence depth d_{rm} has to be estimated. Thienert & Pulsfort (2011) and Behnen et al. (2013) suggest values between one and two times the tunnel radius.

The formulation for the calculation of the bedding modulus including the annular gap backfill is subject to fundamental misunderstandings. It neglects the decrease of radial stresses with increasing distance to the excavation boundary. Hence, the subsoil reaction coefficient is underestimated. In addition, disregarding the shear stresses between the backfill and the rock mass due to different Poisson's ratios and the assumption of an elastic ground behaviour further decreases the accuracy of the results.

The bedded beam model method is a practical tool for the design of lining segments. Considering the bedding properties further investigations regarding the analytical approach are necessary.

2.3.4 Numerical analysis

At present, different design methods are applied in different countries. While numerical methods have replaced analytical and empirical approaches especially in anglophone countries, the bedded beam model method is still widely applied in German speaking parts of Europe. Nevertheless, numerical approaches are used for the solution of complex engineering problems. Due to the simple structure, the bedded beam model is still used for validation/verification purpose (The British Tunnelling Society, 2004).

In contrast to the simulation of conventionally driven tunnels the modelling of a TBM driven excavation is much more complex. Depending on the specific task of the performed simulations, the model usually undergoes significant simplifications. Nevertheless, only in rare cases mechanized driven tunnels may be simulated using 2D models. At present, the available numerical methods can be used effectively for the simulation of many different aspects of TBM driven tunnel. Difficulties arise from complex interactions between TBM, support and rock mass.

Using numerical methods in hard rock TBM tunnelling, aspects like penetration performance, thrust force, possible shield jamming, rock mass deformation, different linings, etc. or the back calculation of failure modes amongst others can be assessed. Hence, depending on the aim of the investigation only the region of interest is modelled with the necessary influences. Numerical models in TBM tunnelling are prone to a relatively high level of detail. In addition, the identification of important, specific aspects is difficult and subject to further investigation.

The advantage of three dimensional modelling is the possible simulation of a wide variety of implementable mechanisms. The disadvantage is given by the long calculation time and the high amount of required storage and computational power. The complexity of the problem, uncertainties regarding the ground properties and interaction parameters of the TBM, the support and the rock mass limit the applicability of numerical simulations.

2.4 Determination of the bedding properties

The bedding properties are mainly influenced by the deformational properties of pea gravel. The deformational properties can be subdivided into two categories: the elastic properties which describe the stress-strain behaviour and the relocation response within the annular gap.

2.4.1 Elastic properties

The elastic properties expressed by the Young's modulus and the Poisson's ratio of pea gravel are the decisive input parameters for the bedding modulus. Hence, a sound knowledge of the expected range is necessary for lining design. At present, tunnelling guidelines do not define a testing procedure to determine the elastic properties of pea gravel. The determination of the load deformation behaviour is solely carried out by means of laboratory tests. The most suitable and normatively regulated one dimensional compression test (oedometer test) cannot be used due to the small specimen dimensions. Hence, non standardized tests are used in practice in order to determine the elastic properties.

Vigl (2000) has investigated the elastic behaviour of pea gravel using non standardized constrained compression tests with a grain diameter range between 8 and

12 mm. Within this study the influence of the grain shape (rounded/broken) and compaction was investigated. The deformation modulus ranged between 30 MPa for broken and not compacted gravel to 130 MPa for a rounded and compacted gravel.

A model test setup (Figure 12) was developed by Bilfinger Berger SE. The device was designed to test the deformational response of a two layer system, consisting of backfill and soil with a model scale of 1:1. This method results in lower stiffness moduli than are obtained with oedometer tests due to the lower confinement (Behnen et al., 2013).

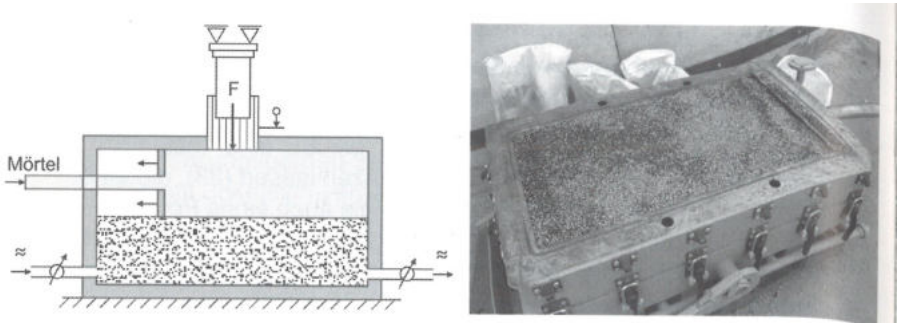

Figure 12: Model test setup for on site bedding evaluation (taken from Behnen et al., 2013).

For the CLEM7 project in Brisbane, Australia, Behnen et al. (2010) investigated the deformational response of pea gravel using oedometer tests and the test apparatus shown in Figure 12. Within this study rounded as well as broken gravel with varying sizes of fine grains were used. The results scatter in a wide range of values (see Figure 13). No further results with the presented apparatus have been published yet.

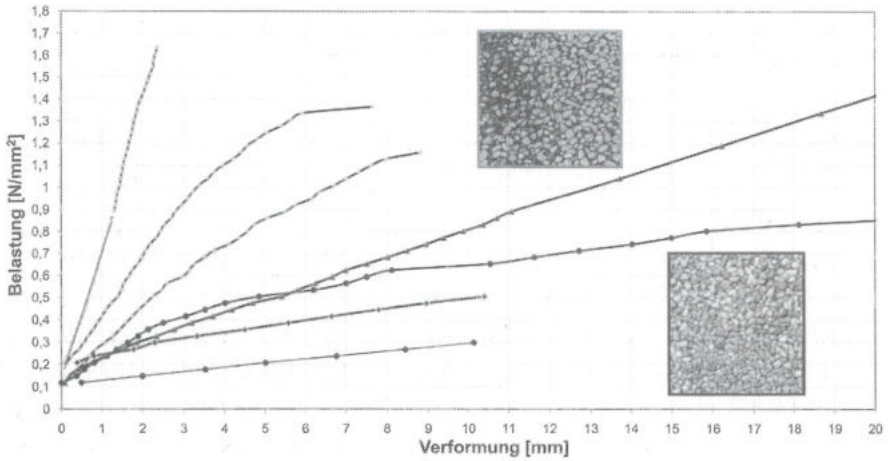

Figure 13: Load–deformation relationship for different pea gravel compositions (taken from Behnen et al., 2010).

Since neither a single test procedure, nor uniform test specimen dimensions are defined, the results of the different tests are difficult to compare. Therefore, the use

of certain parameters in the design phase must be reviewed critically. Hardly any in-situ verication of the used parameters occurs during the design or throughout the construction phase. The application of characteristic values for gravel from a variety of sources with the associated strong variations also provides no reliable parameters. In general, the associated reference pressures are not specified and the test method is not explicitly stated.

2.4.2 Bedding distribution

At present, the backfilling success of the annular gap is evaluated either by comparing the amount of backfilled material with the available annular gap volume or by monitoring methods. For the latter, methods such as hand lasers, theodolites or scans by means of chord measurements at the side wall and crown segments, as well as the observation of cracks and deformation are applied Guideline Concrete Segmental Lining System (2011). Optical methods only offer indirect indications of the bedding condition of the support. Additional drill holes in order to confirm the backfill success are usually avoided. At present, no comprehensive methods have been tested which represent the state of the annular gap satisfactorily.

Geophysical measurement methods are preferred due to their non-destructive application and broad applicability in infrastructure projects. They are based on the measurement of electrical and mechanical properties of various media. Depending on the measuring principle, they can be separated into

- gravimetric
- seismic
- electric
- magnetic
- and electromagnetic

methods.

For the given task, these measurement methods are limited to seismic (impulse-echo) and electromagnetic. The thickness of the lining segments as well as the annular gap is generally known. Hence, by evaluating the respective physical properties of the involved components (e.g. reinforced concrete, grout, pea gravel, air, water) the response of the expected signal can be modelled and compared with on-site conditions.

2.4.2.1 Impulse-echo

The impulse-echo is an acoustic method, which measures wave reflections caused by a mechanical input of short duration. The acoustic waves are usually generated

with a small metal impactor (sphere) close to the accelerometer (see Figure 14). These waves propagate through the medium and are partially reflected at a boundary between two materials with different acoustic properties including voids. The sensor then measures the oscillation amplitudes and the frequency spectrum of the reflections. With a known acoustic velocity of the components and the obtained frequency the depth of the reflections can be obtained.

Figure 14: Illustration of the impact-echo method. Impactor (metal sphere) with a diameter of 25 mm close to sensor (taken from Aggelis et al., 2008).

The impulse-echo-method was applied at a telecommunication and sewage tunnel with a diameter of 5 m and a segmental lining thickness of 22.5 cm (Aggelis et al., 2008). The tunnel is situated in the central area of Japan with a bedrock consisting of mudstone. The backfill was performed using grout with bentonite and cement as solid constituents. The relevant acoustic material properties were derived from core samples and laboratory tests. Since a comparison of the volume of calculated and injected grout led to differences of 30 %, acoustic tests were performed to check the sufficient quantity of the backfill. Figure 15 shows the expected scenarios for the measurements.

Since the differences of the acoustic properties of grout and mudstone are much smaller than those of grout and air, the rock mass side boundary of a partially filled annular gap reflects a reliable signal. Aggelis et al. (2008) illustrated the results using wavelets by plotting the reflected energy of one measurement over the time domain (see Figure 16).

Due to the material dependent acoustic velocity, the time axis also accounts for the

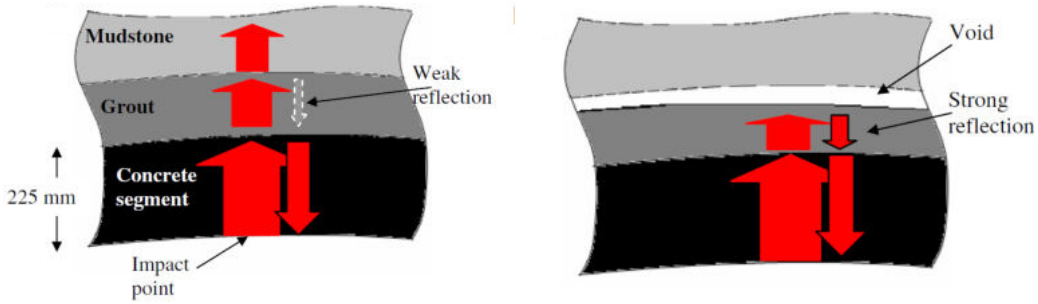

(a) Fully grouted annular gap.

(b) Partially grouted annular gap.

Figure 15: Scenarios for differently filled annular gaps indicating the intensity of the expected reflections due to differences of acoustic properties (taken from Aggelis et al., 2008).

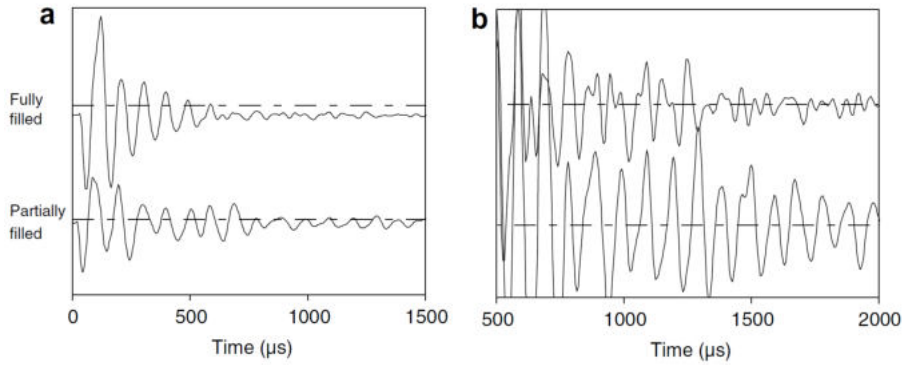

Figure 16: Frequency – time domain plot. Left: limit set to 10% of maximum energy threshold; Right: limit set to 0.1% of maximum energy threshold (taken from Aggelis et al., 2008).

penetration depth. It can be noticed that especially in the fully filled annular gap almost all energy is reflected prior to 500 μs. This represents the boundary of the segmental lining and the grout mixture. Since the grout – air interface at the partial filled case causes a strong reflection, the energy expands beyond 500 μs.

The disadvantage of this method lies in the application procedure of the sensors. Depending on the number of measurements the method is time-consuming. Furthermore, only boundaries which are completely interconnected can be detected (Karlovsek et al., 2012). Hence, when using pea gravel as backfilling material no reliable results can be expected.

2.4.2.2 Ground penetrating radar

Electromagnetic methods (ground penetrating radar) are characterized by the high measuring speed, the detectability of layer boundaries as well as of voids. The electromagnetic waves of the ground penetrating radar are emitted by an electric dipole antenna. The waves travel with a velocity mainly depending on the elec-

trical properties of the layer through the respective medium. At a boundary, part of the energy is reflected and consequently recorded by the receiving antenna. In this case, the recording device registers an amplitude and the corresponding two-way travel time (penetration time and reflection time) of each propagating wave (Knödel et al., 2005). In order to obtain a radargram of a subsoil profile, the transmitting-receiving antenna is moved along a profile line (see Figure 17).

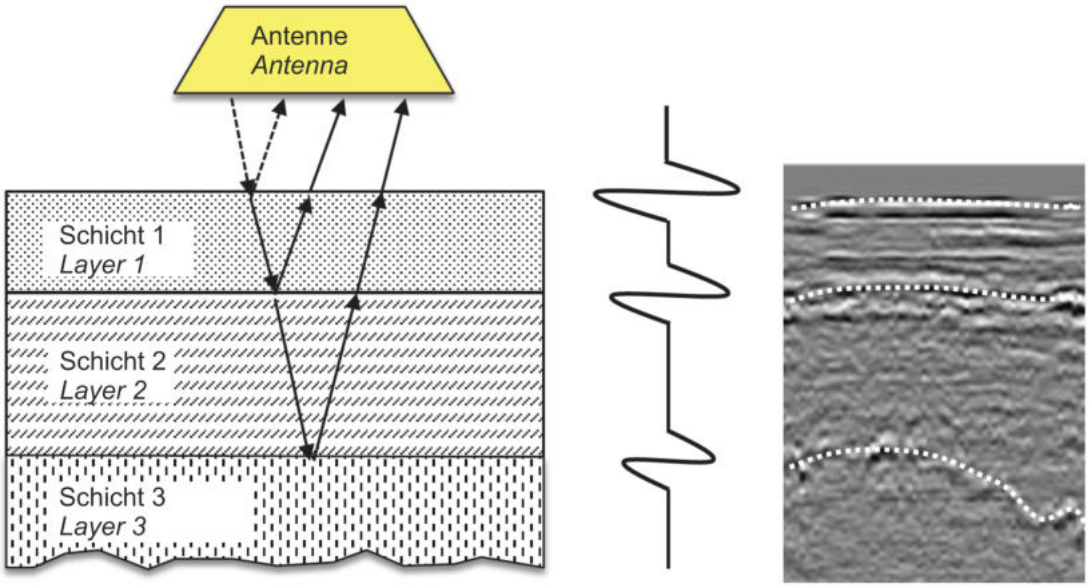

Figure 17: Determination of the ground profile using propagating electromagnetic waves. Left: Ground radar antenna with underground profile; Middle: single reflected wavelet; Right: Series of wavelets form a radargram (taken from Lalagüe, 2015).

The resolution of of the radargram increases with higher frequencies due to their shorter wave lengths. At the same time, the absorption and scattering of high frequencies causes a reduction of the investigation depth. Hence, it is necessary to carefully examine the most suitable frequency for the given situation in order to obtain a sufficient investigation depth and a sufficient resolution to detect the annular gap. Applicable antenna frequencies for detection of void range from 250 MHz up to 2.6 GHz.

When applying electromagnetic methods at segmental linings the most relevant issue is the noise caused by the installed reinforcement. Due to the high electric conductivity, the electromagnetic waves cause an electric field within the metallic rebars which creates a new magnetic field. Hence, several electromagnetic fields superimpose, decreasing the measurement resolution of deeper structures.

To verify the homogeneity of the grouted backfill Xie et al. (2007) tested the GPR method in the Shanghai Metro Line, China. The thickness of the segmental lining was 35 cm with an inner steel reinforcement spacing of 15 cm and an annular gap width of 20 cm. Measurments were carried out with a frequency of 200 MHz. Due

to the varying water content of the newly placed backfill grouting and the high influence of water regarding the electromagnetic properties, a so called Common-Mid-Point method was used. The investigation yielded promising results, as shown in Figure 18.

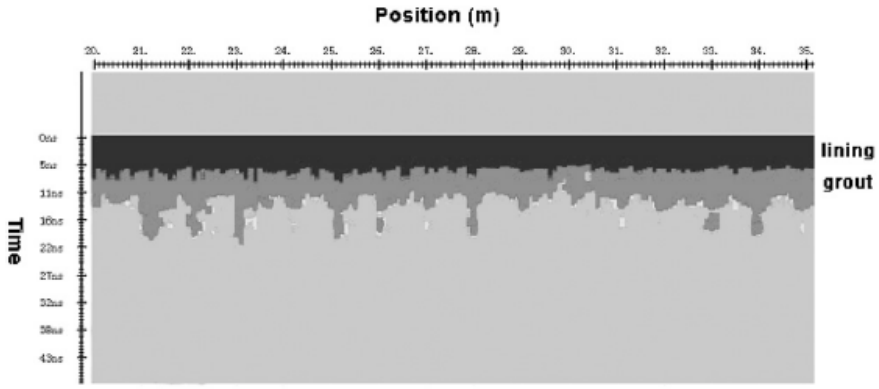

Figure 18: Radargram of a 200 MHz electromagnetic investigation of grout behind lining (taken from Xie et al., 2007).

In a further study, Zhang et al. (2010) increased the used frequencies up to 1 GHz. The experiments were carried out on single freestanding segments, as well as on installed rings with a transition from 20 days old mortar to air. Figure 19 shows measurements of zones with grouted and ungrouted annular gap. This research showed the frequency of 500 MHz to be the most suitable.

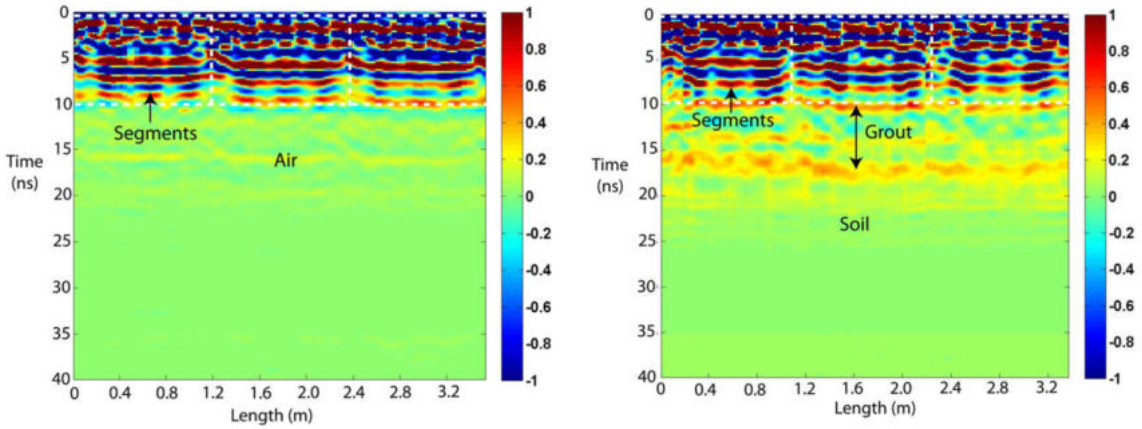

(a) Air filled annular gap.

(b) Grouted annular gap.

Figure 19: GPR field measurements of 35 cm reinforced lining segments (taken from Zhang et al., 2010).

Lalagüe et al. (2016) conducted a study dealing with the detection of rockfalls onto free standing inner linings in Norwegian tunnels. In good rock quality conditions in Norway, sometimes prefabricated inner linings are used, having basically no contact to the ground. Due to ageing processes of the surrounding rock mass, rock falls from the crown on the inner lining may lead to instability of the lining. Therefore, a destruction free solution to investigate loose rocks resting on the roof

support using GPR methods has been proposed.

In order to investigate the influence of the reinforcement and to demonstrate the measurability of different rock sizes behind the lining, three test setups have been created (Figure 20). Test setup 1 has two aligned layers of reinforcement with a lateral spacing of 14 cm. Test setup 2 consists of the same configuration but non aligned reinforcement layers. Test setup 3 does not contain any reinforcement except a simple rebar network due to statical reasons. All test setups have a thickness of 15 cm.

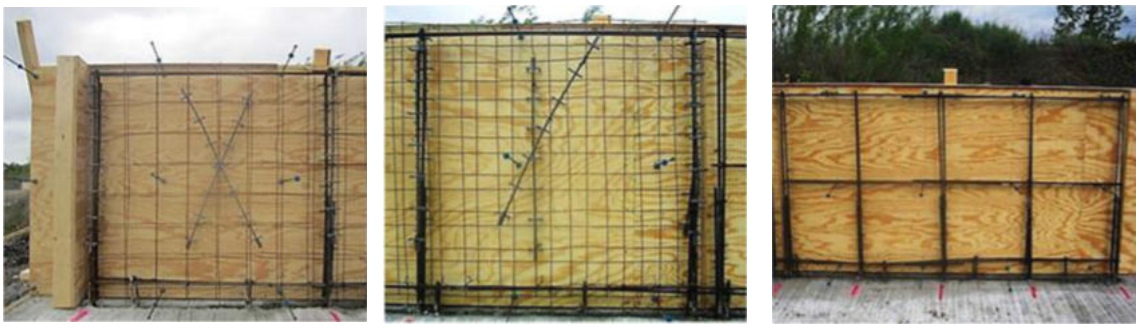

(a) Test setup 1. (b) Test setup 2. (c) Test setup 3.

Figure 20: Panels with different reinforcement configuration prior to the concreting (taken from Lalagüe et al., 2016).

Rocks with different sizes from 5 to 50 cm were placed on a board behind the Panels (see Figure 21) in order to simulate different rock falls. Ground coupled GPR measurements were carried out with 400 MHz, 1.5 GHz and 2.6 GHz. The antenna frequency of 1.5 GHz provided the best results, where smaller blocks could still be detected (see Figure 22). The 400 MHz measurement was considered as unsuccessful due to the attenuation of low frequencies by the reinforcement. The 2.6 GHz measurements lead to an insufficient penetration depth resulting in larger blocks being undetected.

The introduced research projects yield promising results with a comparable setup. Nevertheless GPR measurements for the detection of the pea gravel distribution behind a reinforced segmental lining have not been conducted yet. Due to the ability to detect boundaries which are not force fitted, the application of GPR methods appears to be the most promising for the given boundary conditions.

Figure 21: Test setup for the location of rocks behind reinforced concrete wall (taken from Lalagüe et al., 2016).

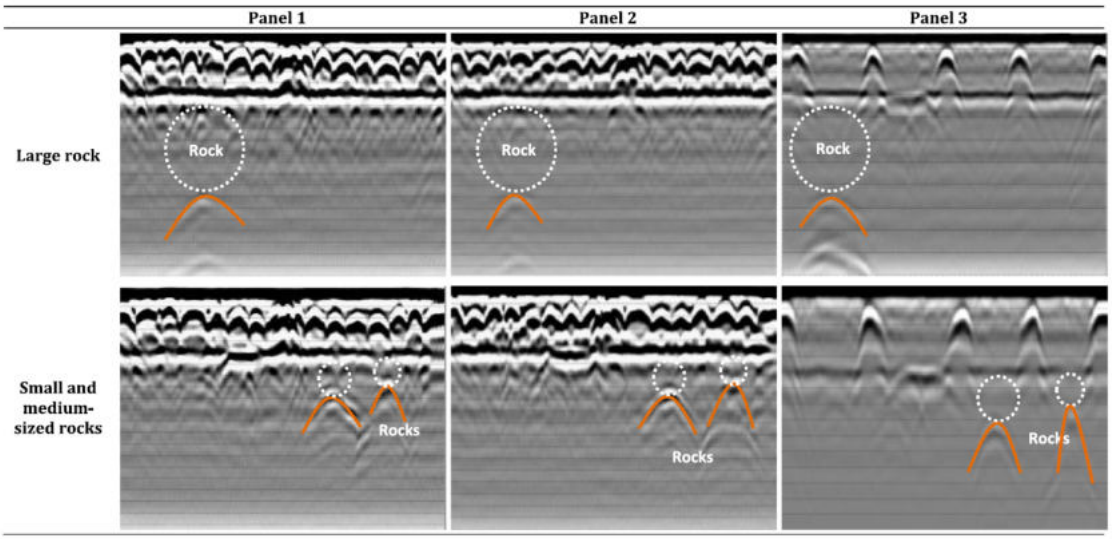

Figure 22: Radargrams for the same rock sizes tested on different test setups with a meauring frequency of 1.5 GHz (taken from Lalagüe et al., 2016).

2.5 Definition of objectives

After evaluating the state-of-the-art on the bedding of TBM driven tunnels and its influence on the support, the following issues demand further clarification:

1. **Geomechanical characterisation of pea gravel.**
   Considering the mechanical properties of pea gravel presently commonly used for the design of the segmental lining, following questions arise:

   a) What are the deformation properties of pea gravel and is it possible to represent the deformation behaviour of pea gravel using standardized testing methods?

   b) Is there a distinct stress and loading type dependency of the deformation properties?

   c) What are the deformation properties of pea gravel on site and are they influenced by the distinct relocation behaviour?

2. **Deformation behaviour of lining segments after leaving the shield tail.**
   Displacement measurements of lining segments are usually conducted on a regular basis. Measurement sections contain up to five monitoring points. Since the ring of segments experiences an immediate settlement after leaving the shield tail, rigid-body motion and ring deformations deviating from the original arrangement are measured at the same time.

3. **Design improvements to overcome the temporary partially bedded state.**
   With a distinct failure mechanism of pea gravel within the range of the first rings behind the shield an additional load case arises. A full segment ring, being not completely bedded, undergoes deformations, and thus may be damaged. Hence, either the design has to be modified to account for those conditions, or additional support should be implemented to improve the deformation and loading situation of the segment ring in areas of non complete bedding. Hence following points need clarification:

   a) On which design principle do improvements have to be based, and how can the resulting changes be integrated into the construction process?

   b) How can these improvements influence the overall stability of the support?

4. **Relocation behaviour of pea gravel.**
   The relocation behaviour of pea gravel at a shield TBM is a well known fact. The distribution and the extent of the bedding slope behind the shield tail is unknown. With a distinct failure mechanism of pea gravel within the range of the first rings behind the shield following questions arise:

   a) How does the failure mechanism of pea gravel occur and what is the distribution and extent within the annular gap behind the shield tail?

b) Can the distribution within the annular gap be depicted using nondestructive methods?

On the basis of these conclusions, following goals within this doctoral thesis can be defined:

1. Investigation of the geomechanical properties of pea gravel using standardized tests. The main goal is to obtain a better understanding of the behaviour of pea gravel which represents a crucial member of the lining – rock mass interaction. Hence, large oedometer tests (Wieser, 2011) and load plate tests shall be performed. The Young's modulus as a representative value for the deformation behaviour has to be reviewed differing between loading, unloading and reloading cycles. In addition, the influence of the stress level has to be outlined. For the sake of completeness and to gain a better understanding, the strength parameters shall be obtained as well.

2. Designing and conducting an in-situ test apparatus for the determination of the deformation behaviour of pea gravel within the annular gap and perform tests on site. The principle of the load plate test shall be adopted for the use on site without any need for electric or hydraulic supply. The test apparatus should allow a non-destructive procedure. The load application on pea gravel has to be done through an existing injection opening for the injection of the backfill. The in-situ testing device for the determination of the deformation behaviour of pea gravel shall be used to validate the laboratory results and to determine the in-situ parameters.

3. Provide knowledge on the relocation process and distribution of pea gravel within the annular gap behind the shield tail. A suitable model test should show the relocation behaviour of the bedding material during the forward movement of the shield tail. The model scale has to be chosen properly in order to reproduce the failure mechanism as realistically as possible. The failure mechanism as well as the slope angle within the annular gap have to be identified. A non-destructive investigation procedure using ground penetration radar technology shall demonstrate the detectability of pea gravel behind the lining. Limitations for this procedure shall be pointed out. Hence, the in-situ repose angle of pea gravel can be determined.

4. Design and implementation of a temporary bedding concept to overcome the temporary state of a partially bedded segmental lining. The system should establish an immediate contact between the lining and the surrounding rock mass. Due to different deformation behaviour of different rock masses, the system has to be adjustable in radial direction in order to manage different annular gap widths. Load concentrations on the segmental lining due to the newly developed design have to be avoided. The system shall be implemented into the existing construction processes at the TBM without major delays in the advance process.

5. Investigate the deformation behaviour of the segmental lining after leaving the shield tail. On the basis of existing displacement measurements the rigid-body motion shall be determined. The ongoing ovalization of the assembled ring of segments shall be described depending on the load redistribution between segmental lining and rock mass, rock mass deformations and observable rock failure mechanism. With this procedure the implemented bedding concept shall be evaluated and compared to similar cases.

6. Using 3D numerical methods, the influence of the design improvements for the given rock mass conditions shall be validated. A suitable model has to be created, incorporating all relevant parts of the TBM advance and the construction process. On this basis, the deformation behaviour of the segmental lining as well as the section forces will be evaluated and the advantages of the design improvements regarding the utilisation of the support pointed out.

3 Deformation behaviour of pea gravel

The deformation behaviour of pea gravel represents one of the most important influencing factors for the bedding quality of the segmental lining. It is of upmost importance to establish a homogeneous filled annular gap in order to keep the deflection forces within the lining as uniform as possible. Hence, the gravel needs to be closely graded in order to guarantee an evenly distributed medium with homogeneous degree of compaction and elastic behaviour. With the intent to investigate the deformation behaviour of pea gravel, the problem was subdivided into two major topics which were further analysed:

1. In order to obtain information on the stress-strain behaviour of pea gravel, a series of laboratory, on-site and in-situ tests were executed. These tests allow one to study the deformation response under different conditions. Hence, the expected range of the Young's modulus can be compared with the material parameters presently used which influence the design of the segmental lining.
2. To be able to consider the distribution of pea gravel within the annular gap, the relocation behaviour as well as the the distribution at rest has to be investigated. Hence, scaled planar and circular model tests simulating the annular gap with pea gravel were performed in order to obtain further insights on the rearrangement process. Moreover, a comprehensive test procedure using ground penetration radar technology was conducted in several steps to investigate the limiting factors, the material properties of the components, the measurability using an analogue model and finally the in-situ repose angle at rest of pea gravel.

3.1 Elastic properties

At present, the determination of the stress – strain behaviour of pea gravel is solely carried out by means of laboratory tests. The most suitable and normatively regulated one-dimensional compression test (oedometer test) cannot be used due to the small specimen dimensions. In practice, non-standardized tests (model tests (Behnen et al., 2012) and large-scale oedometer tests (Wieser, 2011)) have shown promising results for the determination of the stiffness or the bedding modulus.

Three different test procedures have been executed in order to obtain an overview of the load – deformation behaviour of pea gravel under different boundary conditions. With the large oedometer test and the load plate test, the influence of different confinement conditions have been evaluated and compared. In addition,

a newly developed in-situ load plate apparatus allowed tests of the load response of pea gravel within the annular gap.

3.1.1 Large oedometer tests

For the laboratory determination of the elastic properties the large oedometer apparatus developed by Wieser (2011) has been chosen. With an inner diameter of 300 mm and a possible sample height between 60 and 200 mm, the dimensions account for the grain to sample size ratio according to the standard Casagrande oedometer. Pilgerstorfer (2014) has performed an extensive testing program on artificial bimrock material confirming the applicability and reliabilty of the test apparatus.

3.1.1.1 Test preparation

Two pea gravel samples with different grain size ranges were used for the oedometer tests. Six tests with the diameter range of 8 to 11 mm and two with the range 4 to 8 mm were performed. In order to investigate a possible pre - compaction, an oscillating load was applied over a period of 15 minutes. The test series are shown in Table 1.

Table 1: Large Oedometer test series on pea gravel.

Series	Grain size distribution [mm]	Pre compaction [-]	Maximum load step [MPa]
1	8 – 11	No	1
2	4 – 8	No	1
3	8 – 11	Yes	1
4	4 – 8	Yes	1
5	8 – 11	No	20
6	8 – 11	No	20
7	8 – 11	No	20
8	8 – 11	No	20

In order to investigate the influence of grain disintegration, the pea gravel in series 5 to 8 was loaded up to a maximum stress level of 20 MPa. The remaining test series have been limited with 1 MPa in order to avoid grain disintegration.

Figure 23 shows the test sample of series 5 inside the oedometer ring prior and after the test procedure. In Figure 23b the grain disintegration after the final load step can be seen. At this point it is unknown at which load level the first cracks occurred.

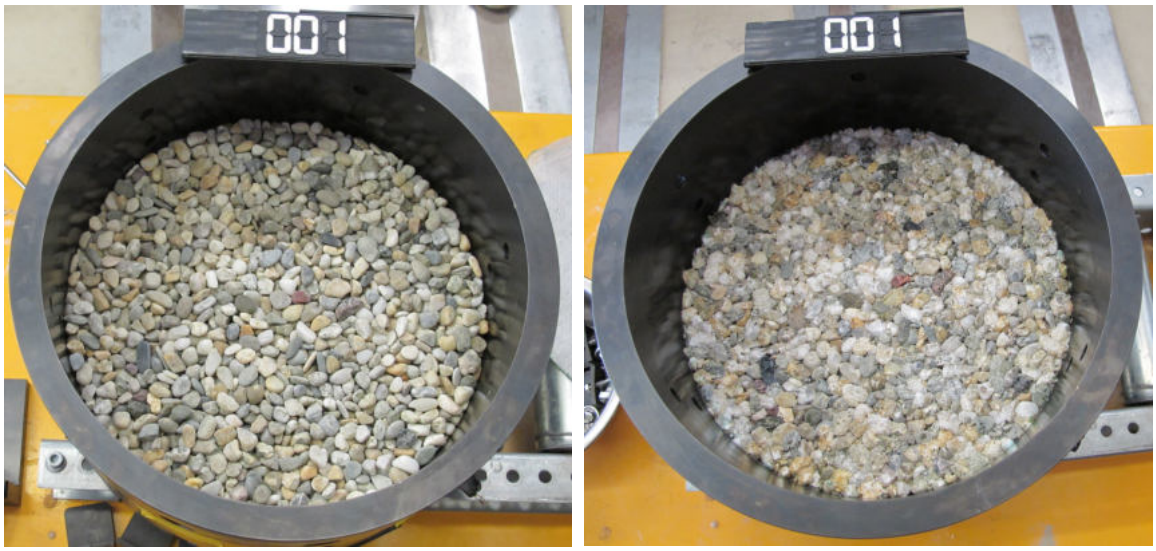

(a) 8 – 11 mm sample before test. (b) 8 – 11 mm sample after test.

Figure 23: Pea gravel sample before and after the oedometer test with load maximum of 20 MPa (Series 5).

The oedometer setup allows a subtraction of the frictional forces occurring between the circular steel ring and pea gravel. Hence, the load levels represent the effective stresses acting on the specimen. All load levels have been kept constant until the displacement rates reached almost zero. The test procedure has been executed according to ÖNORM EN ISO 17892-5 (2017).

3.1.1.2 Data evaluation

For the determination of the confined modulus E_s the strain and stress increment for each load cycle were identified and assigned to either first loading, unloading or reloading cycle. Assuming that the solid content of the specimen stays constant and lateral expansion is prevented, the following relationship for the determination of the confined modulus E_s can be used:

$$E_s = \frac{\Delta\sigma}{\Delta\varepsilon_a} \tag{7}$$

where:
E_s ..... constrained modulus [MPa]
$\Delta\sigma_a$ ..... stress increment [MPa]
$\Delta\varepsilon_a$ ..... axial strain increment [-]

In order to provide comparable results with other test routines, the Young's modulus was derived using following relationship:

$$E = E_s \cdot \frac{(1+\nu)\cdot(1-2\nu)}{1-\nu} \tag{8}$$

where: E ..... young's modulus [MPa]
E_s ..... constrained modulus [MPa]
ν ..... Poisson's ratio [-]

The Poisson's ratio for pea gravel ranges usually between 0.1 and 0.25. For the evaluation of the oedometer tests ν was set to 0.2.

3.1.1.3 Results

The stress – strain development associated to the individual maximum stress step of 1 MPa and 20 MPa is shown in Figure 24a and 24b, respectively. While the test series in Figure 24b illustrates a homogeneous development of the load response, the series in Figure 24a indicate deviating behaviour which is explained by the pre compaction condition. The compacted samples show slightly stiffer response during the first loading up to a normal stress level of 0.1 MPa. Beyond this level, a distinct decline in the first loading path is shown. The influence on the elastic response has to be investigated by plotting the Young's moduli in relation to the normal stress level.

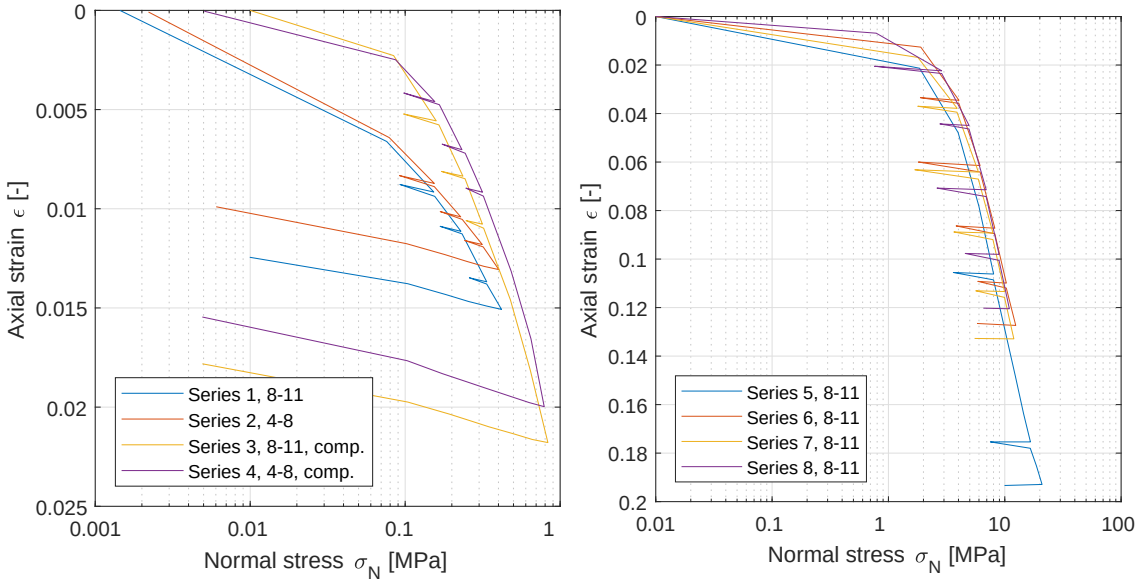

(a) Series 1 - 4.

(b) Series 5 - 8.

Figure 24: Stress – strain development of the oedometer tests (comp. – pea gravel was preloaded).

Figures 25 and 26 provide a graphical evaluation of the development of the Young's moduli over the applied normal stress according to Section 3.1.1.2. The markers indicate the secant modulus between two adjacent loadsteps and is therefore plotted at the intermediate stress level.

The results of the first loading moduli for all oedometer tests are presented in Figure 25. Different markers indicate the different maximum load levels. A steady increase of the Young's modulus up to 135 MPa at a stress level of 0.95 MPa is

recorded. Subsequently there is a decrease in the Young's modulus up to a normal stress of approximately 6 MPa. This might be due to the fact that the strength of the individual grains is exceeded. After a stable grain skeleton of broken and intact grains is established, a further increase in the Young's modulus from a normal stress of 8 MPa can be observed. The inspection of the test samples with a maximum normal stress level of 20 MPa showed a pronounced grain fragmentation.

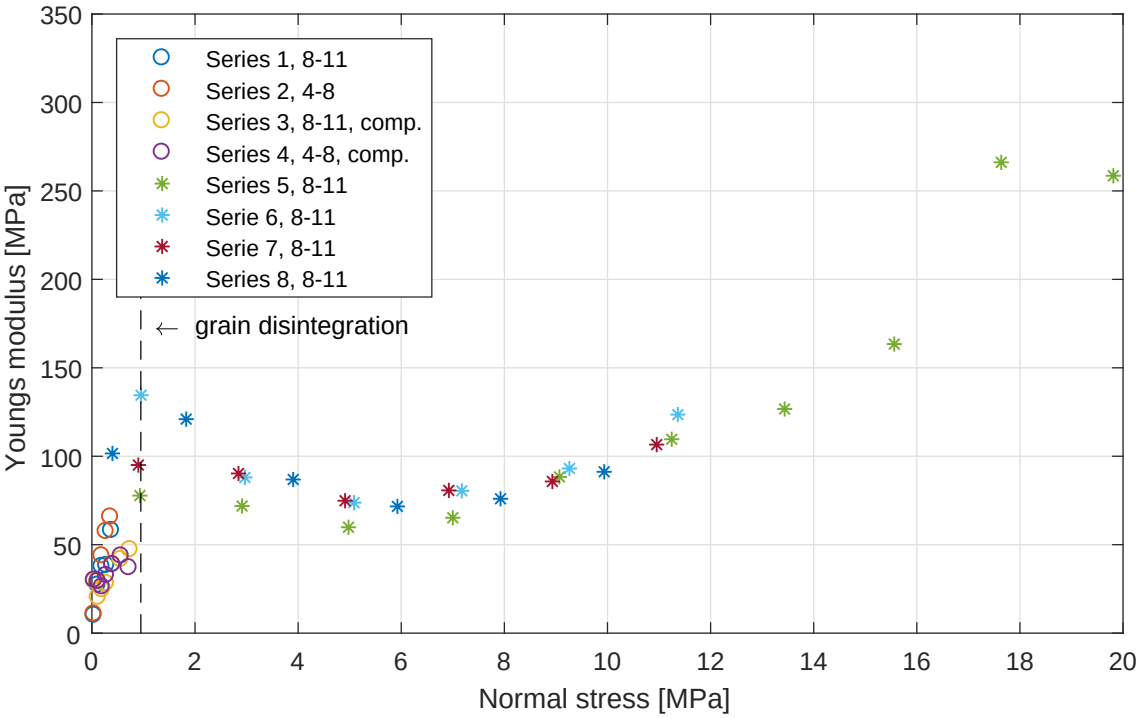

Figure 25: Oedometer constrained modulus development of pea gravel in relation to the normal stress for the first loading cycle ("○" max load level of 1 MPa, "∗" max load level of 20 MPa; comp. ...pea gravel was preloaded).

The comparison of the Young's moduli of Series 1 to 4 depending on the loading type is illustrated in Figure 26. As expected the unloading cycles yield higher values than the reloading cycles with a distinct gap increase compared to the first loading cycle. In the case of first loading, a Young's modulus of 100 MPa is not exceeded with a purely elastic reduction of the pore volume. The Young's modulus development apparently is not affected by a pre loading of the sample nor by the grain size distribution. During unloading and - reloading cycles, a Young's modulus of 100 MPa is already exceeded at a normal stress of approximately 0.10 MPa. The development of the Young's modulus shows a linear behaviour with increasing normal stress. No grain fragmentation was documented for these test series.

3.1.2 Static load plate tests

The static load plate test offers the possibility for the indirect in-situ determination of the load response and compaction of the subsoil. A cylindrical load plate,

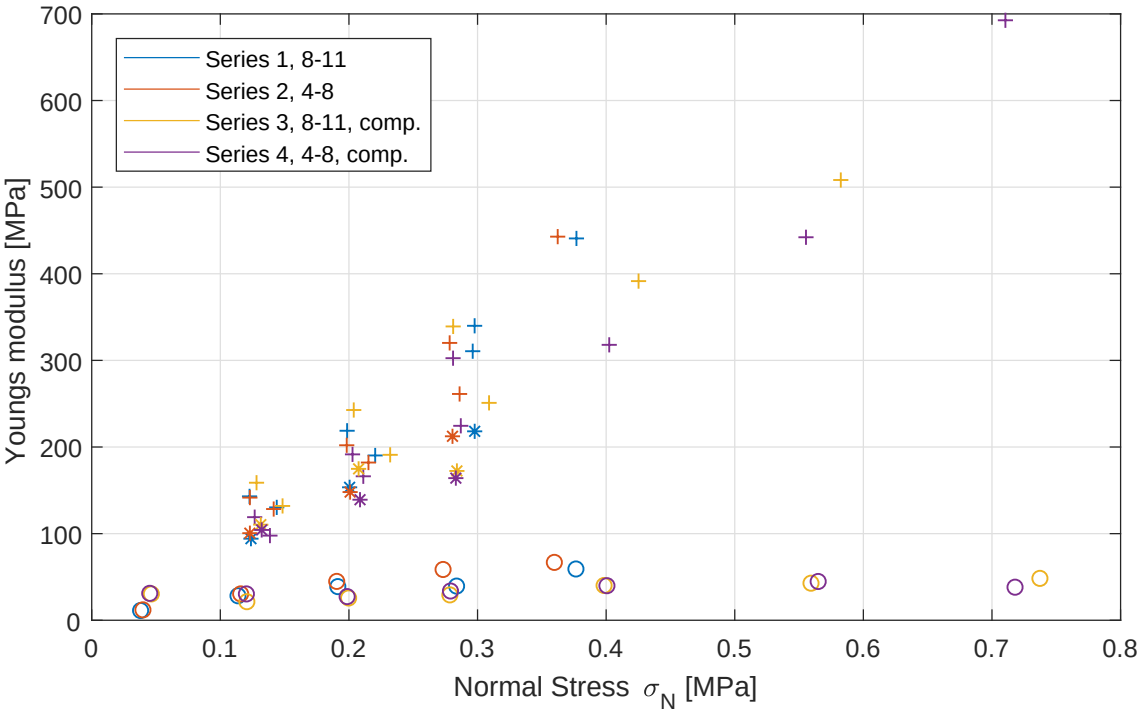

Figure 26: Young's modulus of pea gravel in relation to the stress level and the type of loading ("○" first loading, "+" unloading, "∗" reloading; comp. . . . pea gravel was preloaded).

usually with a diameter of 300 mm is placed onto the investigated material. A hydraulic cylinder supported with a dead weight (truck, digger, compactor, etc.) applies the necessary load on the subsoil. With dial gauges the settlement of the load plate due to the actual load level is measured.

Static load plate tests were performed in order to investigate the deformational behaviour of pea gravel under partially constrained conditions based on the half space theory. Hence, deviations from the results of an oedometer test can be detected. In addition, the characteristic behaviour of pea gravel for the given boundary conditions can be outlined.

3.1.2.1 Test procedure

The test was carried out on an approximately 1 m thick layer of pea gravel in order to avoid influences from the ground below. The tests were performed on pea gravel from series 2 and 4 (see Table 1) with a grain size distribution from 4 to 8 mm. The test configuration can be seen in Figure 27. A total of six tests were executed.

The procedure adopted followed the ÖNORM B 4417 (2018). Due to the low bearing capacity of pea gravel a normal stress of 0.16 MPa was not exceeded. During each test the settlement for first loading, unloading and reloading was documented.

Figure 27: Load plate test on pea gravel.

3.1.2.2 Data evaluation

The data processing was performed according to the solution of Boussinesq (1885) for the vertical surface displacement (settlement) of a continuous, homogeneous, isotropic, linearly elastic half space under loading. Based on this theory the differential settlement of a circular, stiff plate can be written as follows:

$$\Delta s = (1-\nu^2) \cdot \frac{\Delta F}{2 \cdot E \cdot r} \quad \text{with: } \Delta F = \Delta\sigma \cdot r^2 \cdot \pi \tag{9}$$

where:

Δs	.....	differential settlement [m]
ν	.....	Posson's ratio [-]
ΔF	.....	load increment [MN]
$\Delta\sigma$	.....	stress increment [MPa]
E	.....	Young's modulus of the subsoil [MPa]
r	.....	radius of the load plate [m]

Hence, the following equation can be formulated for the differential settlement:

$$\Delta s = (1-\nu^2) \cdot \frac{\Delta\sigma \cdot r \cdot \pi}{2 \cdot E} \tag{10}$$

By reformulating equation 10, the Young's modulus can be expressed as presented in:

$$E = (1 - \nu^2) \cdot \frac{\pi}{2} \cdot r \cdot \frac{\Delta\sigma}{\Delta s} \tag{11}$$

For the evaluation of the load plate test, the value for the Poisson's ratio is commonly assumed with $\nu = 0.214$. Hence, equation 11 can be simplified into the following expression for the deformation modulus E_v:

$$E_v = E \ \ (\text{for } \nu = 0.214) \approx 1.5 \cdot r \cdot \frac{\Delta\sigma}{\Delta s} \tag{12}$$

where: E_v ..... deformation modulus [MPa]

By comparing equation 11 and 12 the relationship between Young's modulus and deformation modulus can be defined as:

$$E = E_v \cdot (2 - \nu^2) \cdot \frac{\pi}{3} \tag{13}$$

The Poisson's ratio was set to 0.2 for the evaluation procedure. This value has proven suitable for non cohesive gravel.

3.1.2.3 Results

The stress – strain relationship for all six load plate tests series is illustrated in Figure 28. In contrast to the oedometer tests, the results show a larger variation. Test series 1 exceeded the ground bearing capacity above the stress level 0.16 MPa. Hence, the test procedure was cancelled at this stage.

The stress dependent Young's moduli is depicted in Figures 29a, 29b and 29c for the loading, unloading and reloading cycles, respectively. The tests do not indicate a distinct correlation with the applied normal stress.

The first loading cycle yields very low values of the Young's modulus which leads to the assumption that the bearing capacity of pea gravel is exceeded at an early stage. For non cohesive and non compactable soils this can be explained due to the low cohesion. During the unloading cycle the Young's modulus ranges between 0 MPa and 800 MPa. The unrealistic upper limit also yields the assumption that pea gravel, if not constrained, experiences shear failure which eliminates the possibility for reversible elastic deformations. This effect does not influence the reloading cycle. Hence, the development of the reloading moduli shows good agreement with the oedometer test results.

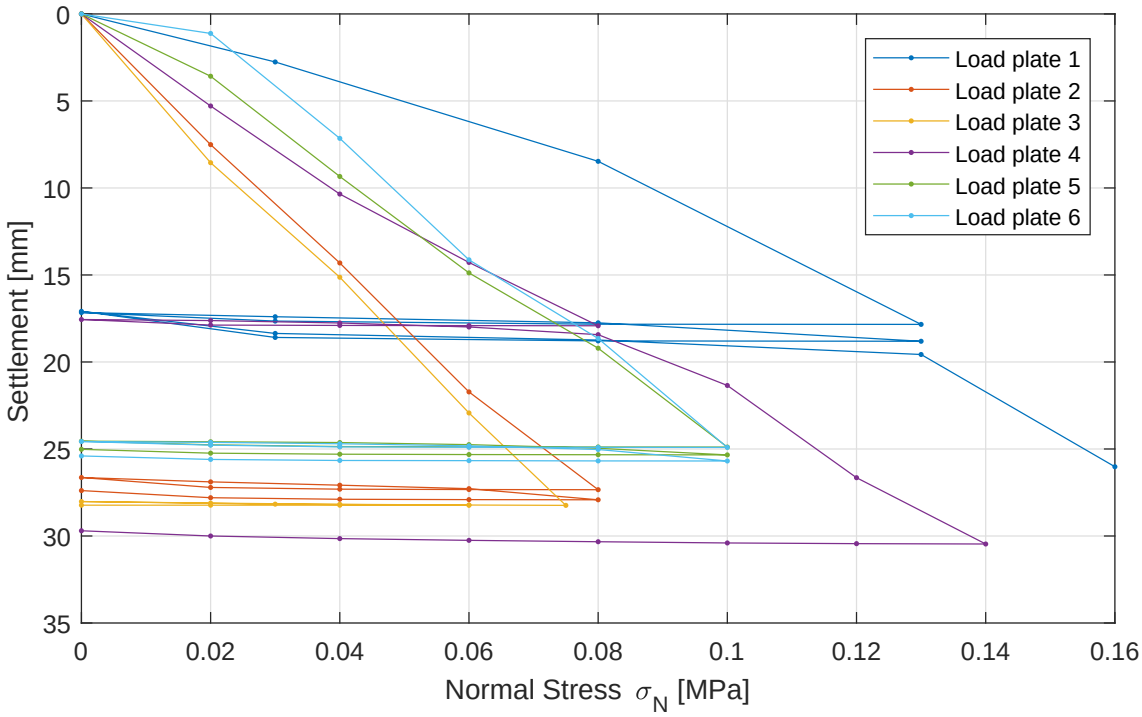

Figure 28: Stress – strain development of the load plate tests.

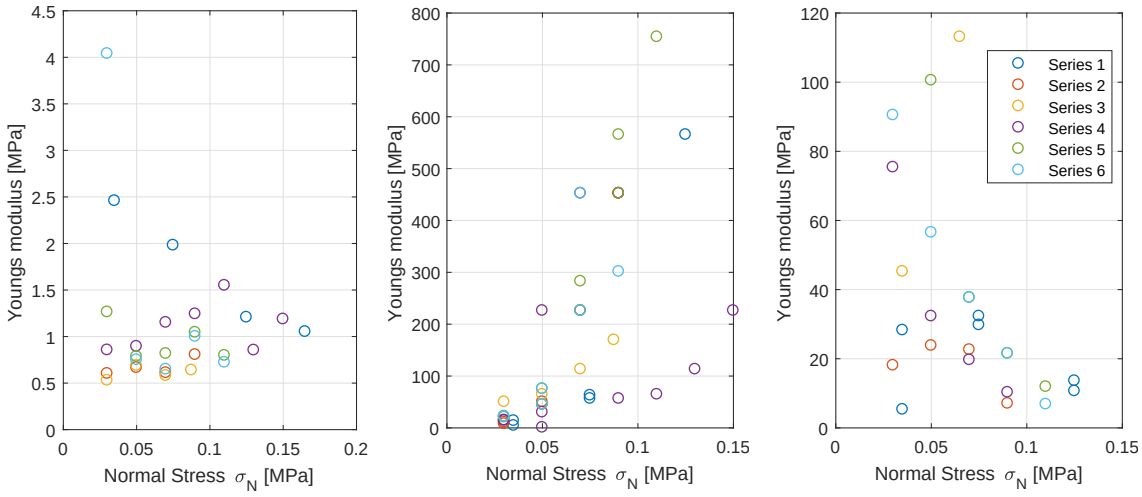

(a) Loading. (b) Unloading. (c) Reloading.

Figure 29: Stress dependent Young's modulus development of pea gravel at the load plate tests.

3.1.3 In-situ Deformation Properties of Pea Gravel

With 32.9 km length, the Koralm base tunnel was divided into three construction lots. With approximately 20 km, construction lot "KAT 2" represents the largest part of the tunnel which is excavated with two DS TBMs. The segmental lining is backfilled with pea gravel. Areas with poor rock mass conditions and cross passages are additionally backfilled with mortar. Nevertheless, pea gravel acts as the primary backfill material behind the shield tail. Hence, the requirement for pea gravel is to immediately provide contact between the segmental lining and the rock

mass. At this project, pea gravel with a grain size range of 8 to 11 mm is used.

Since there are no methods for the in-situ verification of the bedding modulus to date, a measuring device (see Figure 30) has been developed to determine the stress dependent stiffness of the backfill (Lagger, 2016). The measurement is performed throug the radial opening of the lining segments used for the backfilling process.

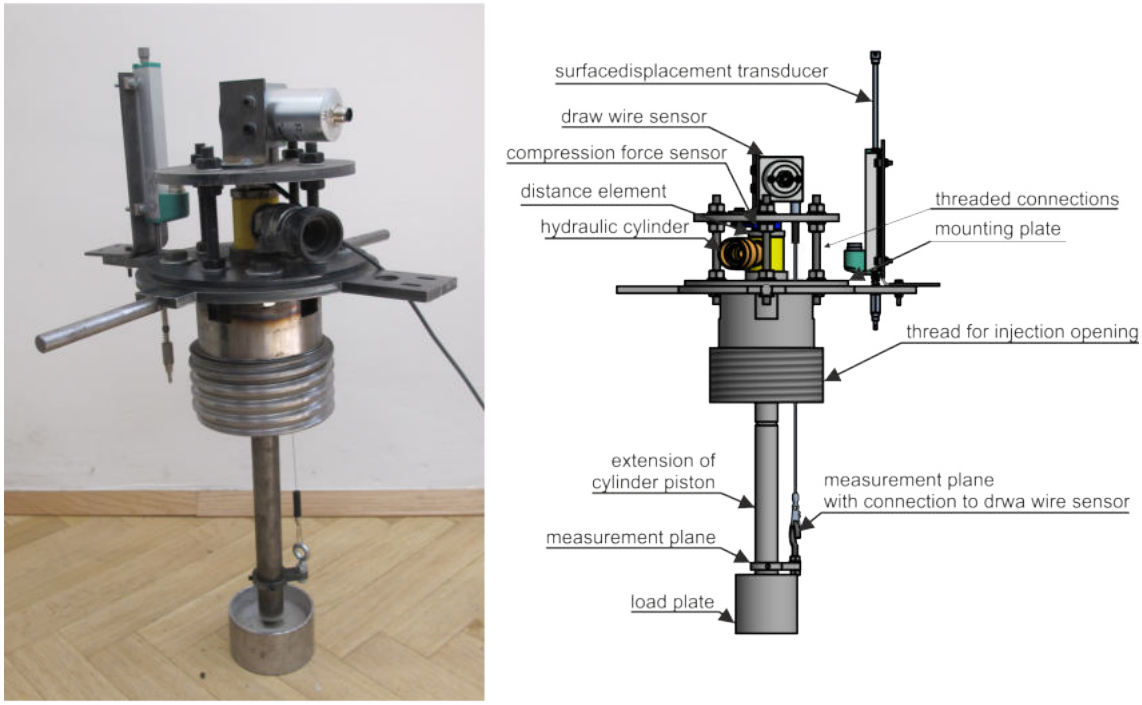

Figure 30: Test apparatus for the in-situ determination of the deformation behaviour of pea gravel (taken from Lagger, 2016).

3.1.3.1 Measurement Concept

As a basis for the development of a measuring concept, field tests for soils were examined for their suitability for determining the deformation properties of coarse grained soils. Hence, the static load plate test ÖNORM B 4417 (2018) was used as a basis since the measured values obtained with this setup allow the direct determination of the deformation modulus E_v. Assuming a continuous, homogeneous, isotropic, linearly elastic half space, the constrained modulus E_s and the Young's modulus E can be calculated with knowledge of the Poisson's ratio (Schultze & Muhs, 1967). At this point it is denoted that the calculated characteristic values and the measuring method are subject to the following restrictions:

- The Poisson's ratio cannot be determined exactly, values from previous experience ranging from 0.15 to 0.25 can be used. In addition, the influence on

the characteristic values E_s and E is only marginal when the Poisson's ratio is changed.

- In contrast to the half space theory, which is used in load plate tests, the boundary conditions in the annular gap are unknown. The influence of "pre-stressing" is therefore included in the test, but cannot be quantified accurately.

Based on the geometry of the backfill openings of the Koralm base tunnel construction lot "KAT2", a prototype for an is-situ plate load test apparatus (Lagger, 2016) was developed, which allows the use in all tunnel areas. The measuring instrument can be mounted by screwing it into the backfill opening. An adaption of the segmental lining is not required (see Figure 31).

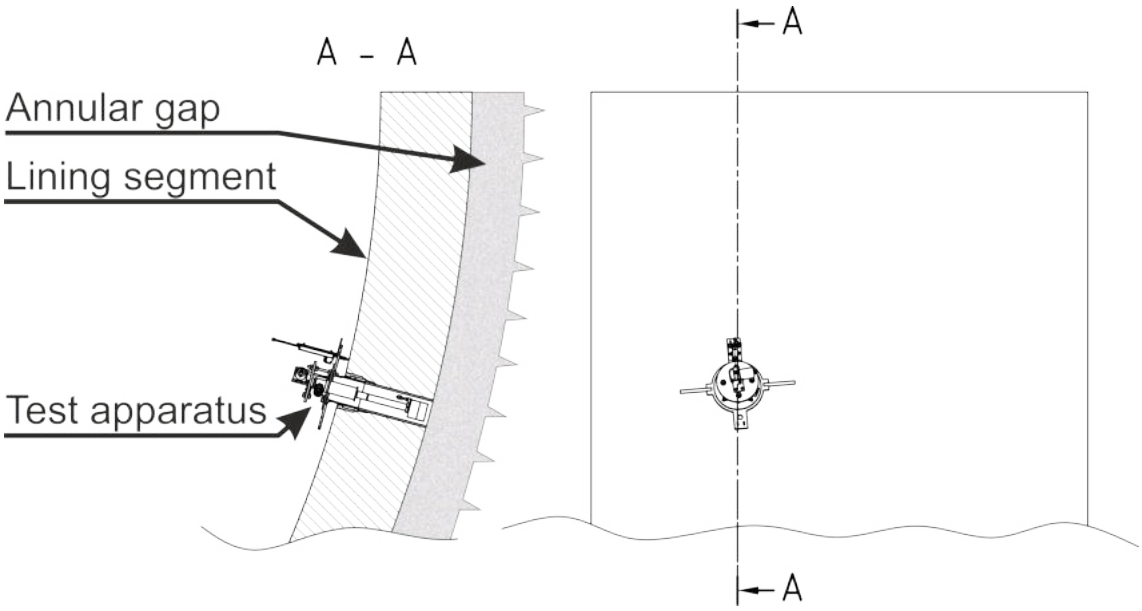

Figure 31: Front view and cross section of the in-situ test setup.

Using a low-pressure hand operated pump and a single-acting hydraulic cylinder, the pea gravel at the end of the backfill opening is loaded with a 68 or 85 mm diameter load plate. The precise control of the applied force is achieved by means of a needle valve with an accuracy of 0.01 kN. The applied force and the displacement of the load plate are recorded continuously. An additional displacement sensor is used to compensate the differential displacements between the test apparatus and the inner surface of the lining. The on-site setup is depicted in Figure 32. A detailed description of the test apparatus can be found in Lagger (2016)

3.1.3.2 On-site measurement

The test procedure is based on the regulations of ÖNORM B 4417 (2018). However, the contact between the load plate and the backfill material occurs only after installation of the measuring device. After the contact has been established, a prestress of 0.02 MPa is maintained for two minutes and the displacement transducers are then reset.

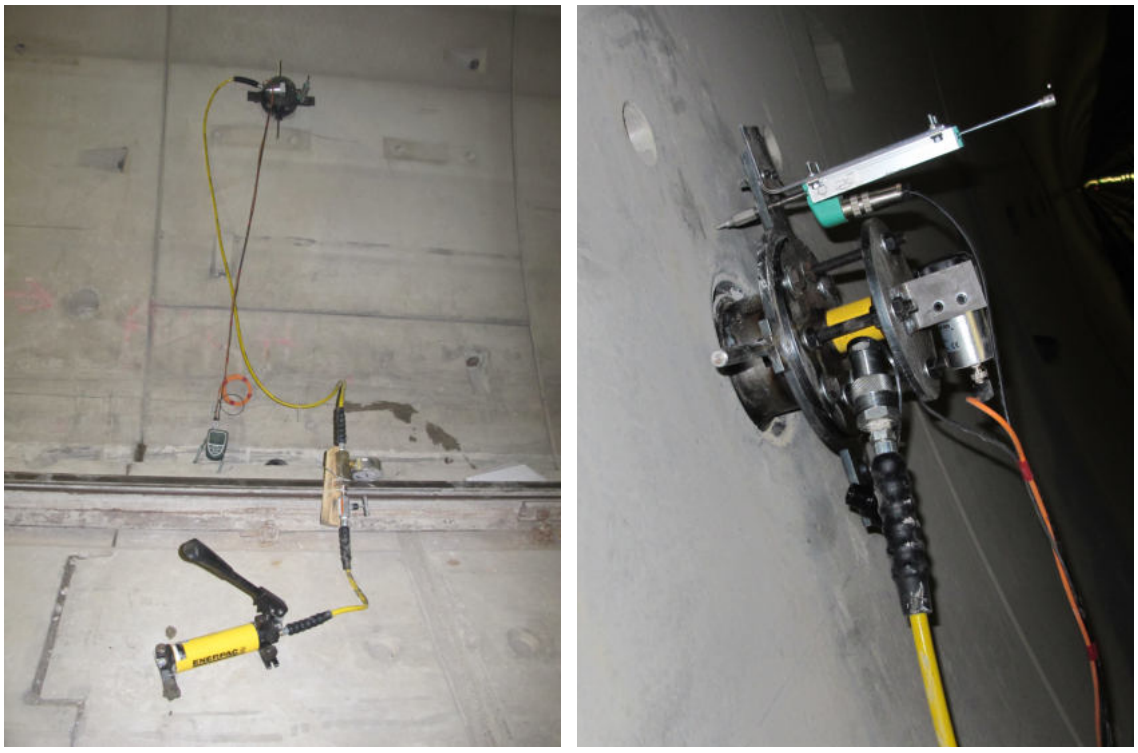

(a) Mounted test apparatus with data logger and hydraulic pump.

(b) Side view of the mounted test apparatus at the 4 o'clock position.

Figure 32: In-situ test apparatus mounted on a pea gravel injection opening.

The stress is gradually increased in steps of 0.10 MPa up to a stress level of 1.20 MPa. In addition to the first loading cycle, two unloading and reloading cycles are carried out with increments of 0.20 MPa each up to the preload stress condition after four initial load steps. After reaching the maximum stress level, stress is reduced in increments of 0.20 MPa. The transition to the following load stage occurs immediately after the rate of displacement drops below 0.02 mm/min.

The evaluation of the tests is carried out after dismantling the test apparatus. The characteristic values are determined in accordance with the ÖNORM B 4417 (2018). The instrument was tested under laboratory conditions prior to the conducted in-situ tests (Lagger, 2016). The tests showed that in the investigated load range, the system deformations are of subordinate importance.

3.1.3.3 Results

Within this project, six tests were executed in areas where no mortar was injected. All at 30° below horizontal level. The geological documentation showed that stable conditions without any breakouts at the excavation boundary are predominant.

Figure 33 presents the results of the in-situ load plate tests. Two series with different load plate diameters (∅ 68 mm and ∅ 85 mm) have been performed. The stress – displacement development, in terms of visual appearance resembles that

obtained with the load plate tests.

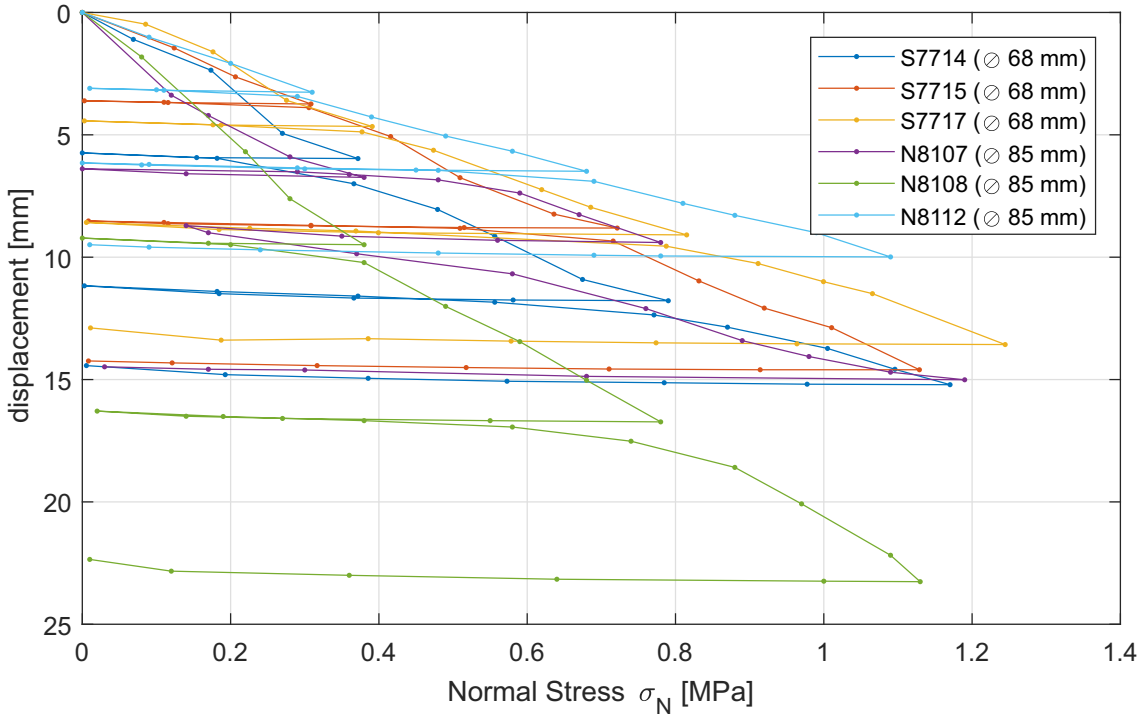

Figure 33: Stress — displacement development of the in-situ load plate tests.

The stress dependent development of the Young's modulus for the in-situ measurements is depicted in Figure 34a, 34b and 34c for the loading, unloading and reloading cycle, respectively. A stress dependent Young's modulus can be identified for all loading types. An influence of the load plate diameter cannot be detected. With higher normal stresses, the deviation of the upper and lower boundary increases significantly. Nevertheless, an expected range of the Young's moduli can be clearly identified. While the unloading and reloading Young's moduli reach 100 MPa at approximately 0.5 MPa, the first loading modulus does not exceed 20 MPa at the maximum load level.

3.1.4 Comparison of Young's moduli

In Figures 35, 36 and 37 the stress dependent Young's moduli for the oedometer test, the static load plate test and the in-situ load plate test are shown. Each Figure represents one loading type.

The comparison of the loading cycles in Figure 35 show that the Young's moduli of the oedometer test yield the highest values. The lower values from the tests with unconfined conditions could be explained by early shear failure of the granular structure. At low stress levels the static load plate tests and the in-situ load plate tests show similar results. This leads to the conclusion, that the confinement at the measured position within the annular gap is comparable with the unconstrained boundary at the load plate test.

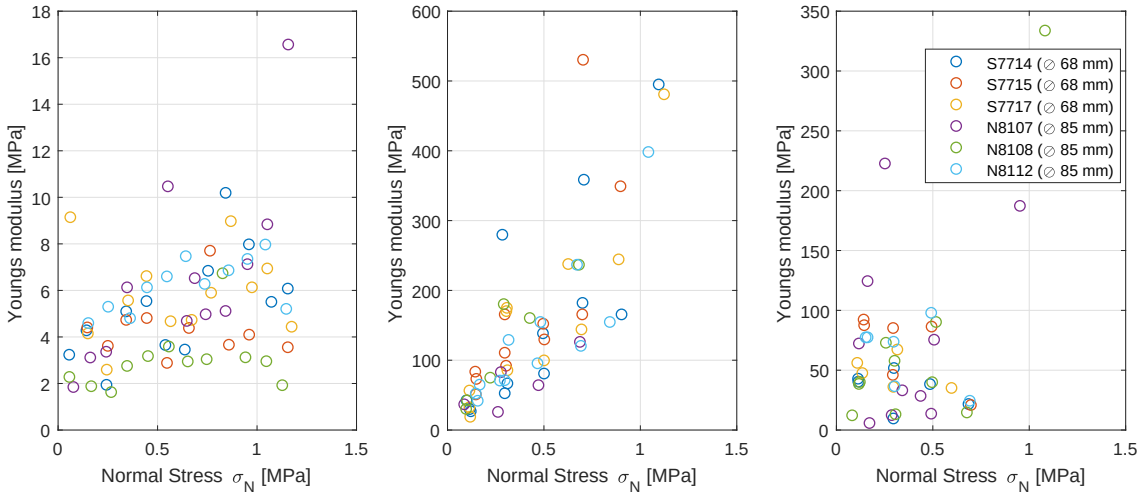

(a) Loading. (b) Unloading. (c) Reloading.

Figure 34: Stress dependent Young's modulus development of pea gravel for the load plate tests.

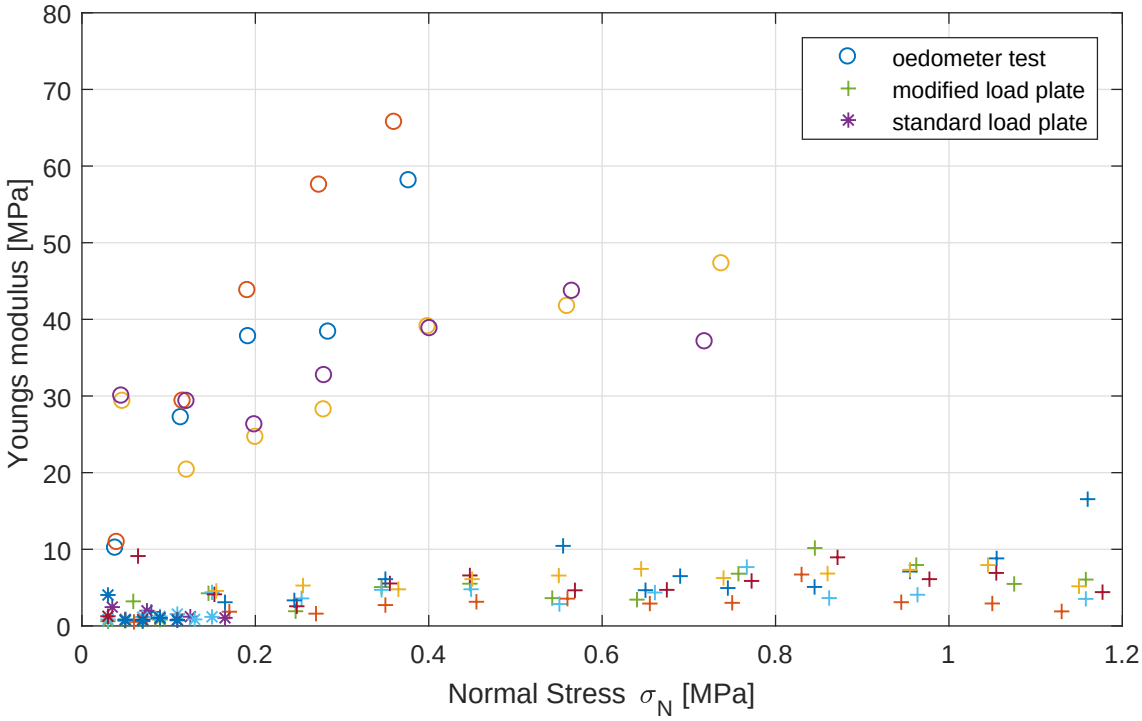

Figure 35: Comparison of the Young's modulus development of the loading cycle for the oedometer, the static load plate and the in-situ load plate test.

The change of the unloading moduli in Figure 36 for the oedometer tests and the in-situ load plate tests shows a similar tendency with increasing normal stress. Nevertheless, the in-situ tests yield lower results, possibly caused by an imperfectly backfilled annular gap. The static load plate test produces unrealisticly high Young's moduli at a very low load level, probably caused by a bearing failure prior to the unloading cycles.

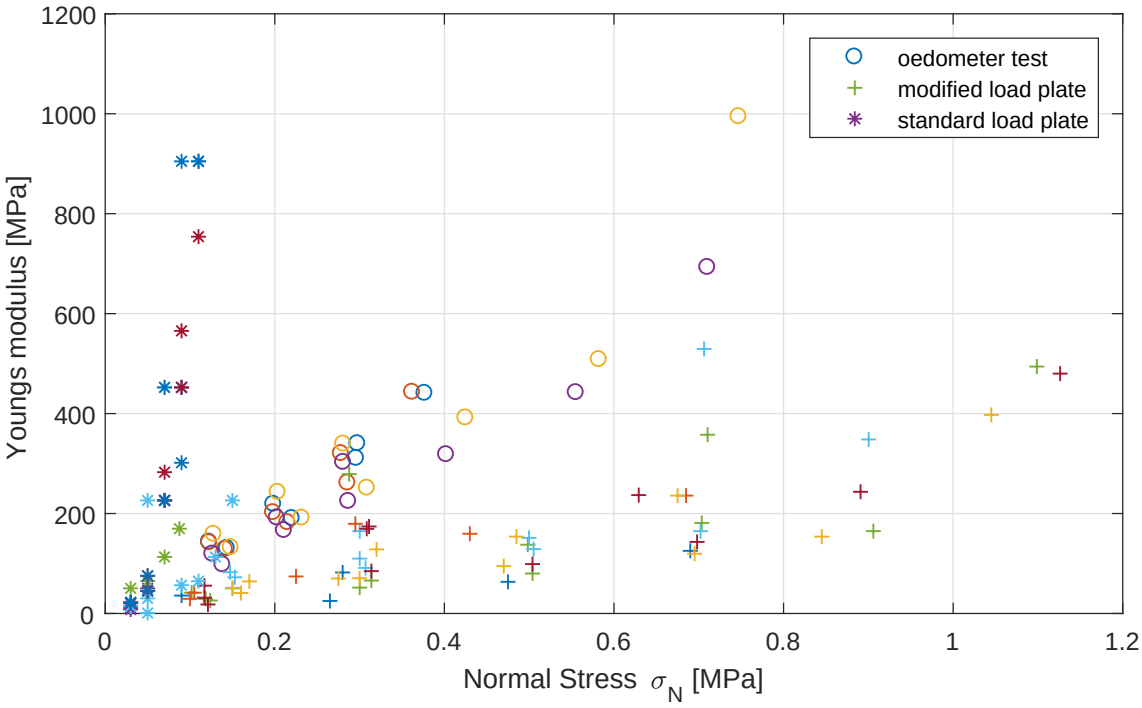

Figure 36: Comparison of the Young's modulus development of the unloading cycle for the oedometer, the static load plate and the in-situ load plate test.

The reloading Young's modulus in Figure 37 yields, as expected, lower values than the unloading moduli. The in-situ load plate tests show a lower stress dependency than the oedometer tests. The static load plate test shows a non linear almost hyperbolic stress dependency.

The results confirm that the elastic response of pea gravel is highly influenced by the type of loading. Except for the large oedometer tests an increase in the Young's modulus with increasing normal stresses especially for first loading and reloading cycles is not significant. This can be attributed to the unconstrained boundary conditions during the in-situ plate load tests. However, it cannot be neglected that the relatively small diameter of the load plate or an incompletely filled annular gap in the measured position influences the results. The unloading cycles depict a clear stress dependency. The static load plate test yields only limited usable results regarding the elastic behaviour which are caused by the rather low cohesive strength of the granular structure, leading to a distinct shear failure at low stress levels. Hence, the strength properties of pea gravel need to be identified.

3.2 Strength properties

In order to confirm the low shear strength of the granular structure of pea gravel, a drained shear test has been performed. For this purpose pea gravel with a grain size range between 8 and 11 mm was used. The test was executed with shear box

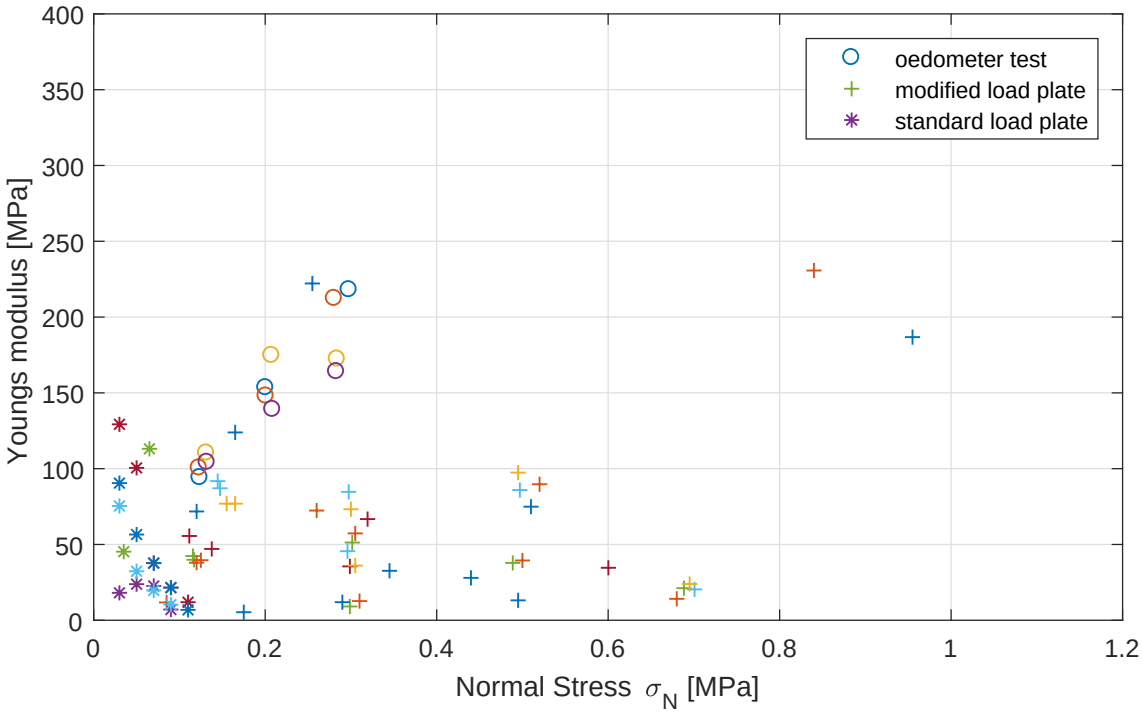

Figure 37: Comparison of the Young's modulus development of the reloading cycle for the oedometer, the static load plate and the in-situ load plate test..

dimensions of 225 mm × 225 mm × 200 mm (width, length, height) and a shear speed of 0.33 mm/min. Due to the low expected stress within the annular gap the normal stress stages have been chosen with 200, 300 and 400 kN/m^2. All tests were executed according to ÖNORM B 4416 (2018).

The plot of the shear stress for the different normal stress levels is presented in Figure 38. The maximum shear displacement ranges from 40 to 60 mm. The peak shear strength parameters are activated at a shear displacement of approximately 10 mm.

Figure 39 illustrates the Mohr – Coulomb failure surface for the peak and residual shear strength. The peak shear strength is defined by a friction angle of 38° and a cohesion of 5 kN/m^2. With further shear displacement the strength decreases, reaching residual values with a friction angle of 28°, and zero cohesion.

The shear strength values lie within the expected range for pea gravel. The results confirm the limited applicability of the static load plate test.

Since, the aim of the investigation lies in the identification of the elastic properties, the strength parameters have been confirmed with a single test. The author stresses, that further investigations are unavoidable for a representative characterisation of pea gravel.

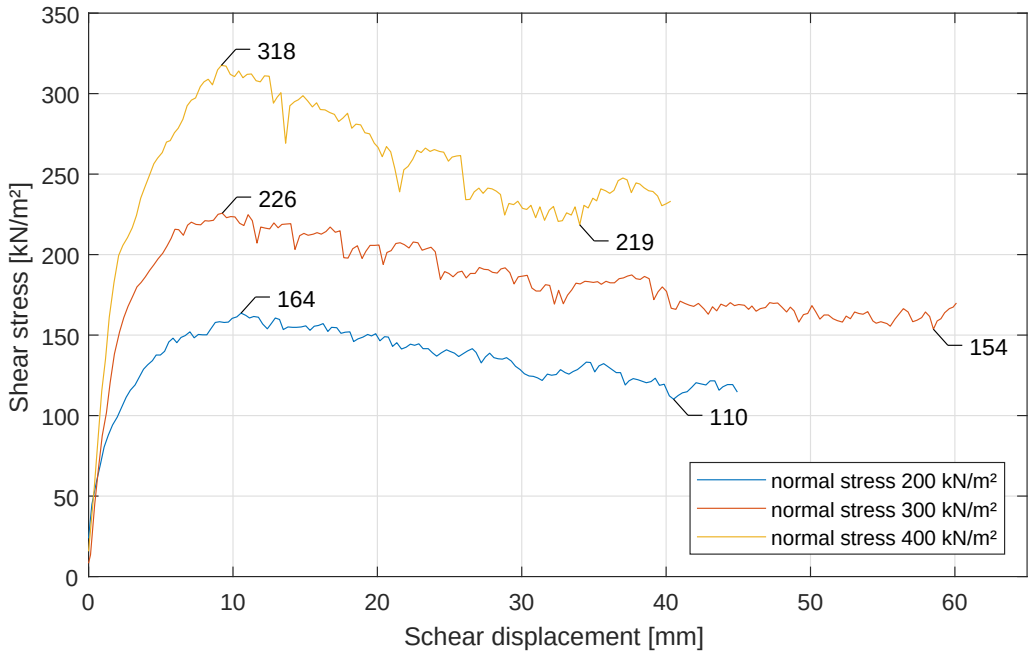

Figure 38: Shear stress – shear displacement development of the shear test.

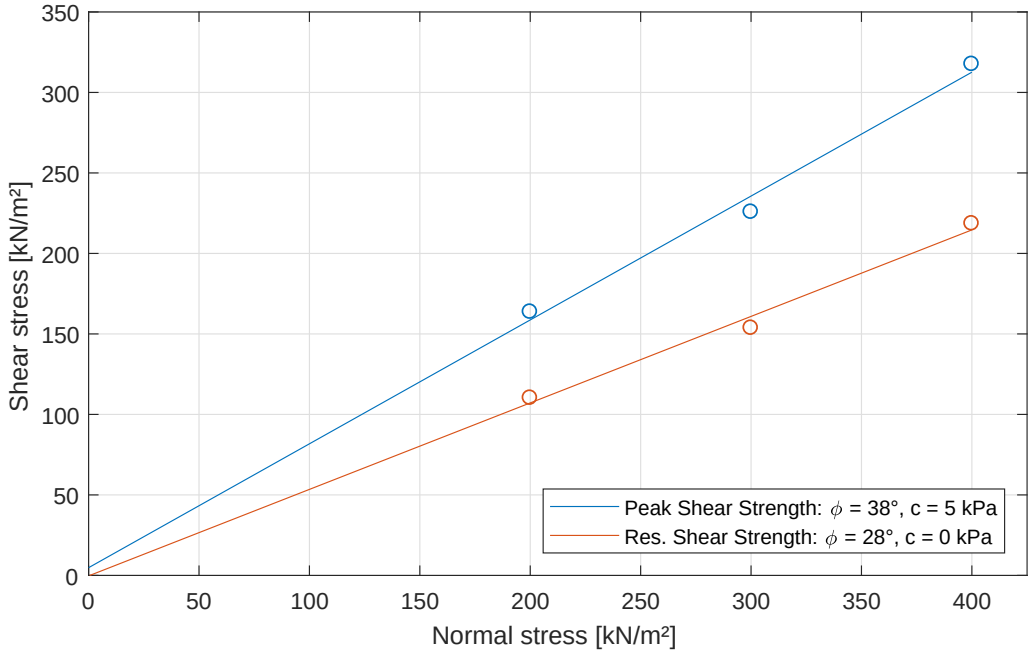

Figure 39: Mohr – Coulomb peak and residual failure surface for pea gravel.

3.3 Relocation behaviour of pea gravel

Due to the abrupt or continuous forward movement of a Shield TBM, pea gravel within the annular gap behind the shield is exposed to a constant relocation process. Hence, scaled model tests have been carried out simulating the relocation behaviour of pea gravel within the annular gap.

In longitudinal direction the annular gap is limited by the outer shield tail seal. While the shield tail of a single shield TBM moves constantly towards the tunnel

face, the shield tail of a double shield TBM performs an abrupt movement. This leads to a distinct slope failure and redistribution of pea gravel within the annular gap. Two different test setups with a model scale of 1:20 have been used in order to investigate this process. To obtain a closely graded material, the fraction between 0.4 mm and 0.5 mm was extracted from a sand sample. Shear tests showed that the sand has a friction angle of 30° and a cohesion of 0 MPa. Hence, a complete model similarity could not be achieved since only geometrical features have been scaled whereas mechanical properties have been neglected.

3.3.1 Planar regripping tests

In order to investigate the failure mechanism of sand in a 2D setup two planar acrylic plates were assembled parallel, with a gap in between. The gap is filled with the above mentioned sand fraction (see Figure 40a). The distance between both acrylic plates was set to 1 cm according to the model scale. This represents an annular gap width of 20 cm and a pea gravel grain size distribution of 8 to 11 mm with the given scale.

Using a Particle Image Velocimetry (Thielicke & Stamhuis, 2014) the failure and deformation process including the wall friction could be identified and quantified. Both, the failure plane angle ϑ_a as well as the repose angle φ (see Figure 40b) have been measured and documented during the relocation process.

To evaluate the influence of the gap width to grain size ratio on the failure plane angle and the repose angle, the spacing between the two acrylic plates was increased stepwise. It has to be stated that by increasing the spacing the geometrical model similarity does no longer meet the original model scale.

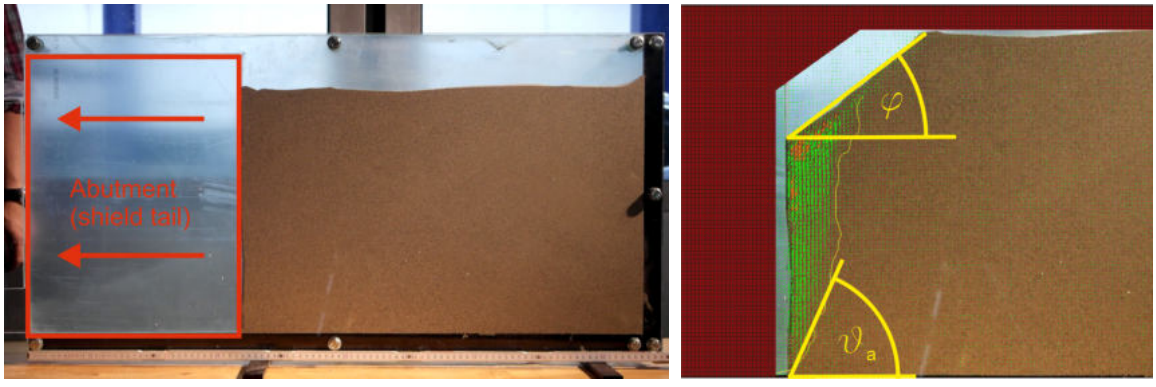

(a) Test setup.

(b) Planar gap failure model identifying the angle of repose (φ) and the failure plane angle (ϑ_a) (taken from Henzinger et al., 2016).

Figure 40: Planar regripping test.

3.3.1.1 Results

Figure 41 shows the results of the planar model tests with different spacing between the two acrylic plates. The blue series shows the directly measured failure plane angle of the soil body. The red series represents the back calculated values using the repose angle by applying Coulomb's limit equilibrium theory for the lateral earth pressure:

$$\vartheta_a = 45 + \frac{\varphi}{2} \tag{14}$$

where: ϑ_a ..... active failure plane angle [°]
φ ..... repose angle [°]

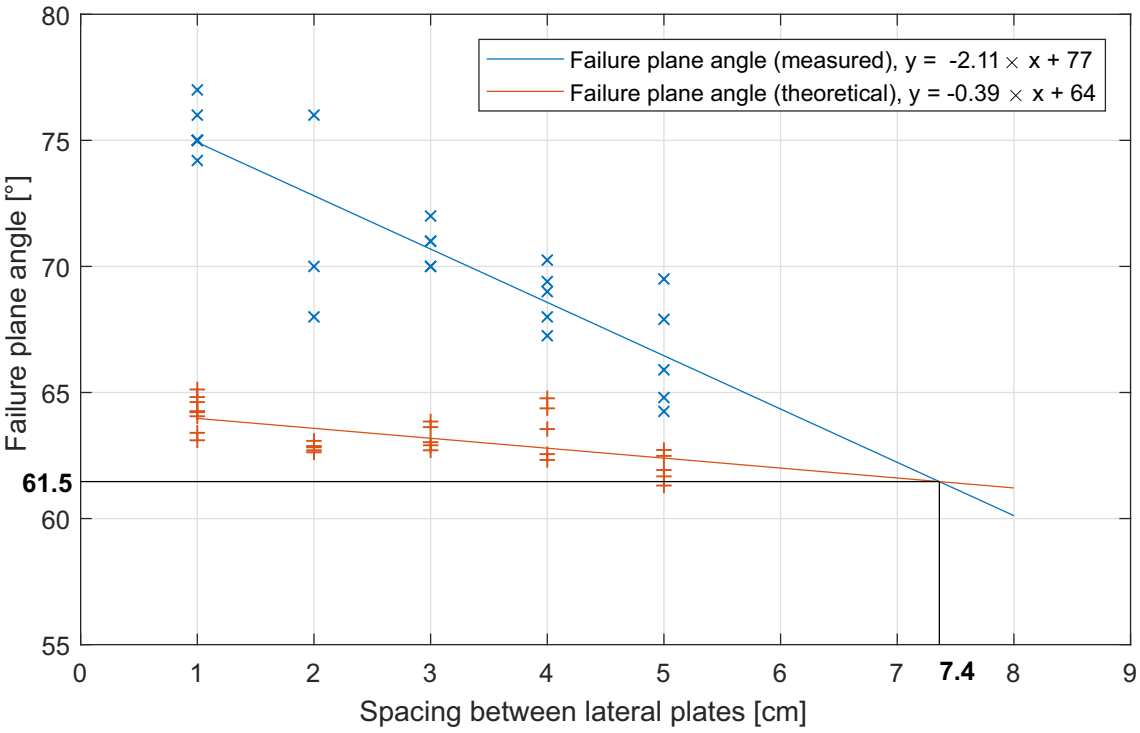

Figure 41: Dependency of the spacing on the theoretical and measured failure plane angle (blue: measured failure plane angle using PIV (Thielicke & Stamhuis, 2014); red theoretical failure plane angle using Coulomb's limit equilibrium theory for the lateral earth pressure with the angle of repose as friction angle; taken from Henzinger et al., 2016).

Both angles are differently influenced by the gap width. With increasing gap width, the failure plane angle decreases more than the angle of repose. Both show a linear response to the increasing gap width. The intersection of both trend lines, which have been extrapolated, indicates the theoretical influence limit of the wall friction at a spacing of 7.4 cm. Hence, the gap width to grain size ratio results in 14.8 to 18.5 with a grain size of 0.4 to 0.5 mm. With a failure angle of 61.5° at the given spacing of 7.4 cm the friction angle according to Coulomb's theory is backcalculated to 33° which is in good agreement with the laboratory test results,

with a friction angle of 30°.

3.3.2 Circular regripping tests

To illustrate the relocation behaviour within the annular gap incorporating a position dependent circular wall friction due to the different contact forces between backfill and contact surface, a test setup was developed which can realistically illustrate the regripping process (see Figure 42). Plastic pipes representing the segmental lining, excavation boundary and shield tail were used for the model. For documentation purposes an acrylic glass pipe was used for the excavation boundary. In order to simulate the abrupt regripping process of the shield tail, a crank mechanism was installed, allowing to move the middle pipe, representing the shield tail in axial direction.

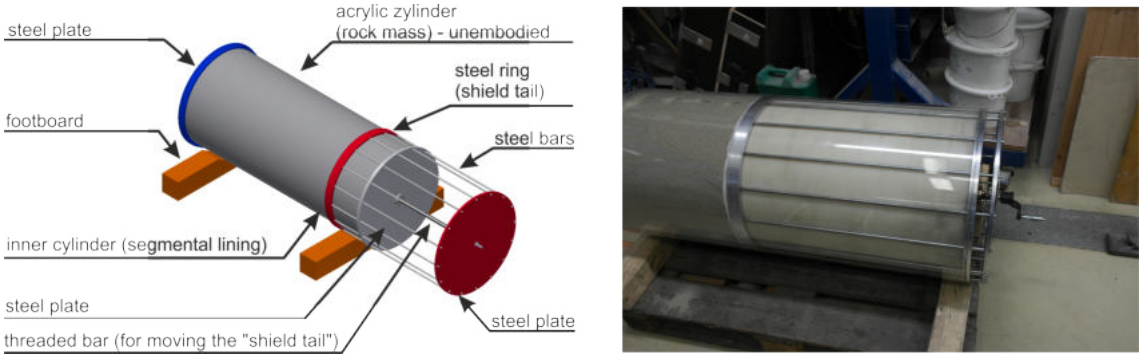

Figure 42: Circular test setup (taken from Henzinger et al., 2016).

During movement of the ”shield” the relocation process was continuously documented with focus on the development of the angle of repose of the backfilling material. The evaluated data have shown, that during and after the experiment the angle of repose at the side wall corresponds to the inner friction angle of the used sand fraction. Strong deviations were detected especially within the crown and invert area. Due to the frictional resistance, the invert area stays unaffected by the relocation process. Figure 43 depicts the relocation process of the circular test setup for different “shield tail” positions.

3.3.3 Results

The results of the scaled model tests on the relocation behaviour of pea gravel have shown that the unfavourable bedding distribution behind the shield tail is unavoidable and mainly triggered by the retraction of the TBM shield. On the basis of both the laboratory tests and the results obtained can be summarised as follows:

- The gap width to grain size ratio influences the size of the failing soil body and thus the relocation behaviour. Gap widths from approximately 15 to 18

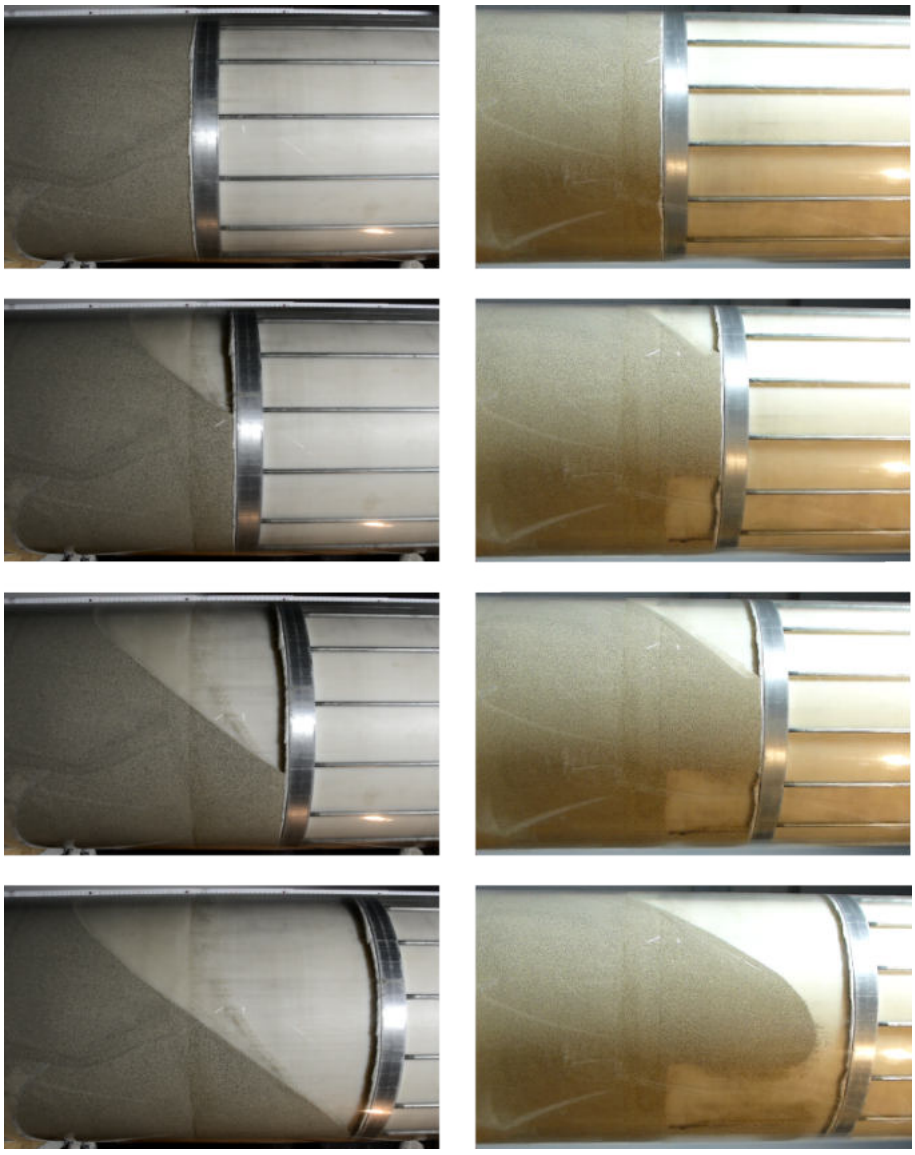

Figure 43: Progressing test procedure from top to bottom (viewing direction towards the longitudinal tunnel axis from outside the annular gap; left: horizontal view of side wall; right: view 45° upwards, showing also invert).

times the grain diameter are large enough to prevent arching effects.

- The relocation process forms a cone shaped transition between bedded and unbedded areas. The repose angle of the cone is slightly higher than the inner friction angle of pea gravel due to the wall friction and arching effects.
- Due to the frictional resistance, the segments in the invert are unaffected by the relocation process. Hence, the importance of a separate backfill of this area is stressed.
- The relocation process of pea gravel within the annular gap is additionally favoured by the abrupt regripping process of a Double Shield TBM. The height of the transition zone between bedded and unbedded areas at the shield tail seal depends on the regripping length and the initial filling level of the annular gap.

3.4 In-situ pea gravel detection within the annular gap using ground penetrating radar

The ground penetrating radar is an electromagnetic impulse – reflection method. The used device consists of an antenna and a receiver. The antenna transmits energy into the subsurface which propagates depending on the electromagnetic properties of the individual media. At the boundary of two different media, a part of the energy is reflected and captured by the receiver. The GPR device records the time difference (two-way travel time) between the outgoing signal and the incoming signal as well as the amplitude of the incoming signal. The GPR device is moved constantly along a defined surface profile, measuring with regular and defined time intervals. By aligning each single measurement horizontally a GPR – profile can be plotted.

3.4.1 Propagation of electromagnetic waves

The propagation of electromagnetic and elastic waves show similarities. Nevertheless, some basic differences influence the applicability and the processing of signals. Especially the coupling between electric and magnetic field vectors draw a distinct line to other geophysical methods. The link between electric and magnetic field vectors and the wave propagation behaviour is based on the Maxwell equations which are described in the literature (Jol, 2009).

3.4.1.1 Material properties

The propagation velocity and the absorption rate of electromagnetic waves strongly depends on the used antenna frequencies. In addition electrical properties of the investigated materials have great influence. These are represented by the dielectric permittivity ε, the electrical conductivity σ and the magnetic permeability μ. These parameters are interdependent.

The relative dielectric permittivity ε_r is the physical key parameter for the given scenario. It describes the ability of a material to store electricity when an external electric field is applied. It is defined as the ratio of the absolute dielectric permittivity ε to the absolute dielectric permittivity of vacuum ε_0 and is therefore dimensionless and frequency dependent:

$$\varepsilon_r(\omega) = \frac{\varepsilon(\omega)}{\varepsilon_0(\omega)} \tag{15}$$

where: $\varepsilon_r(\omega)$ ..... relative dielectric permittivity [-]
$\varepsilon(\omega)$ ..... absolute dielectric permittivity $\left[\frac{\mathrm{A \cdot s}}{\mathrm{V \cdot m}}\right]$
$\varepsilon_0(\omega)$ ..... absolute dielectric permittivity of vacuum $8.8544 \cdot 10^{-12}$ $\left[\frac{\mathrm{A \cdot s}}{\mathrm{V \cdot m}}\right]$
ω ..... angular frequency [s^{-1}]

Although in this case not strictly an issue, it has to be mentioned that the relative dielectric permittivity is a complex function. Since most engineering materials show low conductivity, the relative permittivity is reduced to its real part. Electromagnetic waves travel faster through media with low dielectric permitivities.

The electrical conductivity σ provides a measure for the ability to conduct an electric current. In the case of a segmental lining, an electric current is applied at the reinforcement causing an attenuation of the applied electromagnetic field.

The magnetic permeability μ , similar to the electrical conductivity, represents a measure for a material to be magnetized upon exposure to an electromagnetic field. With increasing magnetic permeability, the attenuation of the emitted energy decreases. Most engineering materials show a minimal amount of magnetic permeability. Hence, the magnetic permeability can be neglected in most cases ($\mu = 1$).

3.4.1.2 Signal properties

The electromagnetic frequency ω indicates the oscillating frequency of the emitted wavelet. The wavelength λ is interdependent with the frequency as depicted in the following relation:

$$\lambda = \frac{c}{f} \tag{16}$$

where: λ ..... wavelength [m]
c ..... velocity of EM wave in vacuum = $3 \cdot 10^8$ [m/s]
f ..... frequency [1/s]

Hence, low frequencies produce high wave lengths and vice versa. The wavelength is the main indicator for the penetration depth and the resolution of the investigated profile. Increasing frequencies relate to higher resolution capabilities and lower penetration depths. Hence, the electromagnetic frequency has to be evaluated according to the given problem in order to guarantee a satisfying resolution with a sufficient penetration depth.

3.4.1.3 Characteristics for the detection of voids

For the detection of voids it is necessary to be able to distinguish between a backfilled and a non properly backfilled annular gap. With the electromagnetic methods two characteristics can be used to differentiate these cases.

Reflection characteristic: When electromagnetic waves encounter a boundary between two materials with different dielectric permittivities ε_r, a reflected and transmitted wave signal is created. Hence, an amplitude is illustrated in the radargram. The size of the reflection can be calculated for a boundary perpendicular to the emitted wave by the reflection coefficient r:

$$r = \frac{\sqrt{\varepsilon_{r_1}} - \sqrt{\varepsilon_{r_2}}}{\sqrt{\varepsilon_{r_1}} + \sqrt{\varepsilon_{r_2}}} \tag{17}$$

where: r ..... reflection coefficient [-]
ε_{r_1} ..... dielectric permittivity of first medium $\left[\frac{\text{A·s}}{\text{V·m}}\right]$
ε_{r_2} ..... dielectric permittivity of second medium $\left[\frac{\text{A·s}}{\text{V·m}}\right]$

With increasing differences in the dielectric permittivities between consecutive layers, the reflection coefficient increases. Table 2 provides literature values for the dielectric permittivitiy ε_r for the involved materials.

Table 2: Literature examples for dielectric permittivities ε_r.

Material	ε_r $\left[\frac{\text{A·s}}{\text{V·m}}\right]$
hydrated concrete	~ 7
air	1
water	80 (20 °C)
gravel	~ 5.5

With equation 17 it can be seen that a transition between concrete and air or water causes a much higher reflection coeffeicient (concrete – air. $r = 0.45$; concrete – water: $r = -0.54$) than concrete and dry gravel (concrete – gravel $r = 0.06$). Negative reflection coefficients denote a phase reversal in the reflected amplitude. Hence, the reflection characteristic is the first feature which can be drawn to identify the material within the annular gap.

Reflection time: The velocity of electromagnetic waves for a specific medium is a function of the dielectric permittivity ε_r. Hence, for non magnetic materials the real part of the velocity is given by:

$$v = \frac{c}{\sqrt{\varepsilon_r}} \tag{18}$$

where: v ..... velocity of the EM wave [m/s]
c ..... velocity of EM wave in vacuum = $3 \cdot 10^8$ [m/s]
ε_r ..... dielectric permittivity $\left[\frac{\mathrm{A \cdot s}}{\mathrm{V \cdot m}}\right]$

With the known velocity the layer thickness can be calculated with the two-way travel time Δt accordingly:

$$d = v \cdot \frac{\Delta t}{2} \tag{19}$$

where: v ..... velocity of the EM wave [m/s]
Δt ..... two-way travel time [s]

In the case of the annular gap, the thickness of the layer is known. Hence, the expected two-way travel time Δt can be expressed as:

$$\Delta t = \frac{d \cdot 2 \cdot \sqrt{\varepsilon_r}}{c} \tag{20}$$

With the electric permittivities listed in Table 2, the measured travel time represents the second feature for the identification of the annular gap backfill.

3.4.2 Methodology for the void detection in the annular gap

The GPR technology is well approved for imaging subsurface profiles with the focus on cavity and layer thickness detection. The thickness of a layer can be determined by using the travel time of a reflected radar impulse, when the electromagnetic properties are known. The amplitude of reflections at the interface of two different media is a function of the contrast in the electrical properties. In the given situation reinforced lining segments with a thickness of 35 cm were used. The transition between the annular gap, filled with pea gravel and an empty or water-filled annular gap is to be detected. The double reinforcement layers represent the limiting element. Figure 44 shows the influence of the reinforcement on the wave propagation with a numerical simulation.

In order to provide a systematic approach for the given problem, the following procedure has been elaborated and executed for the quality control of the annular gap backfill:

1. Modelling of the electromagnetic wave propagation incorporating all relevant influencing materials including lining, reinforcement, backfill and rock mass. This step should give an overview of the measurable distinction between a

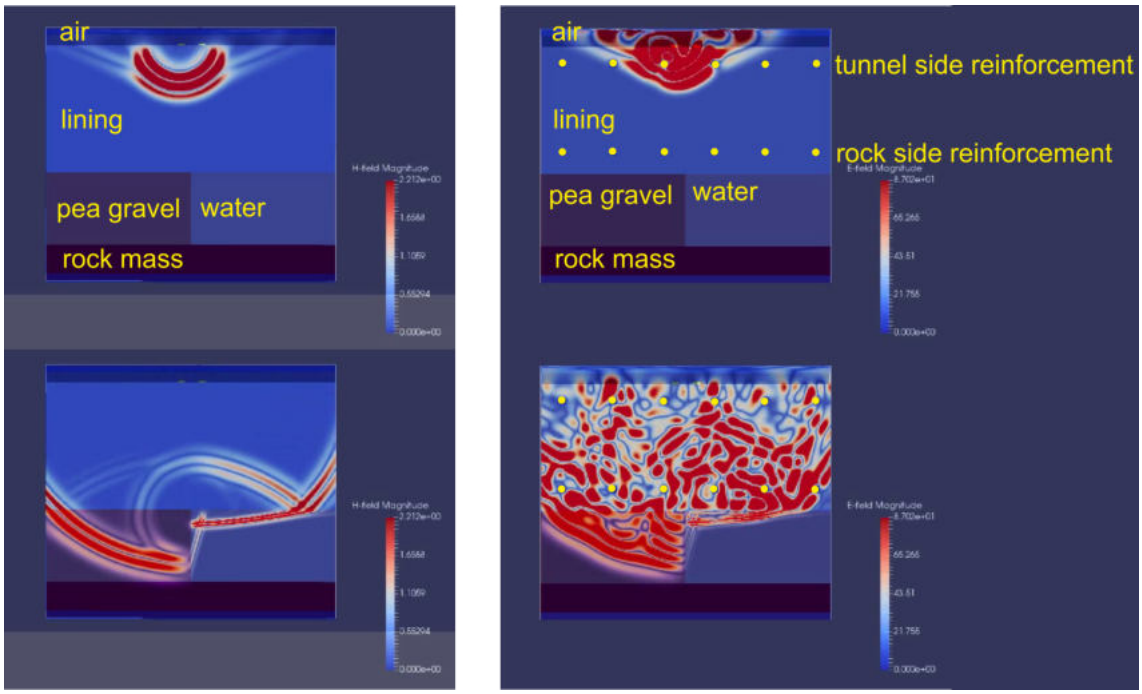

Figure 44: Propagation paths of electromagnetic waves through a lining segment (left: unreinforced, right: reinforced) followed by an annular gap; top: transmitted electromagnetic waves penetrate the lining; bottom: reflections at the interface between lining segment to pea gravel and water (taken from Lammer-Stecher, 2017).

backfilled and non backfilled annular gap with variation of the reinforcement spacing and electromagnetic frequency.

2. Determination of the dielectric permittivity ε_r with calibration measurements under defined boundary conditions.
3. Measurement of different backfill scenarios on analogue models. This should provide a first impression of the detectability of non backfilled and backfilled annular gap under a controlled measurement setup.
4. Measurements underground on installed lining segments with a distinct transition between backfill and air filled void.

The GPR investigations were carried out by order of the Austrian Federal Railways (ÖBB-Infrastruktur AG) under the administration of the Institute of Rock Mechanics and Tunnelling. Numerical investigations have been carried out in collaboration with GeoHiRes International GmbH. The component measurements, the analogue tests and the underground investigations have been executed in collaboration with WILLMES Bauwerksprüfung.

3.4.3 Numerical Analysis

Due to the limited variation of the electromagnetic parameters and the absence of material based non-linearity, numerical simulations were carried out in order to ascertain the possible use of a GPR measurement. The numerical finite difference Software GPRmax2D (Warren et al., 2016) was used in order to investigate the suitability of GPR methods for the given task.

3.4.3.1 Numerical model

The numerical model consists of a combination of different material regions. The discretization is illustrated in Figure 45. The horizontal length and the depth of the model were chosen to be 0.8 m and 0.7 m respectively. This accounts for the lateral extent of a backfilled and "empty" annular gap as well as the lining segment, the reinforcement, the annular gap and the rock mass. In addition, the free space on the interior edge of the lining segments due to the thickness of the antenna is incorporated.

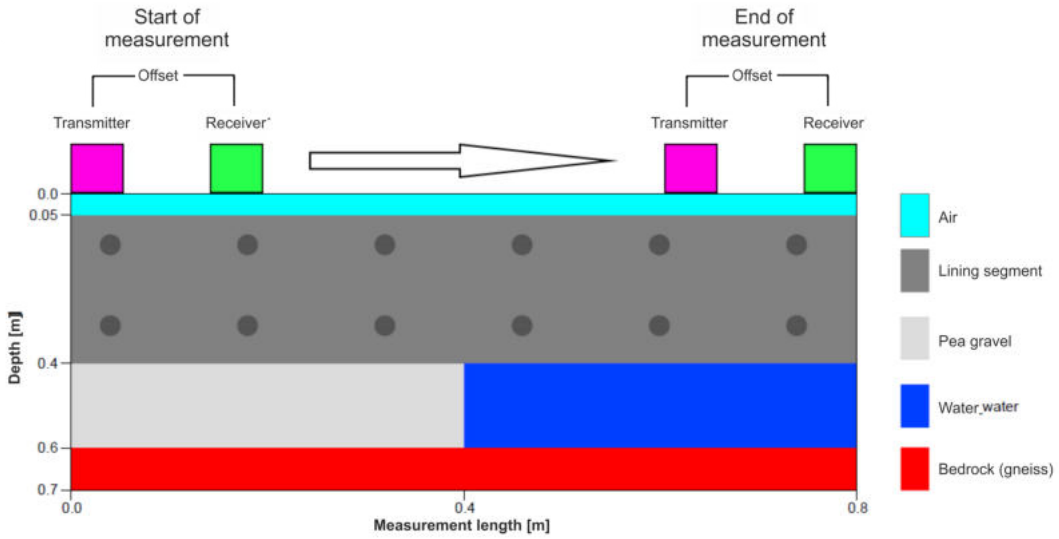

Figure 45: Numerical model for GPR measurements (taken from Lammer-Stecher, 2017).

The thickness of the segmental lining was chosen to be 0.35 m, the annular gap filling or cavities 0.20 m. Gneiss was assumed as the surrounding rock mass behind the annular gap. The diameter of the reinforcement rebars in the model was chosen to be 10 mm according to the commonly used dimensions. The simulation was carried out by moving the antenna, consisting of transmitter and receiver from the top left to the top right position as outlined in Figure 45.

3.4.3.2 Evaluation Methodology

In order to evaluate the possibility for the localization of bedding imperfections and to illustrate the limitations, a sensitivity analysis has been performed, varying the spacing of the reinforcement, the antenna frequency and the void filling. With a constant geometry, the spacing of the upper and lower reinforcement has been varied between 6 and 14 cm in steps of 2 cm. The antenna frequency has then been varied, using the common values 400, 900, 1000 and 1600 MHz. The parameters for the void filling were switched between air and water.

With the one-way travel times for the individual materials and their corresponding thickness (see Table 3), the associated reflections in the radargrams can be identified.

Table 3: One-way travel times of electromagnetic waves.

Material	thickness [m]	one-way travel time [ns]
air	0.05	0.33
concrete	0.35	6.18
pea gravel	0.20	3.27
water – void	0.2	11.95
air – void	0.2	1.33

Since the emitted electromagnetic waves are subject to a constant damping due to the material properties, reflections from deeper boundaries appear with smaller amplitudes. Hence, the time-gain method was applied, amplifying the reflected signal with increasing time according to a mathematical function. The effect of the post processing is illustrated in Figure 46. In this case, a model without reinforcement and water filled void was used. The influence of the backfilling is illustrated in the right figure, whereas the left figure shows the raw data. All numerical results have been processed using this method.

3.4.3.3 Results

The radargrams showing the transition between dry pea gravel and water filled voids are depicted in Figure 47 for an antenna frequency of 1600 MHz. A reinforcement spacing of 12 cm and 8 cm was modelled. Two wavelets showing the reflection of single impulses are illustrated in the lower image for the pea gravel filled and water filled annular gap. Both reinforcement spacings show that the void is detectable by means of the reflection characteristic at the rear side of the segments rather than by different travel times through the annular gap.

The results of the numerical modelling showed that cavities were detectable under most of the conditions assumed in the different models. However, this was only

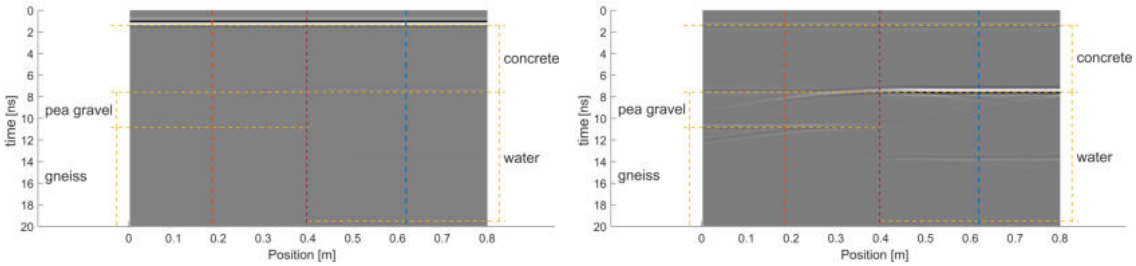

(a) Radargram without post processing.

(b) Radargram with post processing.

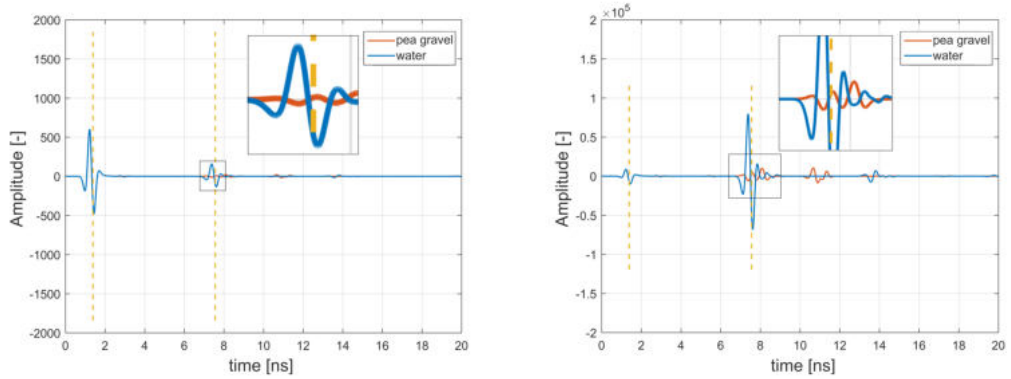

(c) Single scan without post processing.

(d) Single scan with post processing.

Figure 46: Post processing of radargrams. Antenna frequency set to 1000 MHz and the void is filled with water without reinforement (taken from Lammer-Stecher, 2017).

valid with restrictions up to a reinforcement distance of 8 cm. For the given task, the 1600 MHz antenna proved to be the most suitable choice. If locally increased attenuation of georadar waves should occur, the frequency of 1000 MHz could be used alternatively or additionally. Based on the numerical results, the feasibility of the measurements was proven. Hence, actual georadar measurements on the analogue model as well as in the tunnel could be performed. Detailed description of the results can be found in Lammer-Stecher (2017) and Kathage (2016).

3.4.4 Measurement of the Components

To determine the relative dielectric permittivity ε_r of the used components, mortar, mortar – pea gravel mixture, pea gravel, and excavated material, radar measurements were carried out. On pea gravel and the excavated material different saturation conditions shall provide a broader knowledge of the expectable values.

3.4.4.1 Test set-up

Wooden boxes with the dimensions L x W x H of 50 x 50 x 20 cm (see Figure 48), were filled with the respective material. While carrying out the radar measurements a 20 mm plastic plate was placed on top of the boxes. The bottom of

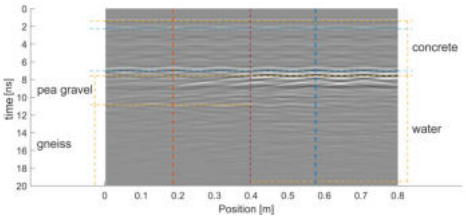

(a) Radargram for 12 cm reinforcement spacing.

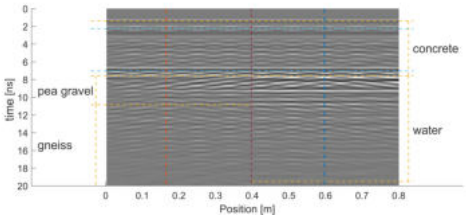

(b) Radargram for 8 cm reinforcement spacing.

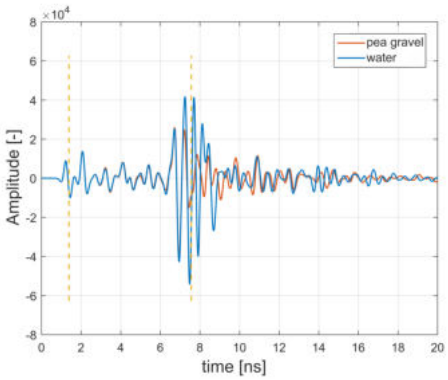

(c) Single wavelets for 12 cm reinforcement spacing.

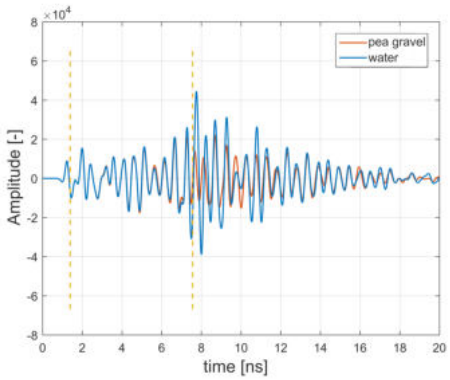

(d) Single wavelets for 8 cm reinforcement spacing.

Figure 47: Radargrams depicting the transition between dry pea gravel and water filled voids measured with an antenna frequency of 1600 MHz (taken from Lammer-Stecher, 2017).

the box was covered with an aluminium foil. The aim of the measurements was to identify significant reflections from the bottom of the box and to determine the permittivity of the material, based on the measured travel time and the known material thickness.

Figure 48: Boxes for the component measurements.

The measurements on the dry materials were superimposed by reflections of the lateral surfaces of the wooden boxes, making an identification of the actual back wall reflection difficult. Measurements on wet material yielded usable results, as the moisture content decreased the emitted electromagnetic wave cone, thereby minimizing the influence of sidewall reflections. Since the measurements in sec-

tion 3.4.5 had a defined annulus thickness of 20.5 cm, the permittivity of the dry components was additionally determined on the basis of the component measurements.

All radar measurements have been carried out with antenna frequencies of 1000 and 1600 MHz by using the “SIR 4000” handheld device.

3.4.4.2 Results

The dielectric permittivity ε_r can be estimated by reformulating equation 17 as:

$$\varepsilon_r = \left(\frac{c \cdot \Delta t}{d \cdot 2} \right)^2 \tag{21}$$

where:
- ε_r ..... relative dielectric permittivity [-]
- c ..... velocity of EM wave in vacuum = $3 \cdot 10^8$ [m/s]
- Δt ..... one way travel time [s]
- d ..... layer thickness [m]

Hence, with the known layer thickness of $d = 0.2$ m, the dielectric permittivity can be back calculated. Figure 49 shows the radargram of the component measurement on saturated pea gravel. The first reflection can be identified at a two-way travel time of 5.45 ns. This results in a dielectric permittivity ε_r of 16.71.

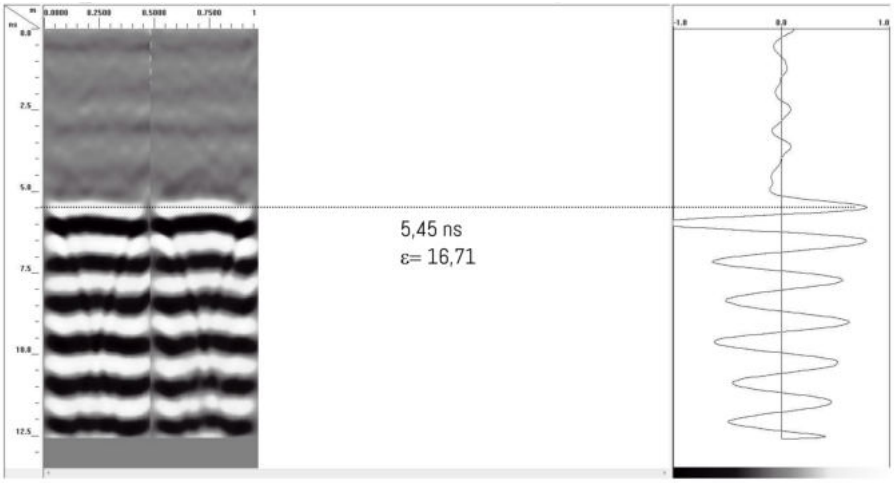

Figure 49: Radargram for the component measurement on saturated pea gravel (taken from Willmes (2018).

The results of the component measurements for the dielectric permittivity are listed in Table 4, including the results of the dry components back calculated from the tests in Section 3.4.5.

Table 4: Dielectric constants of the individual components.

Component	Two way travel time [ns]	Electromagnetic permittivity ε [-]
pea gravel, dry	2.25	2.7
pea gravel, wet	2.85	4.3
pea gravel, saturated	6.9	25.5
mortar	3.54	7.0
mortar + pea gravel	3.54	7.0
excavatet material (gneiss)	3.54	7.0

3.4.5 Measurement on the Analogue Model

In order to ascertain the possible detection of voids and to model transition scenarios of different materials and saturation conditions an analogue model was created. Hence, measurements could be carried out within a controlled setup.

3.4.5.1 Test setup

For the measurements on the analogue model, two differently reinforced lining types (reinforcement content and arrangement) were used. Figure 50 shows the design concept of the wooden formwork mounted on a lining segment of the analogue model. The segments were placed along the radial joint on wooden beams on the ground.

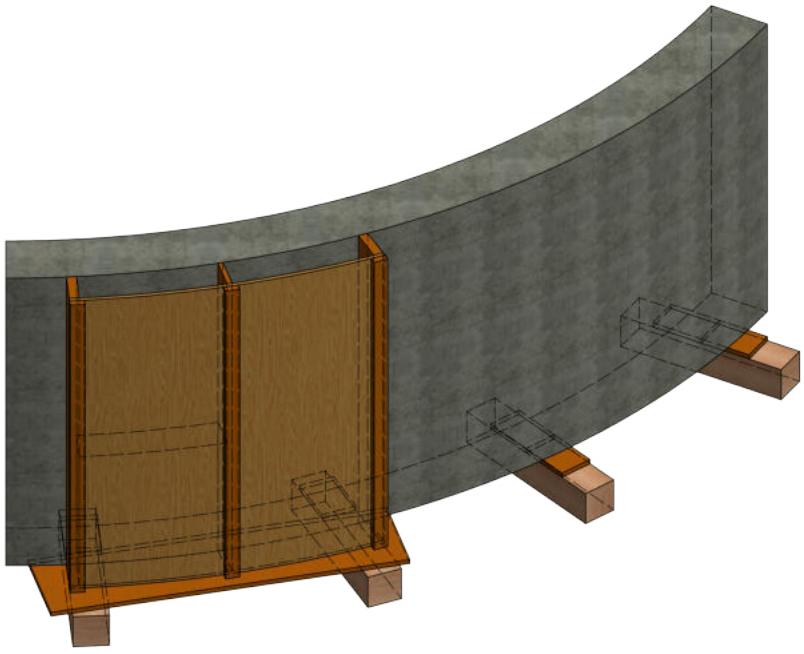

Figure 50: Scheme of the analogue model test setup.

At the back (rock side surface), wooden formworks were arranged on the lining segments, extending over the entire height of the lining, representing the annular gap between the back of the segment and the rock mass. In order to be able to clearly recognize the reflection of the formwork (rock side), an aluminium sheet was attached.

Four chambers were formed, which were filled with different materials in the course of the measurements. Figure 51 shows the formwork during the assembly. The vertical wooden board on the left and the right represent the external boundary of the tested area. The board in the middle is used for the separation between the two chambers on the left and the right side. All formwork joints are waterproof. A valve has been implemented in the bottom board in order to be able to vary the water content.

(a) Wooden formwork without "rock" side boundary.

(b) Wooden formwork with "rock" side boundary.

Figure 51: Analogue model test setup. Wooden formwork mounted on the "rock" side surface of the segments.

3.4.5.2 Measurement procedure and examined cases

In order to capture a significant number of transitions (reflections, see Figure 52) at the concrete annular gap boundary and to cover the expected possible scenarios of the in-situ backfilling situations, an extensive testing program was carried out. This includes cases of pea gravel dry, fully saturated, and with known content of air and water.

The test procedures with pea gravel were conducted on segments with low (type A) and higher (type B) reinforcement content. In addition, the scenario of excavated

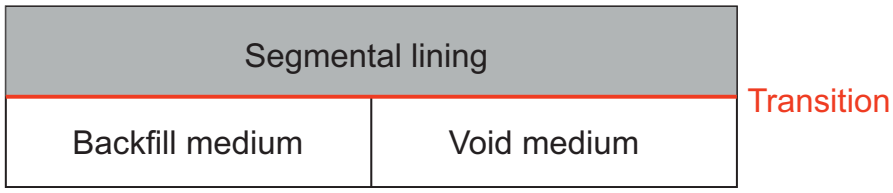

Figure 52: Schematic illustration of the transition between lining segments and annular gap.

material (gneiss) with different humidity conditions to air and water was recorded on the segment type A. The reinforcement plan, the position of the different chambers and the measurement tracks (blue arrows with numbering) for the segment type A is illustrated in Figure 53. The left wooden formwork was used for the excavated material, the right one for pea gravel. Figure 54 shows the equivalent situation for the segment type B which was solely used for pea gravel. Pea gravel or excavated material was placed in chamber 1. The reinforcement spacing for the segment type A ranges between 16.5 and 30.6 cm in vertical direction and is 29.73 cm in horizontal direction. For the segment type B it ranges between 12 and 33.4 cm vertically and between 11.8 and 23.3 cm horizontally.

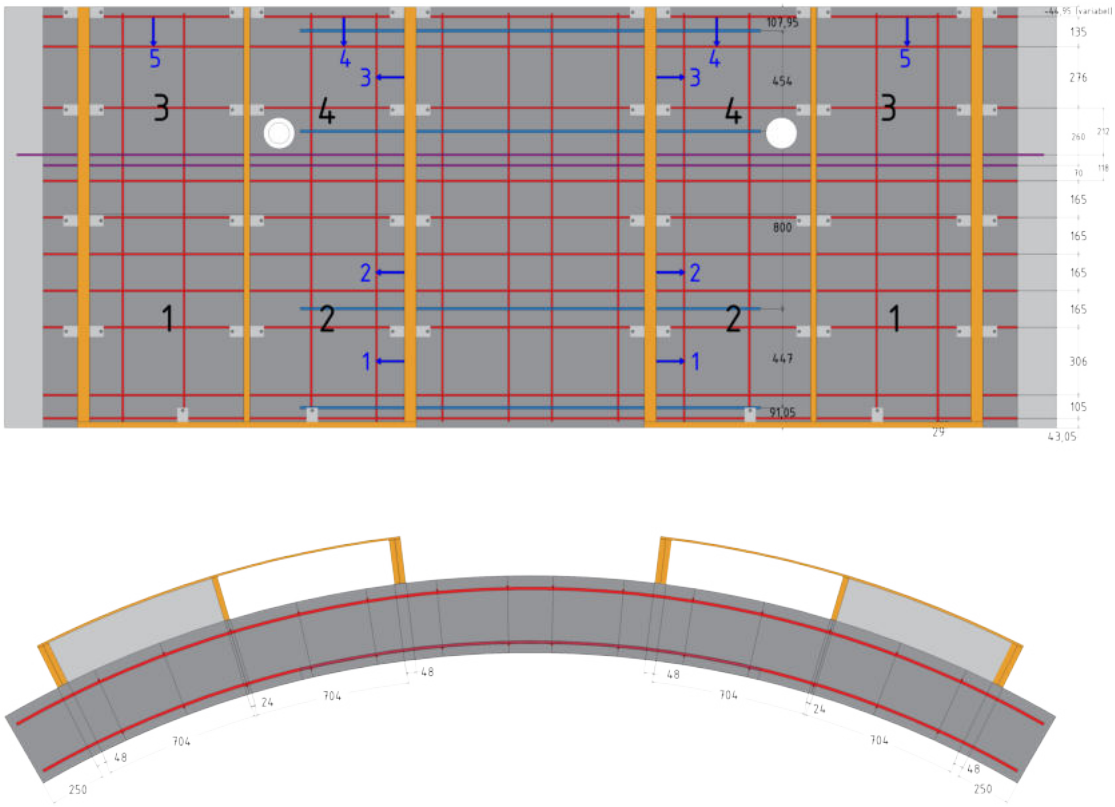

Figure 53: Reinforcement plan and measuring tracks of the segement type A with wooden formwork and chamber numbering. Top: front view towards the interior surface of the segment (formwork boundaries and metal mounting brackets illustrated on inner surface); Bottom: top view of the segment.

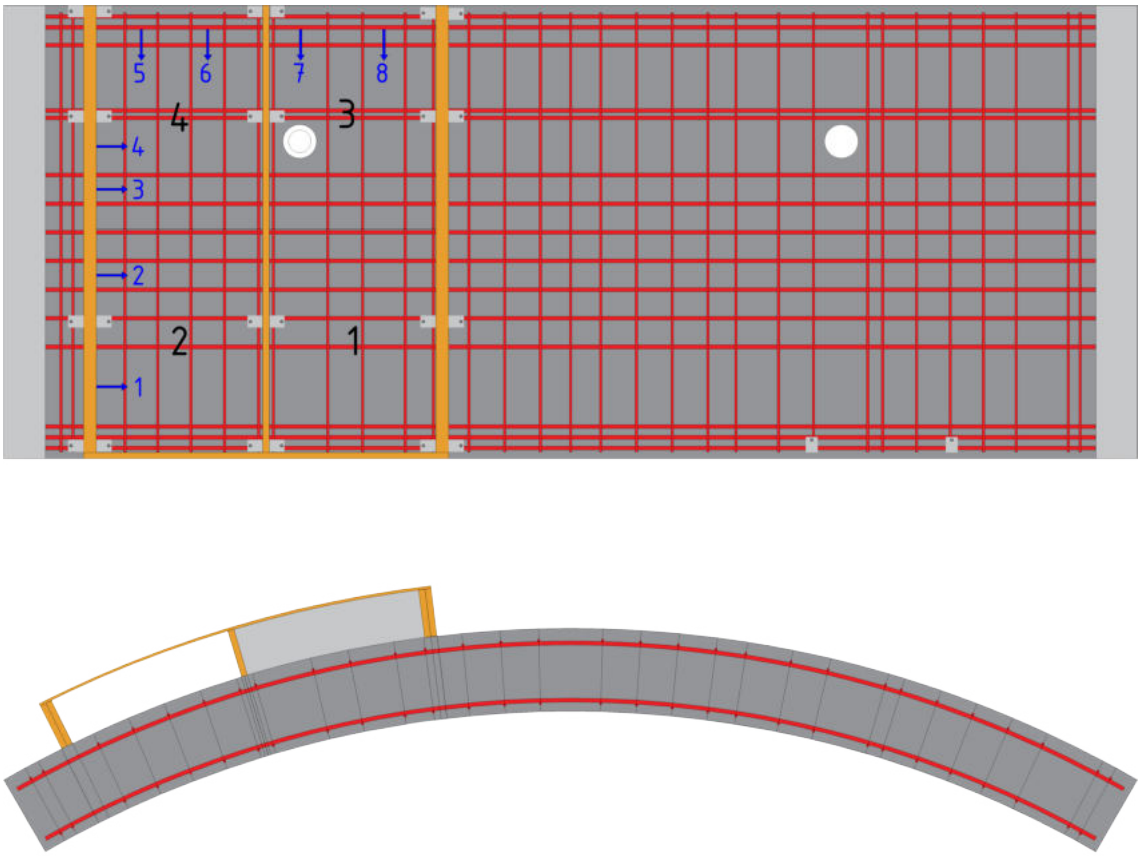

Figure 54: Reinforcement plan and measuring tracks of the strongly reinforced lining with wooden formwork and chamber numbering. Top: Front view towards the interior surface of the segment (formwork boundaries and metal mounting brackets illustrated on inner surface); Bottom: Top view of the segment.

The radar measurements were carried out with the antenna frequencies of 1000 and 1600 MHz with the “SIR 4000” handheld device and different polarizations (antenna orientation). Since the antenna dipoles are sensitive to parallel aligned metal rebar targets, the polarization can be changed by rotating the antenna by 90°.

In order to improve the measurability and to provide reliable results, the measurement tracks were chosen centrally between two reinforcement bars. Hence, the reinforcement plan has to be known and marked on the inner surface of the segments. Figure 55 depicts the segment type A with the reinforcement and measurement plan and shows the measurement procedure.

In order to illustrate the detectability of transitions with and without mortar injected pea gravel and excavated material, mortar was added to chamber 1 at all formworks for a subsequent measurement. In both cases the mortar was 9 months old. Table 5 shows the scenarios and the measurement procedure for the segment type A, table 6 for the segment type B.

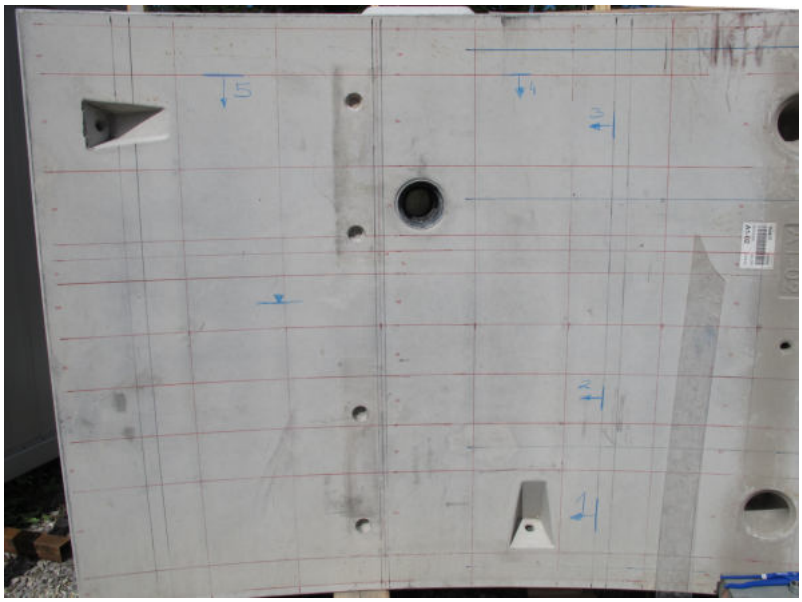

(a) Reinforcement plan (red) and measuring concept (blue) illustrated on the inner surface of the segment type A.

(b) GPR measurements with the "SIR 4000" handheld device.

Figure 55: Analogue model test setup and measuring procedure.

Table 5: GPR measurements on the segment with low reinforcement content – pea gravel / excavated material in chamber 1. Chamber 3 and 4 stay empty. Water content varies up to step 6 in chamber 1 and step 8 in chamber 2. Mortar is added in chamber 1 at stage 7.

Step	measured tracks	chamber	
1		1	2
2	1, 2, 5	dry	dry
3	1, 2, 5	saturated	dry
4	1, 2, 5	wet	dry
5	1, 2	wet	saturated
6	1, 2, 4	saturated	saturated
7	1, 2	mortar	wet
8	1, 2	mortar	wet

3.4.5.3 Results

Figure 56 shows examples of radargrams with different materials in the annular gap. The red dashed line indicates the exterior surface of the segments. A black dashed line refers to the back wall reflection of the formwork boundary (if detectable). Since the travel time depends on the material, the expected reflections lie at different positions. The illustrated two-way travel times are in good agreement with the estimated values based on equation 17.

Table 6: GPR measurements on a highly reinforced segment – pea gravel in chamber 1. Chamber 3 stays empty. Water content varies up to step 7 in chamber 1 and step 9 in chamber 2 and 4. Mortar is added in chamber 1 at stage 8.

Step	measured tracks	chamber		
1		1	2	4
2	1, 2, 7, 8	dry	dry	empty
3	1, 2, 7, 8	saturated	dry	empty
4	1, 2, 7, 8	wet	dry	empty
5	1, 2	wet	saturated	empty
6	1, 2, 5, 6	saturated	saturated	empty
7	3, 4	saturated	saturated	saturated
8	3, 4	mortar	wet	wet
9	1, 2	mortar	wet	wet

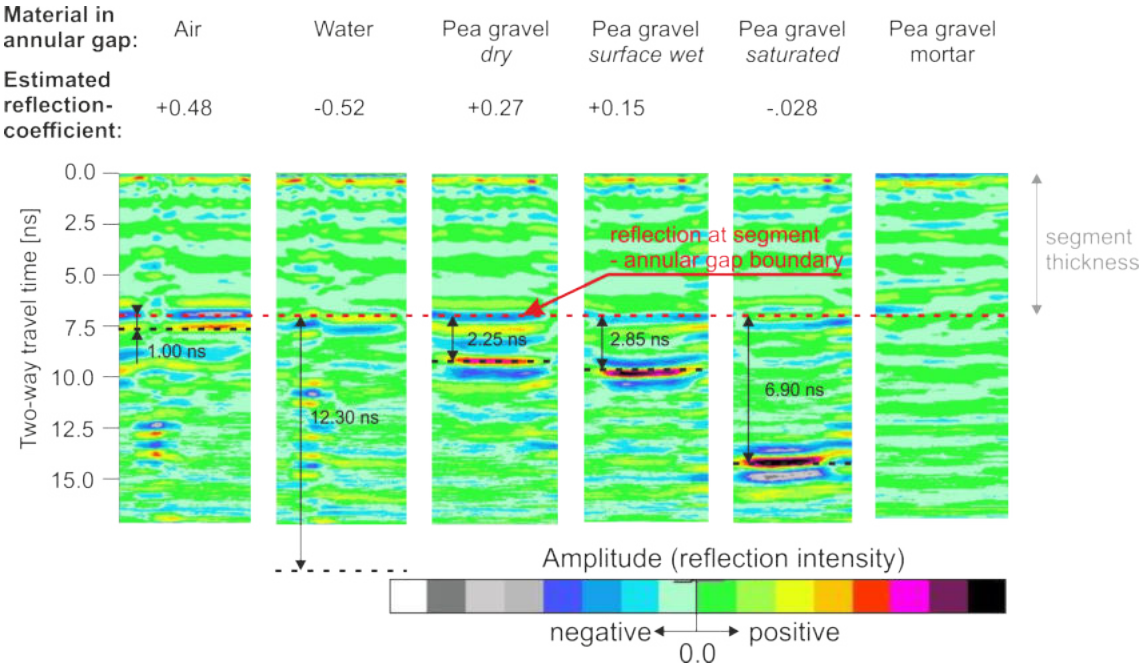

Figure 56: Radaragrams of the analogue model measurements for the weakly reinforced lining different materials (taken from Henzinger et al., 2018).

Comparing the reflection characteristics with the reflection at the concrete to air boundary, similar reflections with decreasing intensity in the transition from concrete to dry pea gravel and concrete to moist pea gravel are noticeable. At the concrete to water boundary, as well as at the concrete to the water-saturated pea gravel boundary, a phase change can be detected. In addition, the transition from concrete to water-saturated pea gravel shows a significantly lower intensity. The concrete to mortar boundary shows naturally no significant reflection. When filling the formwork with dry, moist and water-saturated pea gravel, a significant reflec-

tion of the aluminium sheet on the formwork is also recognizable which enables material identification based on the travel times.

When the excavated material (gneiss) is present in the annular gap, a material identification can be done by analysing the reflection characteristic at the back of the lining segments. The comparison with the reflection characteristic at the interface between concrete and air is helpful. Probably due to the coarseness of the excavated material (grain sizes up to 100 mm) and the associated strong scattering of the radar signal, the measurements on the analogue model with excavated material showed no reflection of the aluminium sheet on the formwork.

For the determination of the media within the annular gap, the application of GPR measurements has proven successful. It turns out that both the travel time as well as the reflection characteristic and intensity are useful tools for the identification of the material within the annular gap.

3.4.6 In-situ measurement

With the findings of the numerical and on-site tests, underground measurements were performed on partially backfilled segments. The measurements were carried out in the south tube of construction lot KAT2 in the Koralm tunnel on the segments type B. Due to the successful application on the analogue model, the “SIR 4000” handheld device was used. Since the measurements with the 1600 MHz antenna frequency yielded significantly more meaningful results than with the 1000 MHz antenna, only the 1600 MHz antenna was used for the underground measurements.

3.4.6.1 Boundary conditions

In order to be able to measure the transition between backfilled and non-backfilled segments the area behind the shield tail was chosen for the tests. Since the redistribution of pea gravel forms a distinct slope, the transition between pea gravel and air filled voids can be visually detected at each side wall. The rock mass, within the test area is composed of intermediate jointed and unweathered coarse grained gneiss with quartzite intrusions. Rock breakouts were identified along the excavation boundary with an uneven distribution. Minor water intrusions led to a moistening of the pea gravel and the segmental lining. Hence, pea gravel and rock breakouts of different block sizes are heterogeneously mixed and wet. In addition, the pea gravel was partially grouted.

3.4.6.2 Measurement procedure

By visual inspection of the pea gravel injection openings the surface of the pea gravel mortar mixture in the annular gap was roughly estimated (see Figure 57). Accordingly, the areas were defined where radar measurements should be per-

formed.

Figure 57: Image of the pea gravel slope within the annular gap behind the shield tail. View against the advance direction (taken from Henzinger et al., 2018).

The type B segmental ring provides three measuring tracks in circumferential direction for the GPR measurements. These three measuring paths had a sufficient distance between the circumferential reinforcement bars ($\geq$ 24 cm) and therefore reliable results were obtained on the analogue model. At first a rough reinforcement location detection using the reinforcement plan and the GPR device was carried out on the segments in order to be able to determine the exact positioning of the radar measurements. Subsequently, the radar measurements were carried out on defined measuring tracks (see Figure 58).

3.4.6.3 Results

The transition from the pea gravel mortar mixture to the unfilled annular gap could be successfully detected by the radar measurements. Figure 59 shows a schematic representation of the pea gravel distribution in the annular gap behind the tail of the shield (green, solid and dashed).

The radargrams obtained in this area are shown in Figure 60 in which the transition from the pea gravel mortar mixture to the not yet filled annular gap is marked. On top of the radargrams the numbers of the individual measuring paths (10, 12 and 18) are given corresponding to the measurement path in Figure 59. The lateral spacing of the reinforcement was 27.4 cm for track 10, 33.4 cm for track 12 and 24.0 cm for track 18. The red arrow represents the measurement path on the lining

Figure 58: GPR measurements for the void detection in the annular gap at the south tube of the Koralm tunnel construction lot KAT2.

segments. On the horizontal axis, the two-way travel time is given. In all three radargrams, the reflection of the rear side of the lining segments can be seen with a two-way travel time of 6.5 to 7.0 ns. This feature is very pronounced in the area of the empty (air-filled) annular gap and decreases at the transition to the pea gravel or pea gravel – mortar mixture filled annular gap. These transitions were marked on the concrete surfaces of the lining segments and the plausible surface of the pea gravel is shown in Figure 59. The horizontal black line in Figure 60 indicates the transition between backfilled annular gap and void. By connecting the transition between the pea gravel – mortar mixture and the air filled void of all three measurements, a repose angle of 31.5° is obtained.

The measurements shown in Figure 60 were executed on a lining segment with a concrete age of around 15 months. Measurements on segments, which were only around six weeks old, showed strong attenuation of the radar signal due to their high moisture content and associated electrical conductivity, which made it impossible to evaluate the reflection characteristic of the rear side of the lining segment.

3.4.7 Results

Due to the numerical simulations, it could be assumed that the void detection using GPR is very likely to be successful. The simulations have shown, that the antenna frequencies of 1000 and 1600 MHz are appropriate.

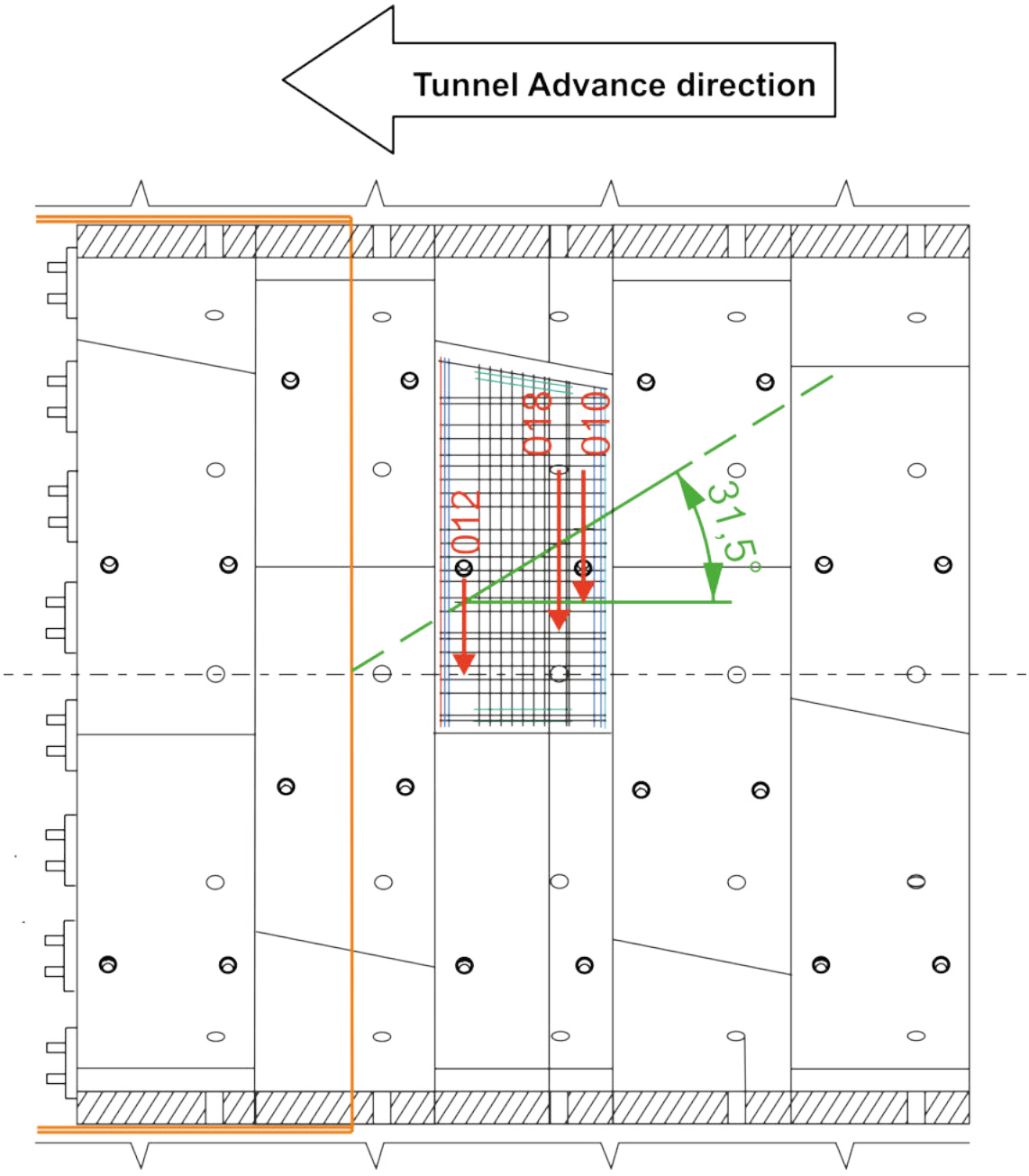

Figure 59: Schematic view of the measuring paths (red), the slope angle (green) and the shield tail (orange) in the longitudinal section of the segmental lining (taken from Henzinger et al., 2018).

The material characterization based on radar measurements on small-sized wooden boxes was only possible to a limited extent due to excessive boundary influences. However, since the radar measurements on the analogue model were carried out under defined boundary conditions and a clearly defined annulus, the measurements allowed material characterization. The measurements on the analogue model also allowed a differentiation of the material within the annular gap based on the two-way travel time and the reflection characteristic on the rock side of the segment.

Although the underground measurements were executed on the lining segments

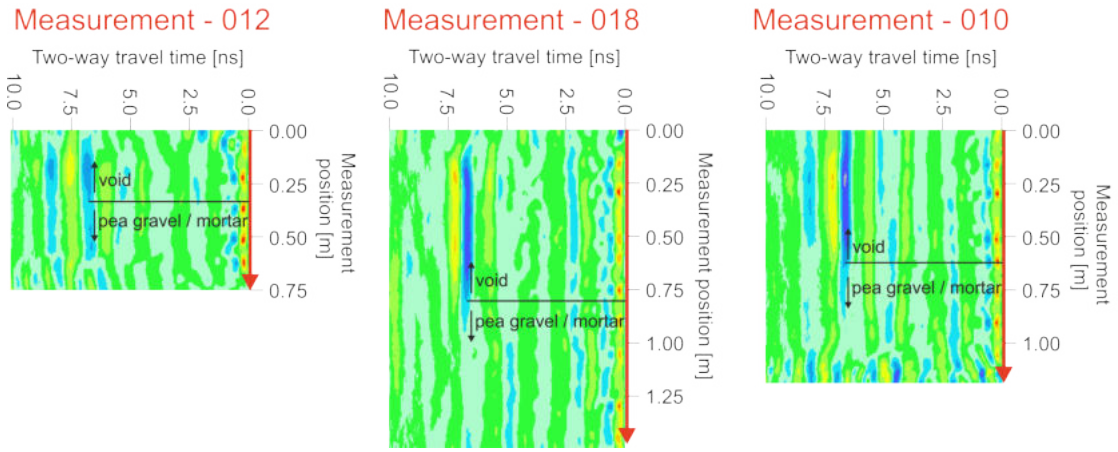

Figure 60: Results obtained by the GPR measurements at the respective positions (taken from Henzinger et al., 2018).

type B, a clear differentiation between the not yet filled annular gap with the back-filled gap was possible.

The limiting factors are the small distances between the reinforcement and the moisture content of the lining concrete. While the measurements on approximately 15 months old segments delivered very clear reflections at the exterior surface of the segments, the approximately six weeks old segment showed a high conductivity due to the higher moisture content. Hence, the reflections on the segment – annular gap boundary could not be differentiated.

3.5 Outlook and recommendations

The presented methods for the investigation of the deformation properties of pea gravel allow a novel determination of the distribution and elastic response in the annular gap. These can be carried out with only little on-site effort.

With the use of model scale test setups, the relocation behaviour of a closely graded material within a planar and circular gap could be analysed. It has been shown, that the regripping process causes a distinct relocation behaviour within the annular gap. Hence, the segments behind the shield tail have to be separated into partially and fully bedded parts.

The large oedometer tests have shown that the deformation properties of pea gravel strongly depend on the loading type and the corresponding load level. In primary loading stages Young's moduli of approximately 80 MPa can be achieved at a load level of 0.3 – 0.4 MPa. At the same load level reloading cycles yield Young's moduli of approximately 200 – 220 MPa while unloading cycles yield Young's moduli of up to 300 – 420 MPa.

The in-situ tests provided consistent and plausible results. The tests were carried

out via the backfilling opening of the segmental lining. The dependence of the loading type on the deformability could be confirmed. Due to the low load dependency of the primary loading and reloading stages, these results have to be treated with caution.

The ground penetrating radar measurements on both the analogue model and in the tunnel yielded positive results for the detection of voids (absence of pea gravel) in the annular gap. An antenna frequency of 1600 MHz has been found to be most suitable under the given boundary conditions. The age or the associated moisture content of the concrete of the segmental lining has a major influence on the informative value of the radar measurements. High moisture content leads to a strong damping of the radar waves and makes the measurement results unreliable. The knowledge of the reinforcement allocation is required in advance. With a lateral reinforcement distance of 240 mm and a transverse reinforcement with a distance of approximately 159 mm, the measurement could be carried out successfully.

4 Deformation characterisation of the segmental lining

The deformation of the segmental lining ring after leaving the protection of the TBM shield is a common and unavoidable effect. Due to the closed geometry, the ring starts to ovalize (Guideline Concrete Segmental Lining System, 2011). Hence, tolerances regarding angular distortion of the joints and the ring width have to be provided in order to avoid clearance violations. The ovalization is mainly triggered by the dead weight of the segments and the number of longitudinal joints per ring. After leaving the shield tail, the bedding should limit further ovalization. The ovalization usually takes place within the area of ten rings behind the shield tail (Recommendations for the design, production and installation of segmental rings, 2013).

4.1 Measurement of the lining displacement

Displacement measurements of the lining are usually performed by mounting approximately five Bi-reflex targets on a single ring of lining segments before leaving the TBM Shield. The target positions are primarily influenced by the geometry of the TBM. Hence, crown and side wall positions are preferably chosen. As usually applied in conventional tunnelling the measurement sections are situated every 10 to 30 m (Austrian Society for Geomechanics, 2014). The measurements are usually executed on a daily basis during the maintenance shift. The zero measurement is done while the ring is still within the TBM shield.

Figure 61a shows the horizontal and vertical displacement profile of a given measurement section. The vertical displacements in combination with the longitudinal displacements are illustrated in Figure 61b. Both plots depict the magnified displacement development for each measurement time.

In order to evaluate the displacements in relation to the tunnel advance, the development for each direction has to be plotted versus time or the relative advance. Figures 62, 63 and 64 illustrate the displacement components depending on the relative advance to the first measurement.

After passing the shield tail, a typical rigid body motion of the ring in the vertical direction with a maximum displacement of about 0.17 cm can be observed. Further displacements, primarily in vertical direction occur while passing the crusher, which is located about 13 to 20 m behind the cutter head. The area of influence is indicated by dashed lines. However, a clear allocation of the displacements to the influences of the crusher is not possible. It can be seen that hardly any addi-

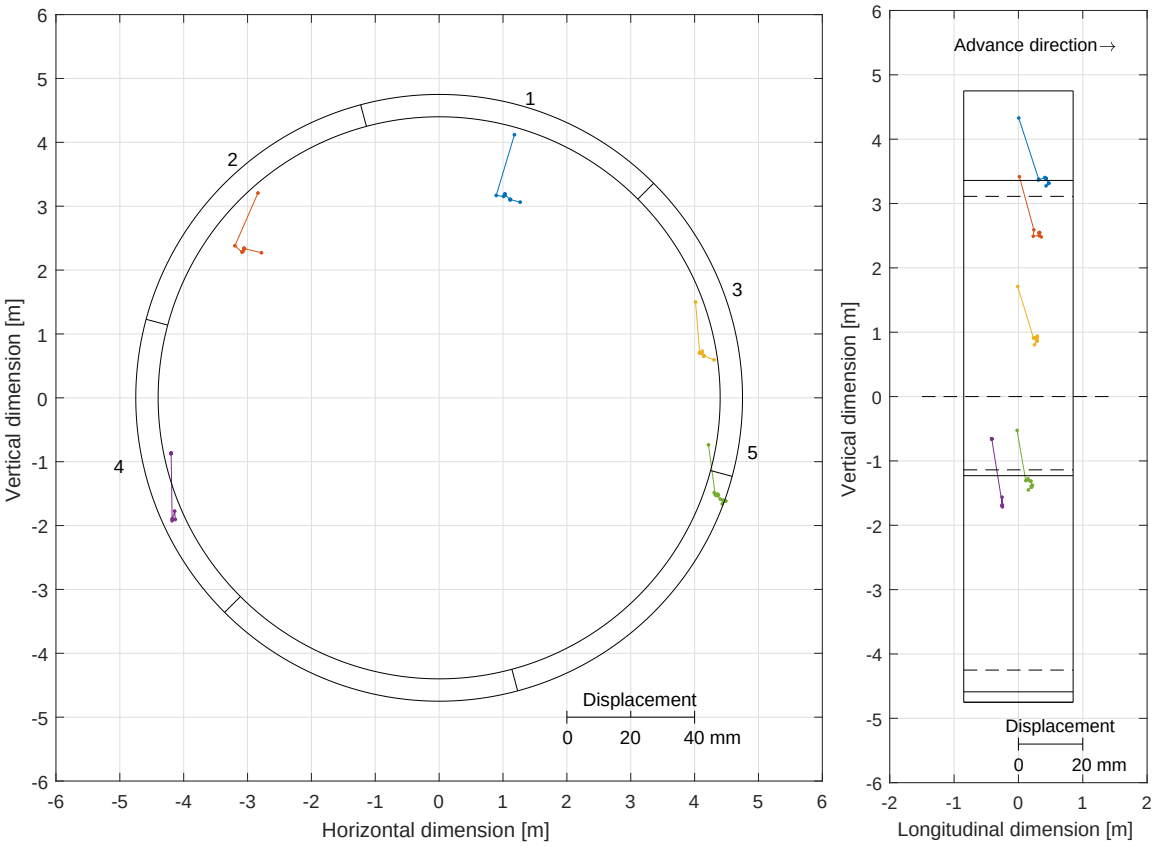

(a) Cross section. (b) Longitudinal profile.

Figure 61: Magnified deformations of the segmental lining with five Bi-reflex Targets.

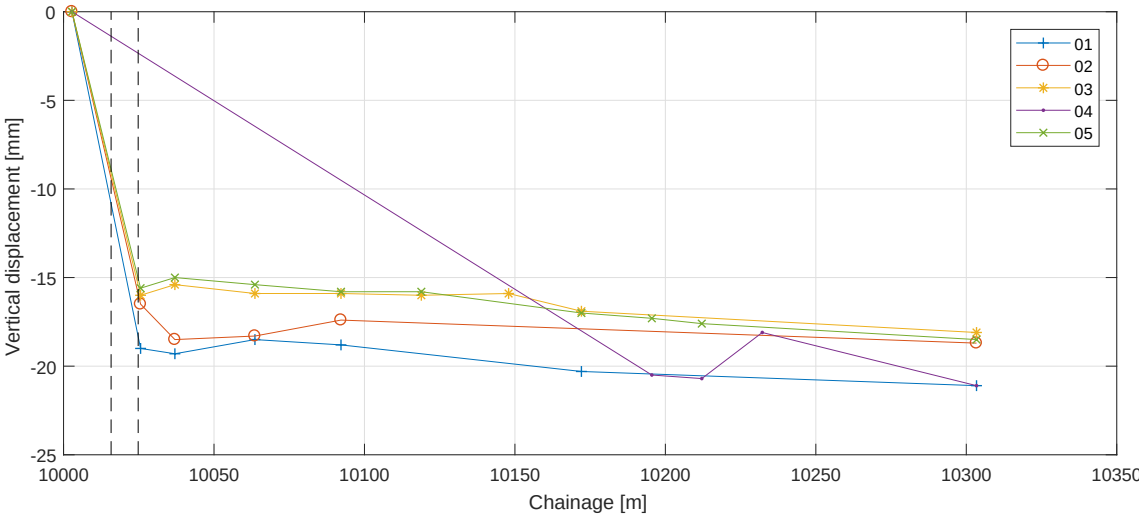

Figure 62: Vertical displacement ("+" . . . heave, "-". . . settlement; dashed lines indicate the area of the crusher).

tional displacements, occur after the third measurement. The mentioned order of magnitude is generally to be regarded as normal.

The horizontal displacements show a small, but uniform shift to the left, when

looking in advance direction. This can be explained by the jack position and current course correction.

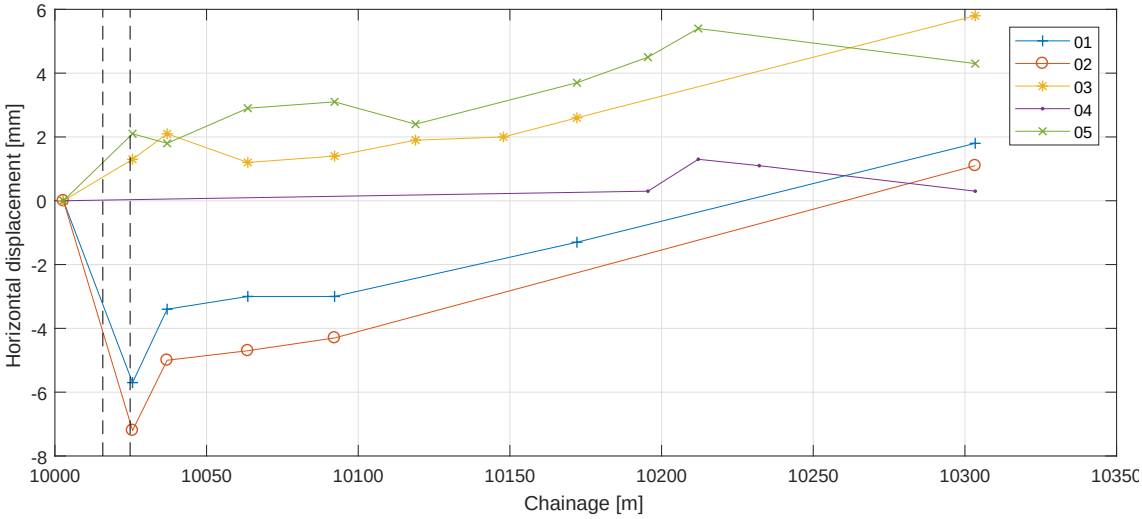

Figure 63: Horizontal displacement (viewing direction towards tunnel face; "+" . . . displacement to the right, "-". . . displacement to the left; dashed lines indicate the area of the crusher)

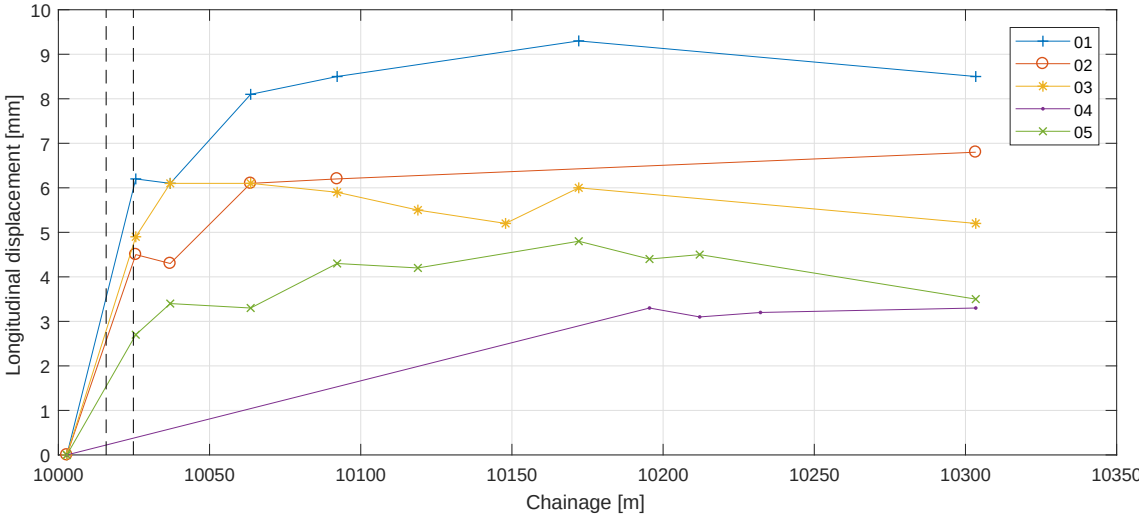

Figure 64: Longitudinal displacement ("+" . . . displacement in advance direction, "-". . . displacement against advance direction; dashed lines indicate the area of the crusher)

The measurements imply a rigid-body motion. Nevertheless, the actual ovalization cannot be identified. Hence, in the following section a data processing methodology is introduced.

4.2 Data processing

To be able to assess the ovalization degree based on the displacement measurements, the eccentricity is used to describe the deviation of an ellipse from a circle.

The main feature of an ellipse differentiating it from a circle is the existence of the focal points. With a circle, both focal points coincide at the center. The distance between the focal points and the center of an ellipse is termed as linear eccentricity e. Figure 65 shows an idealized ovalization of the segmental lining. In the illustrated case the horizontal half axis a is longer than the vertical half axis b.

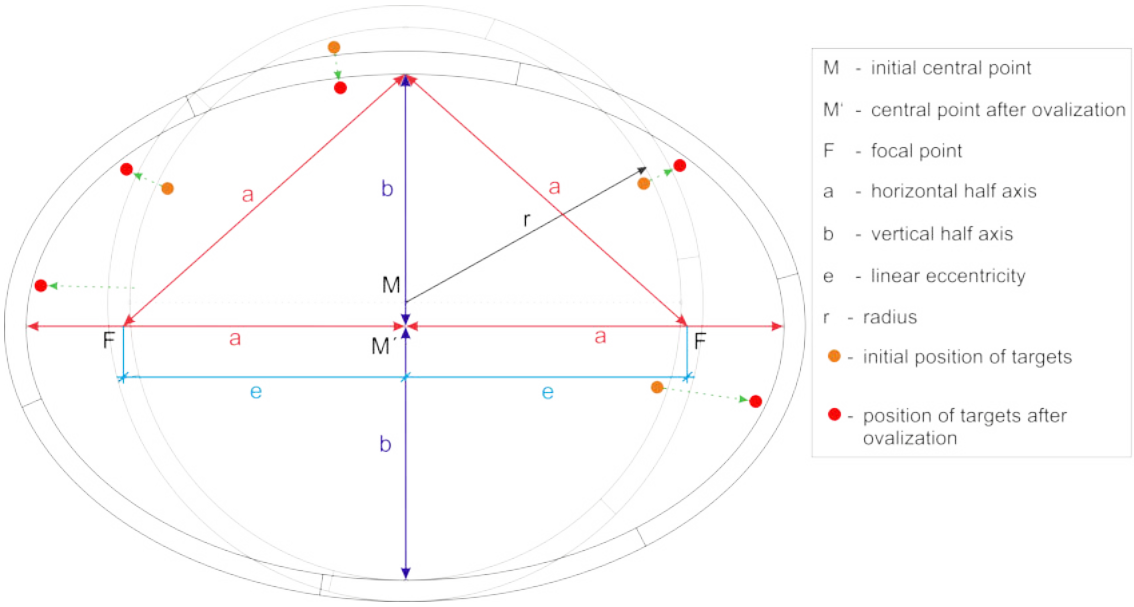

Figure 65: Idelized ovalization of the segmental lining (taken from Henzinger et al., 2018).

The linear eccentricity can be defined as:

$$e = \sqrt{a^2 - b^2} \tag{22}$$

where: e ..... linear eccentricity [m]
a ..... horizontal half axis [m]
b ..... vertical half axis [m]

Dividing the linear eccentricity e by the horizontal half-axis length a, the dimensionless numerical eccentricity ε is obtained:

$$\varepsilon = \frac{e}{a} \tag{23}$$

where: ε ..... numerical eccentricity [-]

For an ellipse, the numerical eccentricity is between zero and one, where zero is a circle and one a parabola. In order to obtain the respective half-axis lengths, an ellipse has to be fitted into the displacement measurements for each subsequent measurement. This is also necessary because the measurement positions are different at the respective rings. In order to obtain a plausible ellipse geometry, the deformation figure was interpolated at a minimum number of four (five points are necessary to describe an ellipse; if the center is known, the number drops to three) simultaneously recorded geodetic individual measurement points.

For the presented measurement profile in section 4.1, the development of the vertical half axis b, the horizontal half axis a and numerical eccentricity is illustrated in Figure 66. Figures 66a and 66b show the development of both half axes in relation to the relative advance of the cutterhead since the zero measurement. Figure 66c illustrates the development of the numerical eccentricity ε as defined in Equation23. The development shows a shortening of the vertical half axis while the horizontal half axis increases. Hence, the numerical eccentricity becomes positive. For this case the numerical eccentricity reaches 0.1 at a relative advance of 20 m to the initial measurement.

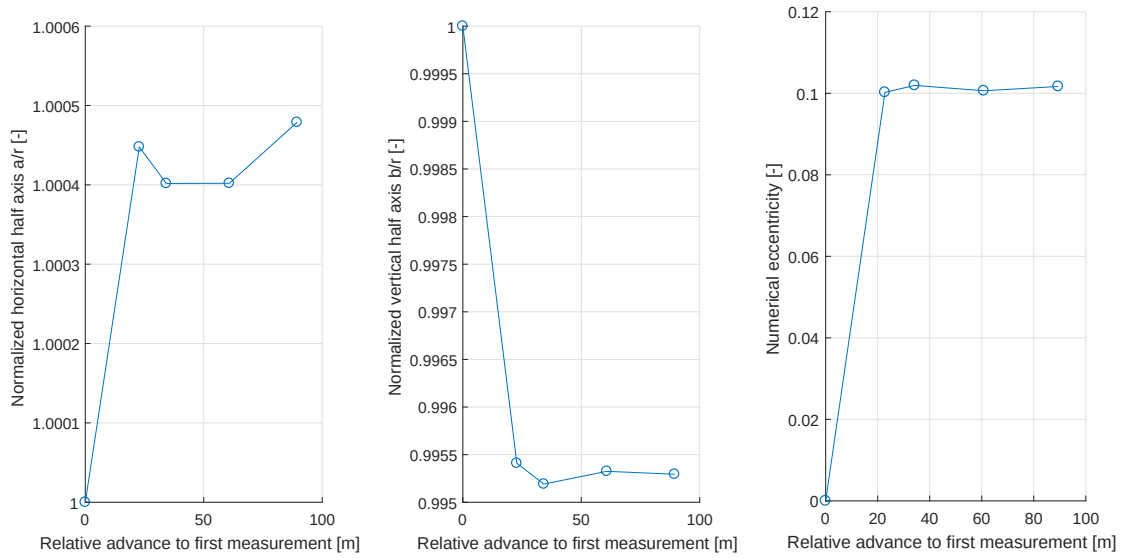

(a) Development of the normalized horizontal half axis a/r.

(b) Development of the normalized vertical half axis b/r.

(c) Development of the numerical eccentricity.

Figure 66: Processed deformation data from Section 4.1. Development in relation to the face advance.

4.3 Analysis of the characteristic ovalization behaviour

To illustrate the influence of different boundary conditions on the deformation behaviour, numerous measurement sections from the Koralm tunnel have been eval-

uated with respect to their ovalization characteristic. For the comparison, the numerical eccentricity of the partially bedded rings in the range of 0 to 20 m after the first monitoring time has been subject to a linear regression in order to represent the usual deformation characteristic, without any bedding improvement measures.

The coefficient of determination R^2 is used to describe the quality of the fit of the regression. R^2 is a statistical value which provides a value of how well the observed data is represented by the model (in this case the linear regression). In its basic form it ranges from zero to one, wherein one denotes perfect fit (all data points are described by the model) and zero denotes that the data do not fit to the model (see Figure 67).

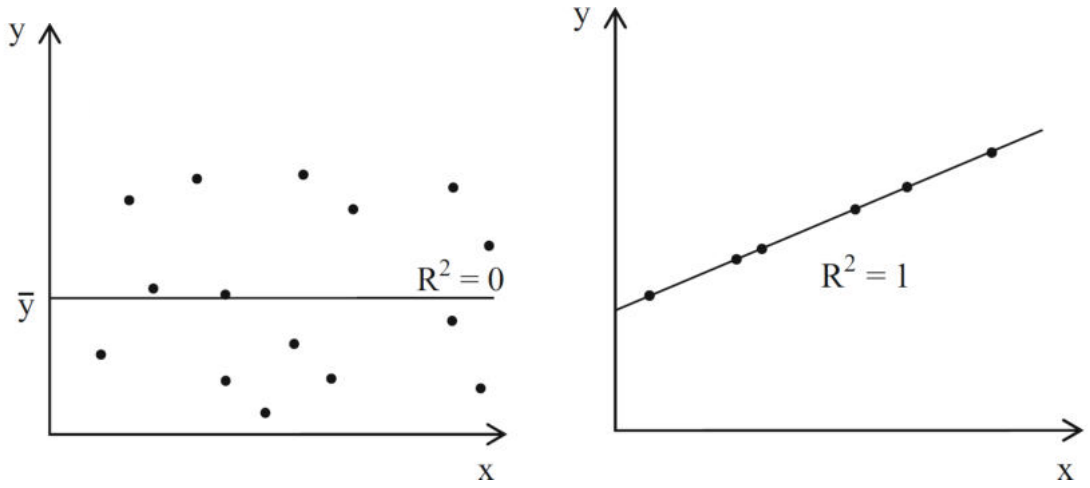

(a) $R^2 = 0$. (b) $R^2 = 1$.

Figure 67: Range for the coefficient of determination R^2 (taken from Bonart & Bär, 2018).

Figure 68 depicts the linear regression for the numerical eccentricity for a rock mass type with a predominant bedding discontinuity spacing >200 cm and a UCS >150 MPa. Twelve measurement sections have been evaluated resulting in a gradient of 0.006 and coefficient of determination R^2 of 0.81.

Table 7 shows the gradients of the deformations as a function of the bedding spacing and the uniaxial compressive strength of the rock mass. In addition to the gradient, the coefficient of determination R^2 must also be taken into account. It can be clearly seen that in the case of better rock mass conditions, the gradient is positive and the coefficient of determination does not fall below a certain threshold value in the order of approximately 0.5. For UCS below 100 MPa, negative eccentricities can be identified, which indicate a shortening of the horizontal and an extension of the vertical half-axis. It is to be expected that outbreaks from the surrounding rock mass, located in the side wall area, hinder the side wall segments from moving outwards.

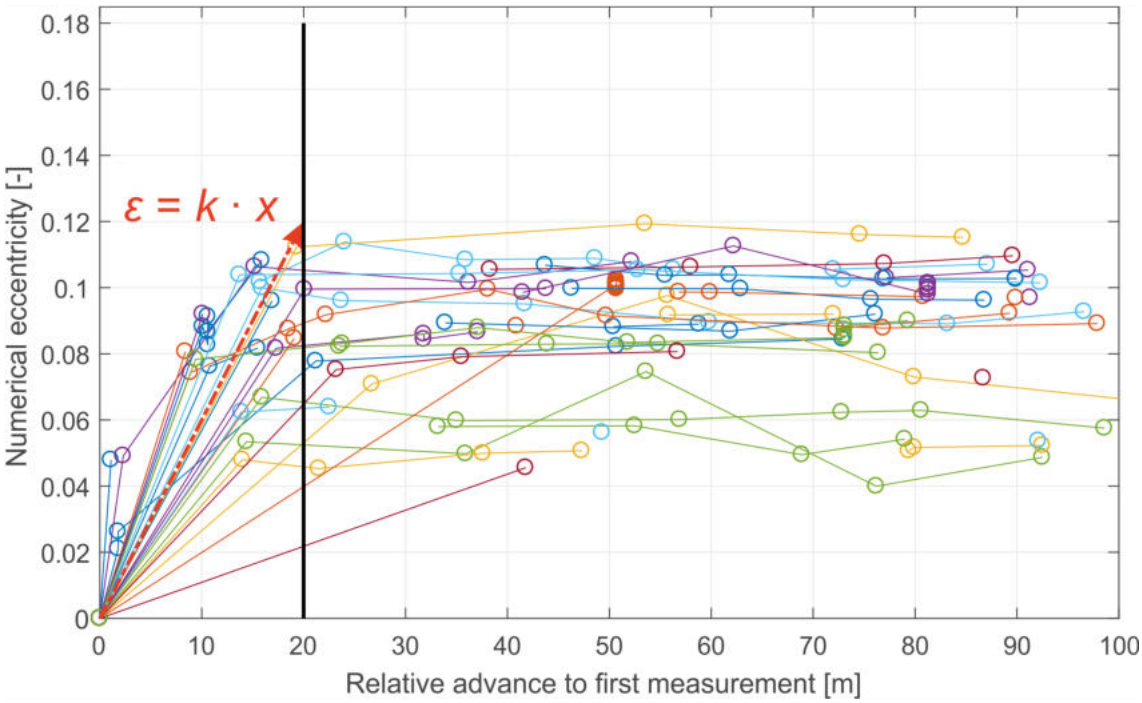

Figure 68: Development of the numerical eccentricity ε for joint spacing >200 cm and UCS >150 MPa. k represents the gradient for the numerical eccentricity.

Table 7: Gradient and coefficient of determination (R^2 with n cases) of the numerical eccentricity ε for different rock masses.

Bedding spacing [cm]	UCS [MPa]	Gradient [-]	R^2 [-]	quantity [-]
>200	>150	0.0060	0.81	27
200 – 60	>150	0.0049	0.61	15
60 – 20	>150	0.0055	0.76	12
>200	150 – 100	0.0041	0.65	4
200 – 60	150 – 100	0.0065	0.51	7
60 – 20	150 – 100	0.0042	0.47	10
20 – 6	150 – 100	0.0091	0.49	1
200 – 60	100 – 50	-0.0031	0.13	10
60 – 20	100 – 50	-0.0068	0.07	9
20 – 6	100 – 50	-0.0092	0.00	8
cataclastic	<5	-0.0043	0.00	8

5 Design improvements

Due to the insufficient bedding of the segmental lining behind the shield tail, a relatively high amount of reinforcement for a temporary load case is necessary. Rock breakouts resting on the lining may lead to further bedding deficiencies by blocking the injection openings of pea gravel. To establish an immediate contact between segmental lining and excavation boundary after leaving the shield tail, two novel bedding concepts were developed. The proposed systems avoid the critical construction stage of an unbedded and freestanding ring of segments (Henzinger et al., 2016, 2017).

5.1 Geotextile Tubes

Folded geotextile tubes (Bullflex®) are attached to the exterior surface of the segments in a notch, in order to allow for a damage free passage at the shield tail seal. After leaving the shield, the tubes can be injected with a suitable material (for example: mortar) and thereby expanded. Thus, an immediate contact with the excavation surface is established and the ovalization of the segmental ring due to dead weight and external loads is prevented. Furthermore, the rearrangement process within the annular gap is prevented, which otherwise occurs due to the forward movement of the shield (see Figure 69). Rock mass deformations can be absorbed similar to the “Convergence-Compatible Segmental Lining System” (Vigl, 2003).

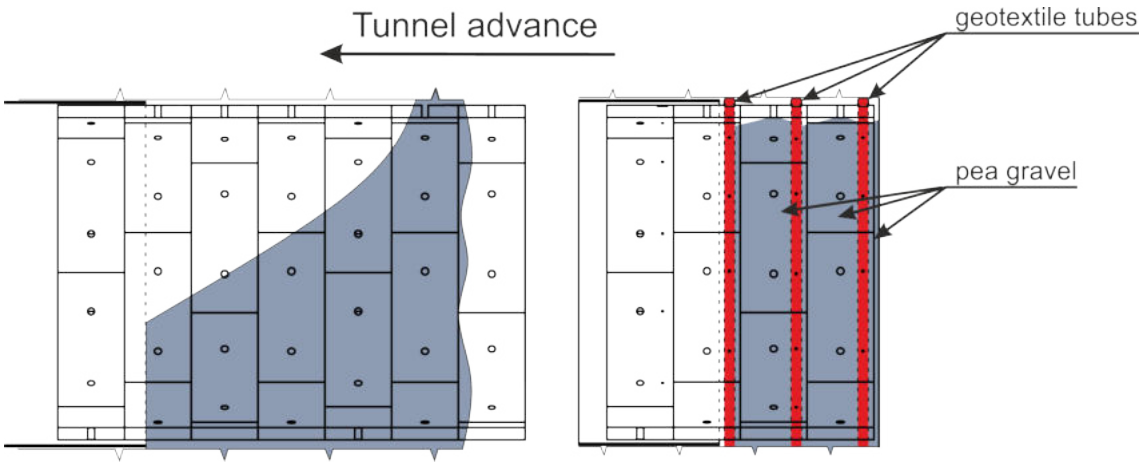

Figure 69: Distribution of pea gravel within the annular gap after advance of the TBM shield; left: without design improvements, right: with geotextile tubes.

Figure 70 shows a filling process in the annular gap, simulated using the cavity between two lining segments. Due to a special arranged seam system, the distribution of the injected material is relatively even during the inflation process.

Figure 70: Filling process of a Bullflex® geotextile tube between two lining segments; left: state before inflation, middle: geotextile tube during the inflation process, right: fully inflated geotextile tube (taken from Henzinger et al., 2016).

5.1.1 Installation preparation

For the verification of the bedding effect, a ring of segments in the northern tube of the Koralm Tunnel construction lot KAT2 was equipped and installed with geotextile tubes under stable rock mass conditions.

To guarantee the temporary and immediate bedding of the segmental lining, the geotextile tubes were attached within a notch on the exterior surface of the individual segments in order to allow safe passage of the shield tail (see Figure 71) . Due to the geometry of the vacuum erectors for the installation of the segments, two geotextile tubes per segment were necessary.

Figure 71: Notch for the geotextile tube on the exterior surface of one segment (taken from Henzinger et al., 2018).

For the injection process, additional openings were arranged in the segments at the level of the backfill injection openings (see Figure 72).

Figure 73 shows the arrangement of the individual tube segments and the injection sequence on the assembled ring of segments.

Figure 72: Additional opening for the injection of the geotextile tubes next to the pea gravel openings (taken from Henzinger et al., 2018).

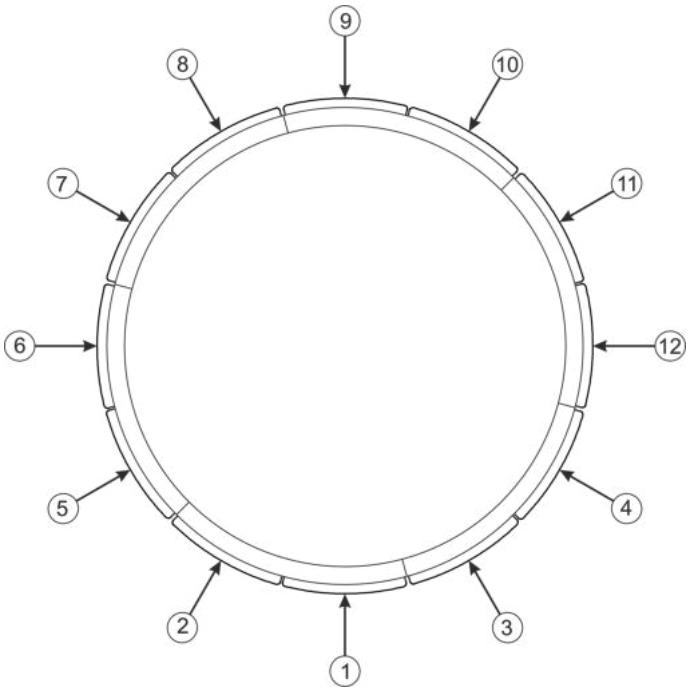

Figure 73: Positioning and injection sequence of the getextile tubes of the segmental lining (view towards the tunnel face, taken from Henzinger et al., 2018).

5.1.2 Inflation of the geotextile tubes

After leaving the shield tail, the geotextile tubes were injected with mortar. Due to the high permeability of the fabric, the excess water filters out. This leads to a quick stiffening of the filling material and thus to an early load capacity of the lining.

The overall injection process of the geotextile tubes was successful. Only with tube 4 and 5 an immediate pressure increase was detected, since pea gravel had already been located between the geotextile tube and the excavation boundary due to rearrangement.

Figure 74 depicts the geotextile tube inserted in the slot on the exterior surface prior to the injection process. After the injection process, the geotextile tube is entirely in contact with the excavation boundary (see Figure 75).

To inject the geotextile hoses, a mixture for cavity filling (Tiwofill) with a water/cement ratio of 0.6 was used. In the course of these test series, the average filling time was approximately 10 minutes with a filling quantity of around 200 l per tube.

Figure 74: Geotextile tube embedded into the lining segment prior to the injection (taken from Henzinger et al., 2018).

Figure 75: Geotextile tube after the injection with full contact to the excavation boundary (taken from Henzinger et al., 2018).

5.1.3 Geological and geotechnical boundary conditions

In the vicinity of the ring of segments, a slightly disintegrated coarse grain gneiss with subordinate pegmatoid lenses was found to be present. The foliation strikes almost perpendicular to the tunnel axis. The dip angle was documented with around 45° against the TBM advance direction. The foliation is rarely mechanically effective.

In the left crown, a water ingress of 0.2 to 0.3 l/s was present which led to an increased pea gravel redistribution in the annular gap.

The geotechnical evaluation of the TBM data reveals stable rock conditions. At a constant mean thrust of 21,000 to 22,000 kN, an equally constant torque of 3,000 to 4,000 kNm is achieved. The penetration is on average 5 mm per revolution. With the TBM performance prediction model by Gehring (1995), the uniaxial compressive strength can be backcalculated to be between 150 and 200 MPa, which is within the expected range of the encountered rock conditions.

5.1.4 Evaluation of the displacement measurements

18 Bireflex-targets have been placed in two measuring sections for the embedded segmental ring. Hence, two measurement sections located at Chainage 15577 and 15579 are situated on one ring.

Figure 76 depicts the progress of the TBM of the northern TBM between 1st of

October and 1st of November 2016. On October 1st the embedded lining ring was approximately 13 m on November 1st approximately 372 m behind the cutterhead.

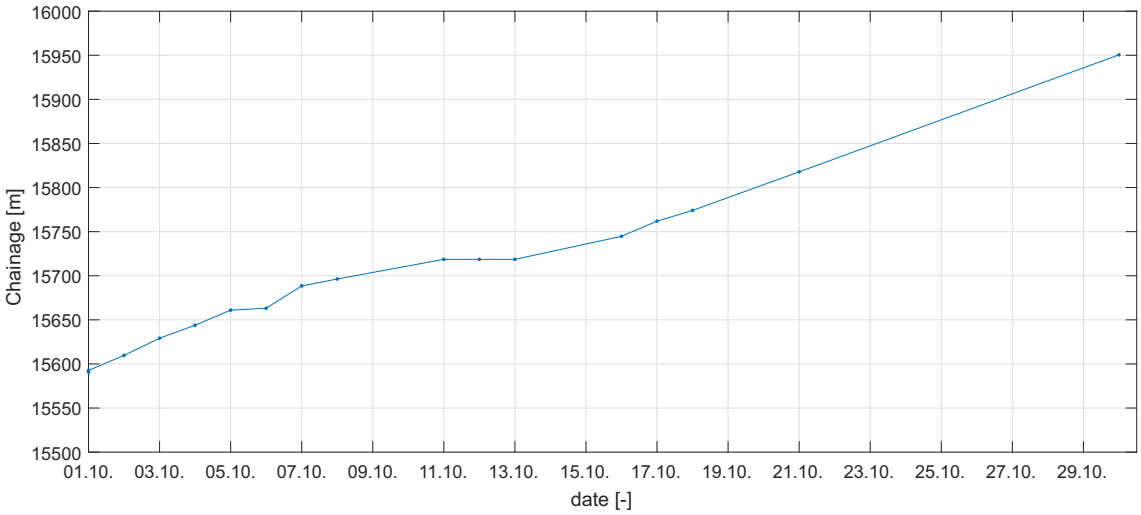

Figure 76: TBM advance from October 1st to November 1st 2016

Figure 77, 78 and 79 illustrate the development of the vertical, horizontal and longitudinal displacement in relation to the relative advance of the cutterhead. In the third follow-up measurement, the bedded segmental ring was already behind the influence area of the crusher. The vertical displacements had stopped, and showed a nearly constant value during the remaining measuring period.

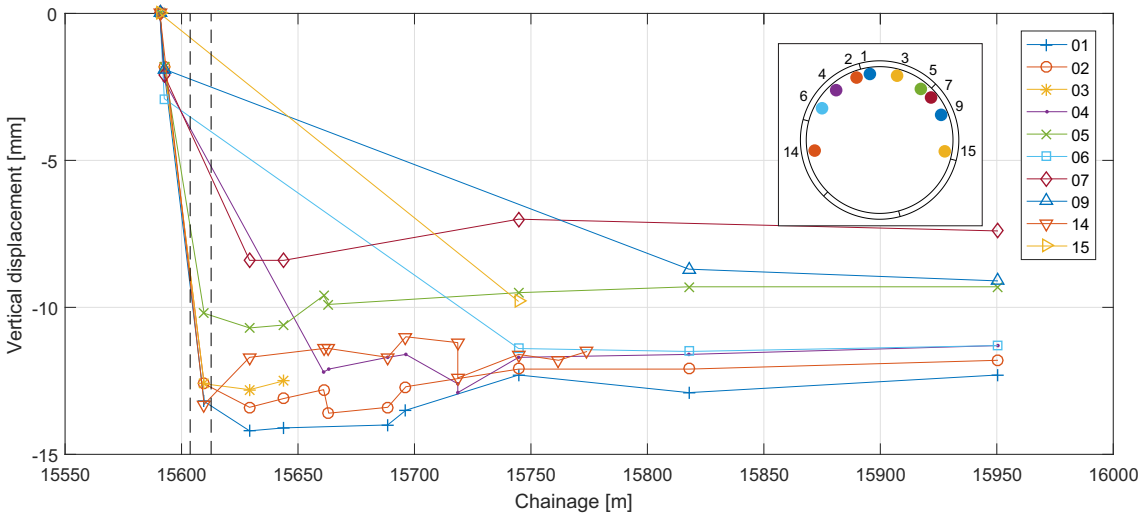

Figure 77: Vertical displacements of MS15577 (“+” . . . heave, “-”. . . settlement; dashed lines indicate the area of the crusher).

The horizontal displacements show a slight, but uniform shift to the left, facing the tunnel face. This can be explained by the position of the thrust cylinders and the current course correction.

Figure 80a shows horizontal and vertical displacements of measuring section 15577. As can be seen in Figure 77 and 78, there is an immediate settlement with a simul-

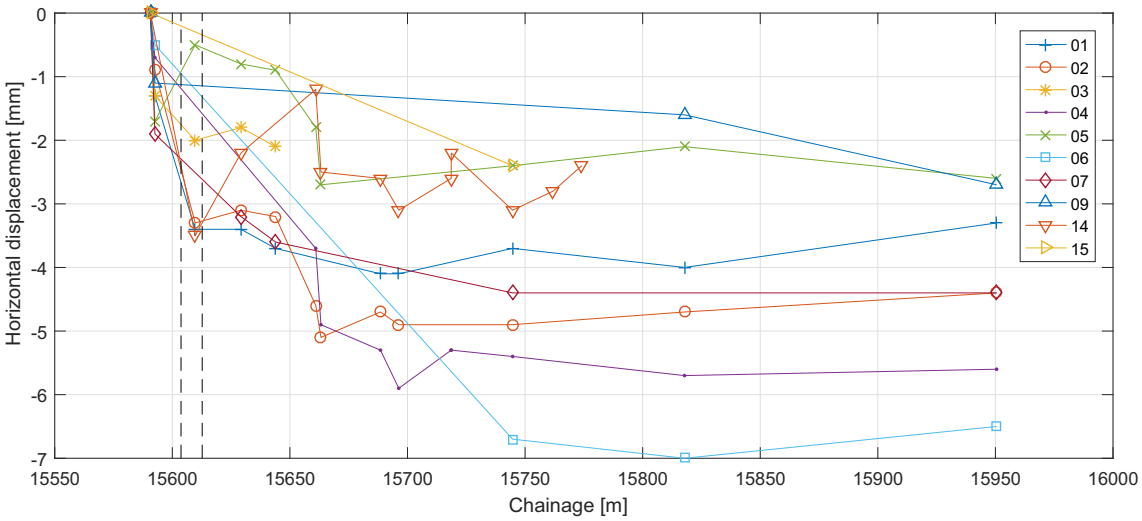

Figure 78: Horizontal displacement of MS15577 (viewing direction towards tunnel face; “+” . . . displacement right, “-”. . . displacement left; dashed lines indicate the area of the crusher)

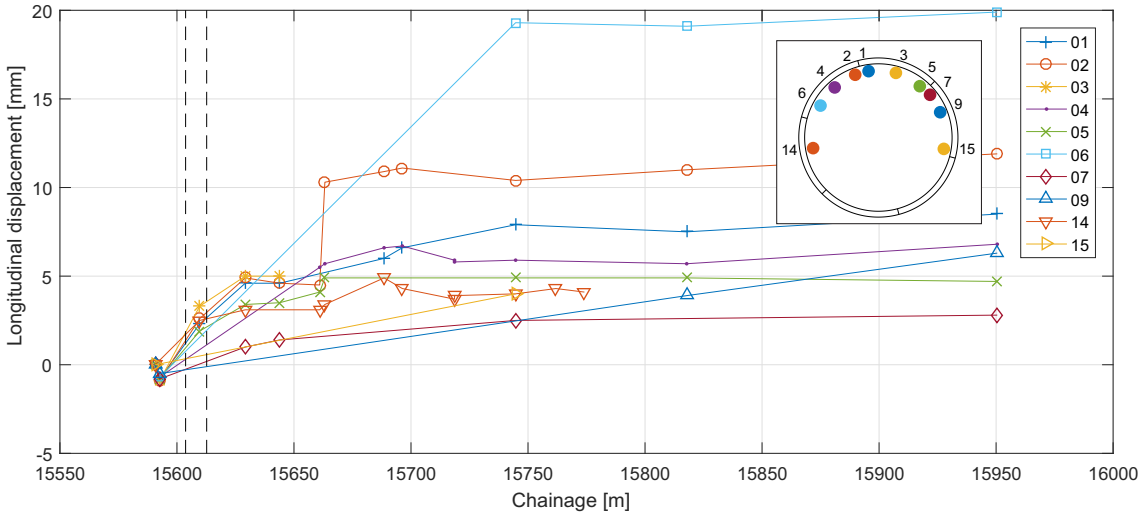

Figure 79: Longitudinal displacement of MS15577 (“+” . . . displacement in advance direction, “-”. . . displacement against advance direction; dashed lines indicate the area of the crusher)

taneous shift to the left of the ring after leaving the shield tail. Further shifts, primarily in vertical direction, occur during passage of the crusher. However, a clear allocation of the displacements to the influences of the crusher is not possible. It can be seen that there is hardly any further displacement after the third follow-up measurement.

Figure 80b shows both measuring sections in the longitudinal section. As depicted in Figure 79, it can be seen that the longitudinal displacements decrease after the second follow-up measurement All points show a movement in direction to the face. This might be due to the increasing distance of the thrust cylinders.

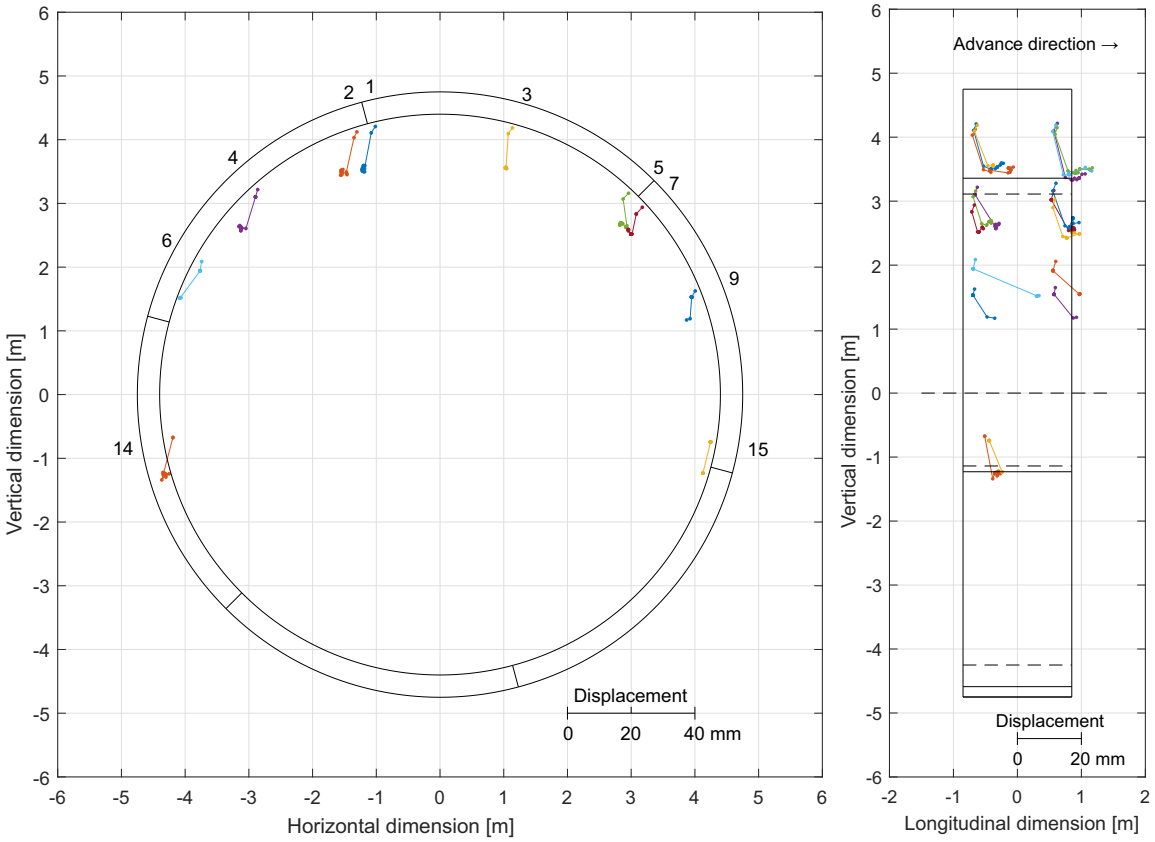

(a) Cross section of ring 7625 with measurement section 15577. (b) Longitudinal profile of ring 7625.

Figure 80: Displacement vectors in cross and longitudinal section.

Figure 81 depicts horizontal and vertical displacements in the cross section of the 15579 measuring section. The same displacement trend can be observed as in measuring section 15577.

5.1.5 Determination of the bedding improvement

Figure 82 illustrates a comparison of the fully and partially bedded rings with the same rock mass type. In relation to the advance since the installation of the segments, the shortening of the vertical half-axis is shown in Figure 82a and the numerical eccentricity in Figure 82b. The vertical half-axis – represented as the ratio b/r – exhibits a continuous reduction, which, assuming that the invert segment moves less than the crown segment, indicates a settlement of the crown segment. The fully bedded ring shows to be in the lower range of the measured deformations. The development of the numerical eccentricity ε indicates that the deformations for the bedded ring stop earlier and remain within the lower range.

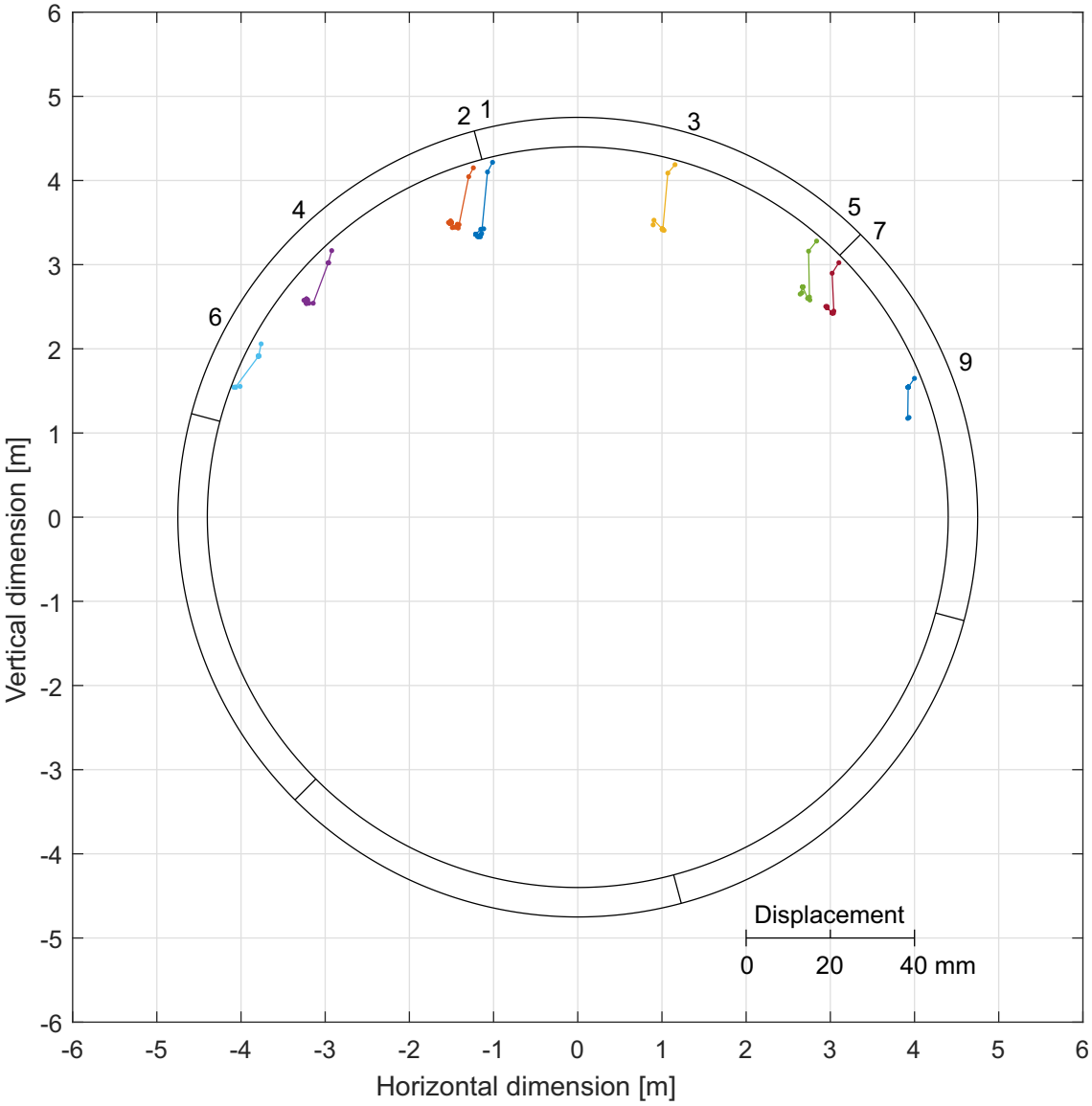

Figure 81: Displacement vectors in the cross section at MS 15579.

5.1.6 Results

The integration of geotextile tubes on the exterior surface of the segmental lining is technically feasible and justifiable. By recessed installation of the geotextile tubes damage by the passing shield tail seal can be prevented.

The displacement measurements have shown that the segmental lining undergoes a rigid body motion after leaving the shield tail with only slight angular distortions.

The filling and the resulting expansion of the geotextile tube results in a partition of the annular gap in longitudinal direction. The pea gravel is thereby prevented from relocating in longitudinal direction (rearrangement). In order to allow easy filling of the chambers created in the longitudinal direction, a working platform should be provided. With appropriate initial training it is possible to fill the geotextile tubes during the excavation process without causing any delay.

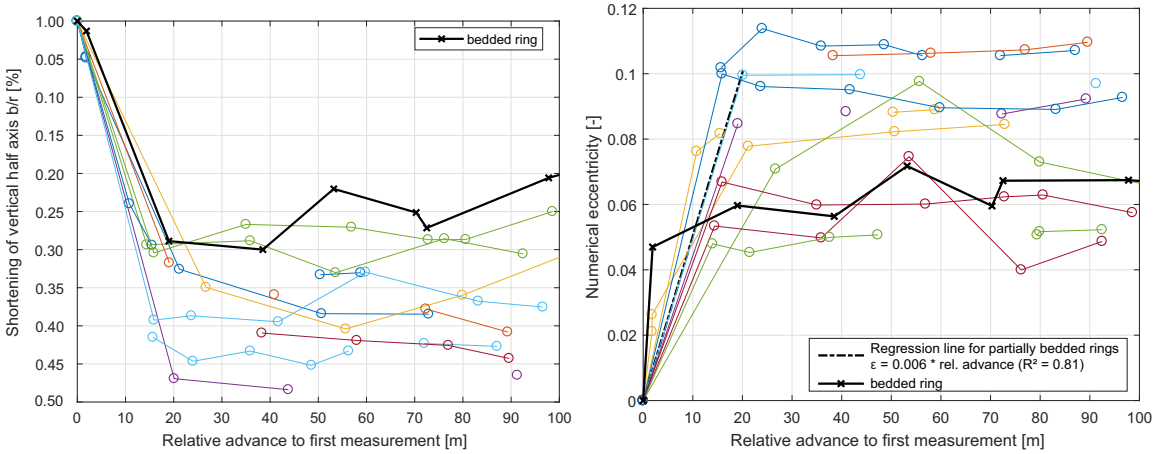

(a) Development of the normalized vertical half axis b/r in relation to the ongoing advance.

(b) Development of the numerical eccentricity in relation to the ongoing advance.

Figure 82: Comparison of the ovalization development with and without geotextile tubes (taken from Henzinger et al., 2018).

5.2 Radial yielding elements

Another approach to overcome the temporary unbedded state of the lining segments is the use of adaptive radial yielding elements. Adaptivity is required to account for varying annular gap width. Yielding of the support is needed to limit the loads on the lining in case of rock mass deformations, and thus reduce inward displacements.

The following concept is based on the fundamental idea of LSC elements. A detailed description can be found in Pejić (2016). In contrast to the suggestion of Moritz (2011b) to place the segments within the longitudinal joints in tangential direction, they have been arranged radially (see Figure 83 and 84). Thus, the elements serve as ductile yielding units between excavation and segmental lining and therefore also prevent the ovalization of the still unbedded rings leaving the shield tail.

The yielding principle is based upon at least one deformable steel pipe per lining segment with a clamping mechanism attached to the inside end (see Figure 85). Therefore, the yielding element can be placed manually within an additional circular opening in the lining segment.

The geometry of the clamping mechanism (see Figure 86) has a decisive influence on the force transmission of the yielding element into the surrounding reinforced concrete lining and the resulting additional stress concentrations in this area. A steep wedge angle results in a better bracing of the system in the opening, but also leads to a larger radial force.

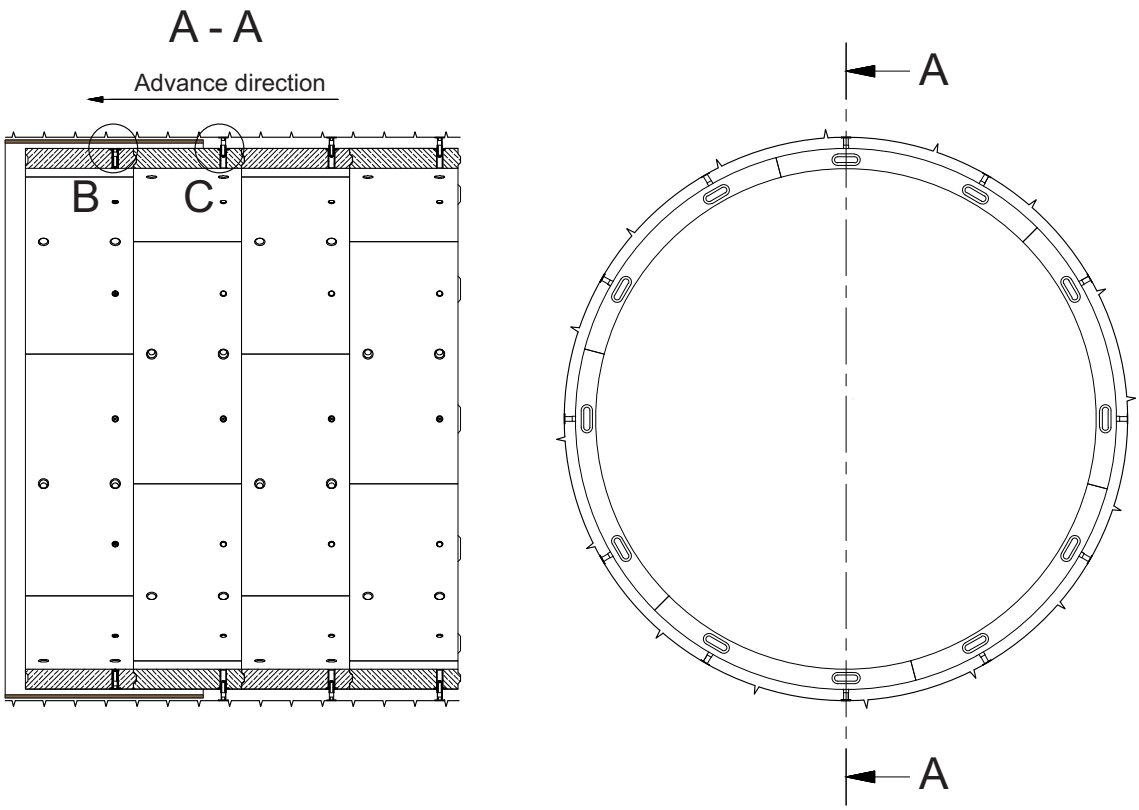

Figure 83: Segmental lining with pre-installed yielding elements; left: longitudinal section through the segmental lining; right: tunnel cross-section with radially arranged yielding elements between the rock mass and segmental lining (taken from Pejić, 2016).

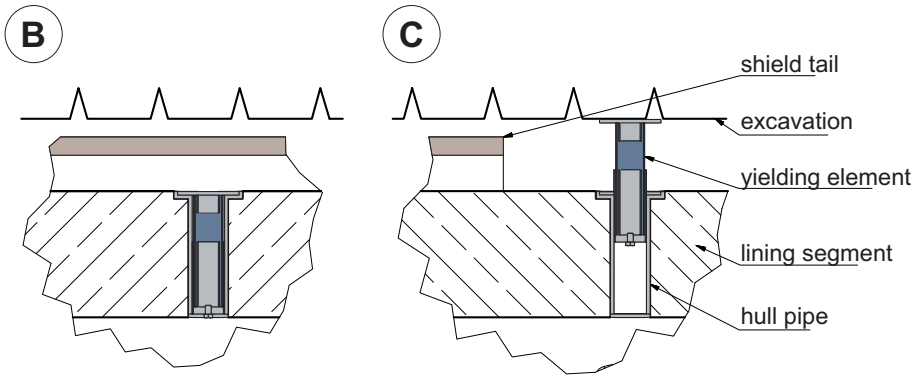

Figure 84: Pre-installed yielding elements; left: retracted; right: extended (taken from Pejić, 2016).

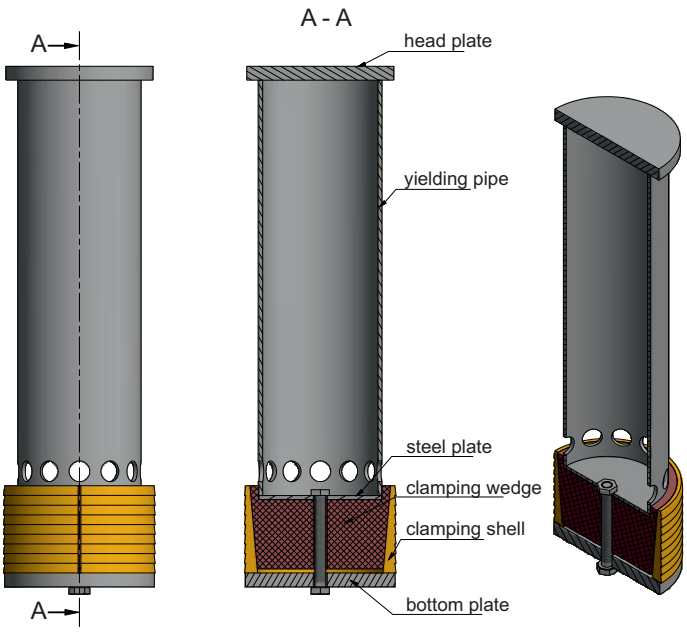

Figure 85: Design concept of the yielding element and the clamping mechanism (taken from Pejić, 2016).

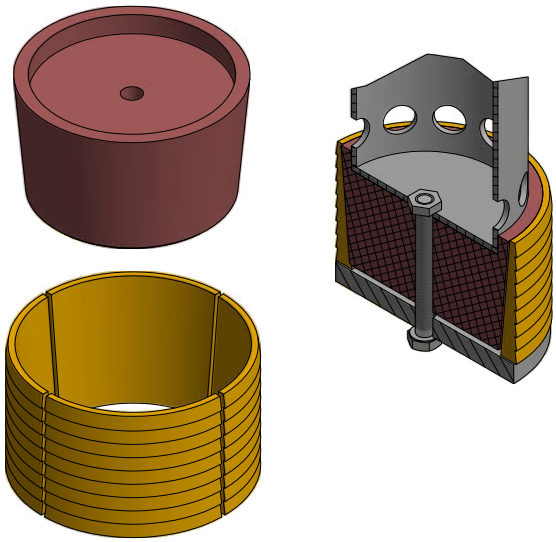

Figure 86: Clamping mechanism - clamping wedge and associated clamping shell with sawtooth profile on the outer side (taken from Pejić, 2016).

5.2.1 Laboratory tests

In order to investigate the effects on the yielding elements and the system interaction between the element and the lining segment, laboratory tests were carried out. The test setup is depicted in Figure 87.

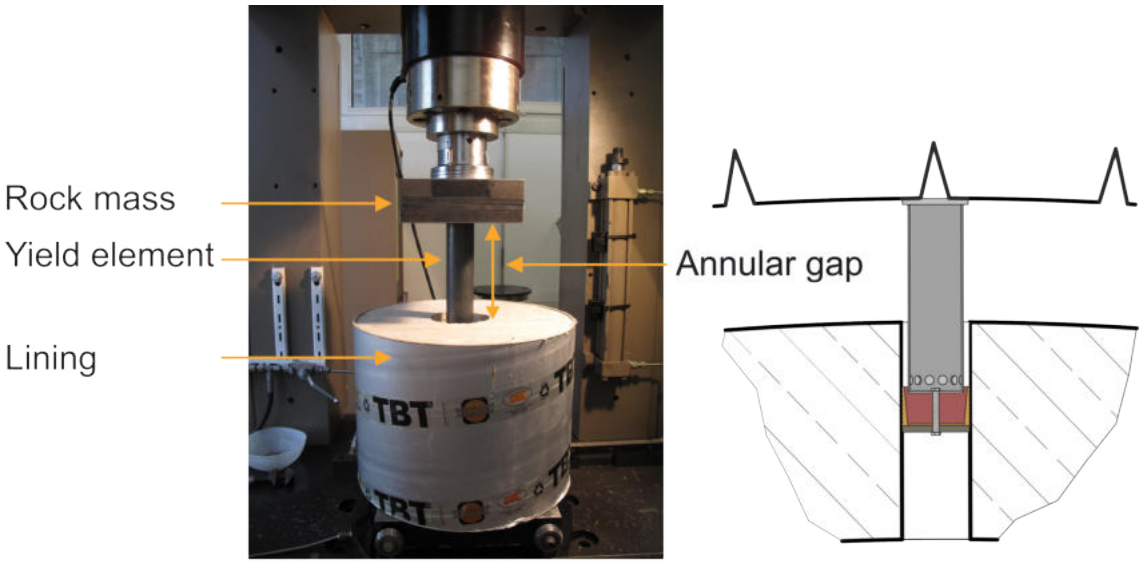

Figure 87: Test arrangement of a yielding element in a servohydraulic test facility.

A concrete body simulating the lining segment with a built-in yielding element served as test specimen on which axial load tests were carried out. The yielding element was placed in the designated concrete opening adjusted to a corresponding annular gap width of 20 cm. The procedure was then performed with a constant loading rate of 2.0 mm/min. In the experiment the yielding element was installed within a reinforced concrete body with a steel spiral (spiral diameter 150 mm, steel diameter 2 x 8.0 mm, pitch 30.0 mm).

Figure 88 shows the stress-deformation line of the examined expansion element with a clamping angle of 80°, as well as the reference curve from the preliminary tests. It can be seen that prior to the actual yielding process deformation occurs until the maximum buckling force of the steel tube is reached. The reason for this is the activation of the clamping mechanism and the elastic and plastic deformation of the plastic components.

As soon as the clamping mechanism obtains a force fitting contact with the surrounding concrete the yielding element behaves like the steel element from the preliminary tests. The buckling force reached an initial peak of 72.1 kN comparable to the reference curve from the steel tube at approximately 1.8 mm axial displacement. With the installed clamping mechanism, a buckling force of 68.8 kN can be reached at a deformation of about 6.8 mm. At approximately 24 mm of displacement, cracks occurred on the surface of the concrete body. The experiment was continued despite the visible cracks. After the second denting of the tube at a buckling force of approximately 119 kN and 36 mm displacement, a force drop to

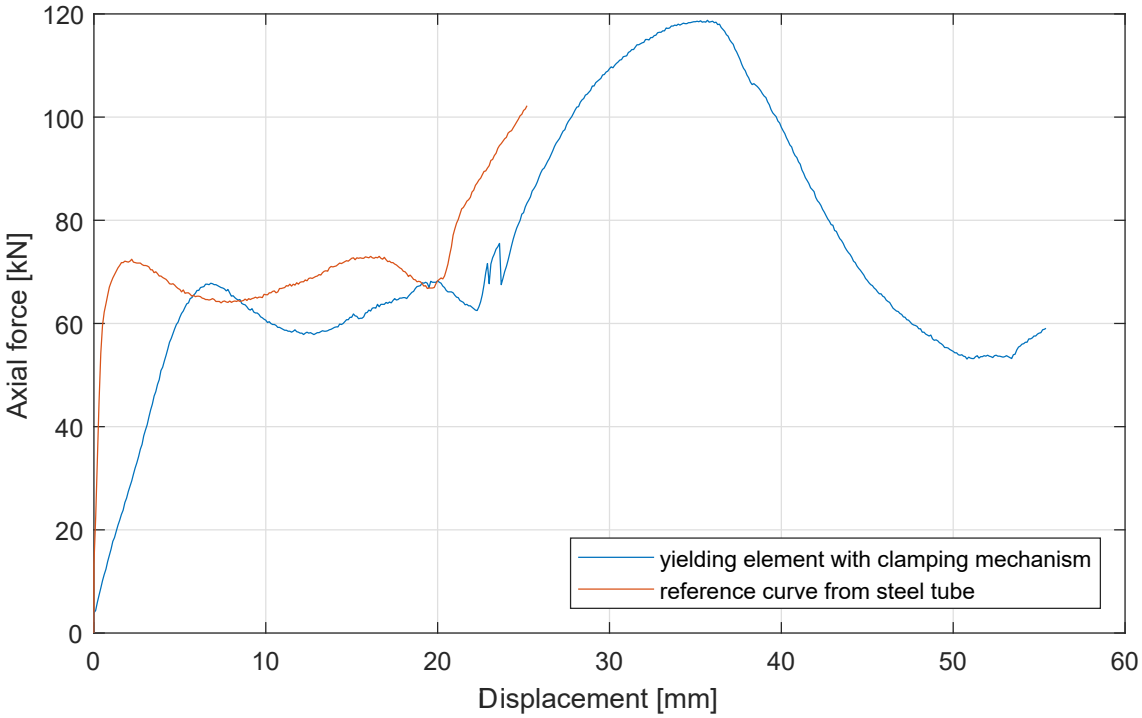

Figure 88: Working line of the expansion element with a cone inclination of 80° compared to the reference curve from the preliminary tests.

53 kN with 50.8 mm displacement followed. The experiment was terminated after a stroke of about 55 mm.

Figure 89 (left) shows the concrete body after the end of the test procedure. When inspecting the concrete opening after the removal of the element, surface cracks could be detected in the concrete opening. Figure 89 (right) shows imprints of the saw tooth profile of the clamping mechanism on the concrete surface of the installation opening.

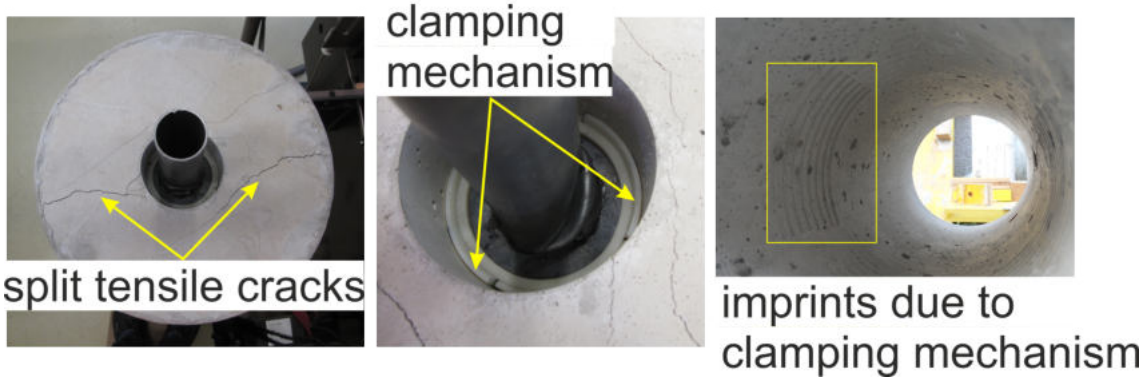

Figure 89: Reinforced concrete body after the test procedure; left: split tensile cracks at the top of the concrete body; right: imprints of the clamping shell in the concrete surface.

5.2.2 Results

The yielding element can be installed and positioned in a cylindrical opening within the lining segment, establishing an immediate contact with the surrounding rock mass. Depending on the ring clearance conditions encountered, this concept allows a flexible application of the yielding elements. The advantages of this system are the easy handling, the targeted usability, as well as the relatively low production costs.

During the laboratory tests, the steel tube showed the expected buckling behaviour and proofed proper function of the clamping mechanism, providing a force fitting contact between concrete and steel tube. After removal of the element shell, imprints were visible on the surface of the concrete opening.

The ductile elements have not been applied on site yet. For the application, additional openings as provided for the geotextile tubes are required. In addition, the requirement for a split tensile reinforcement has to be evaluated.

6 Numerical analyses

The purpose of this chapter is to study using numerical methods, the influence of the incomplete bedding and the improvements on the system behaviour which are obtained by using the geotextile tubes. This comparison can only be conducted with a profound knowledge of the system behaviour as well as by identifying the main influencing elements of the support. Hence, each group of key parameters was evaluated and calibrated using laboratory tests or analytical relationships. After the appropriateness of the numerical model has been proven, the influence of bedding improvements has been investigated.

In contrast to conventional driven tunnels the discretization of the support applied in shield TBM driven tunnels is much more complex. In order to simulate the system behaviour of segmental linings and the load redistribution within the reinforced precast concrete segments, a holistic approach used including all relevant input parameters was chosen and the results evaluated. A brief review of influences and the current approach to incorporate these into the design of the support focusing on pea gravel filled annular gaps, is provided in this chapter.

Due to the lack of numerical codes incorporating all relevant influencing factors and representing, a holistic system behaviour, a model using the FLAC^{3D} code (Itasca Consulting Group, 2017) is generated.

6.1 Determination of support parameters

The support parameters have been determined based on laboratory tests, engineering standards and applicable research findings. Nevertheless, assumptions have to be made and conclusions drawn with the upmost importance given to the qualitative and quantitative results.

6.1.1 Segmental lining

In order to meet the requirement of a realistic implementation of the structural behaviour of the segmental lining, the stress strain relationship of concrete and the interaction between reinforcement and concrete has to be considered appropriately. Therefore, extensive research and development has been performed developing and implementing the respective characteristics into FLAC^{3D} (Itasca Consulting Group, 2017).

6.1.1.1 Concrete

The requirements of concrete are defined by its strength class, exposure class and if necessary by its time dependent strength development. If the on site storage capacity is sufficient enough for a high amount of precast elements, the strength properties after 28 days can be used for the further design process. According to the ÖNORM EN 1992-1-1 (2015) the conformity of concrete is mainly determined by the characteristic concrete compressive strength, other design relevant properties of the concrete can be derived analytically. All characteristic values of concrete are calculated using a FISH routine (internal scripting language of FLAC^{3D}, with model capabilities) based on the characteristic uniaxial compressive strength.

The model parameters for concrete type C35/45 and C50/60 are listed in Table 8. The "Mohr – Coulomb" constitutive model was adopted FLAC^{3D} has proven to be appropriate for the given stress condition.

Table 8: Concrete parameters used for the numerical simulations.

Description	Unit	C35/45	C50/60
Density	[g/cm^3]	2.4	2.4
Cohesion	[MPa]	9.6	16.7
Friction angle	[^{o}]	30	30
Youngs modulus	[MPa]	34,077	37,278
Poissons ratio	[-]	0.20 (for uncracked concrete)	
Tensile strength	[MPa]	3.21	4.07
Residual tensile strength	[MPa]	0	0

6.1.1.2 Reinforcement

The reinforcement was modelled with so called "cable elements" implemented in FLAC^{3D}. For the sake of simplicity and numerical stability, only the bending reinforcement has been introduced into the model. This implementation ensures the appropriate mechanical behaviour of reinforced concrete under tensile load. In addition, the bond strength and reinforcement slip can be incorporated realistically. The cable structural elements are straight elements connected between two nodes (see Figure 90). They provide one axially oriented translational degree of freedom per node. By connecting several nodes with structural cable elements an arbitrary reinforcement can be modelled.

The structural response of the cable elements is described by two sets of parameters. One for describing the mechanical behaviour of the cables and the other for the interaction between cables and the surrounding numerical grid.

Under axial load the material behaviour of rebars is described using an elastic, perfectly plastic material law. The necessary elastic and strength properties derived

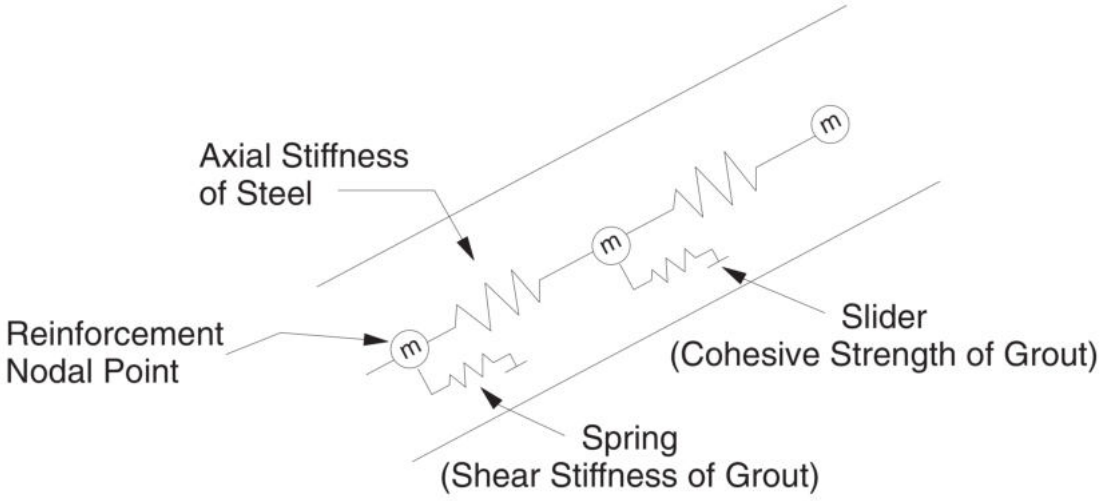

Figure 90: Mechanical representation of fully bonded reinforcement (taken from Itasca Consulting Group, 2017).

for reinforcement steel are listed in Table 9.

Table 9: Mechanical parameters for rebars (steel type BSt 550 according to ÖNORM B 4707, 2017

Description	Unit	
Density	[g/cm^3]	7.85
Cross section area (ø 1 cm)	[cm^2]	0.79
Stress yield	[MPa]	550
Young's modulus	[MPa]	200,000

The mechanical parameters describing the shear interaction between rebar and surrounding material are solely formulated for a grouted annulus. Hence, the equations have to be reformulated in order to capture the interaction of precast lining segments and reinforcement within FLAC^{3D}. Assuming constant elastic and strength properties the implementation is trivial. The strength between cables and grid is expressed by the Mohr-Coulomb failure criterion.

Strength and deformability parameters for reinforcement can be chosen with regard to the steel quality. Due to the linear elastic and perfectly plastic behaviour, further processing is not necessary.

In order to describe the deformation behaviour between reinforcement and the surrounding grout/concrete, Farmer (1975) has developed an analytical relationship between shear stress and displacement along a loaded resin grouted rock anchor. The results obtained, have been shown to be satisfactory for strength and deformability properties close to concrete. In further research St. John & van Dillen (1983) have described and developed a numerical formulation based on the analytical ap-

proach by Farmer (1975). In addition, rockbolt and grout parameters have been incorporated for a rational tunnel design. This implementation represents the state of the art at present in commonly applied numerical codes. The implemented constitutive model derives the shear stiffness based on the shear modulus of the grout and the diameter of the reinforcement as well as the thickness of the annulus. Figure 91 illustrates the shear stress distribution around the rock bolt in radial direction.

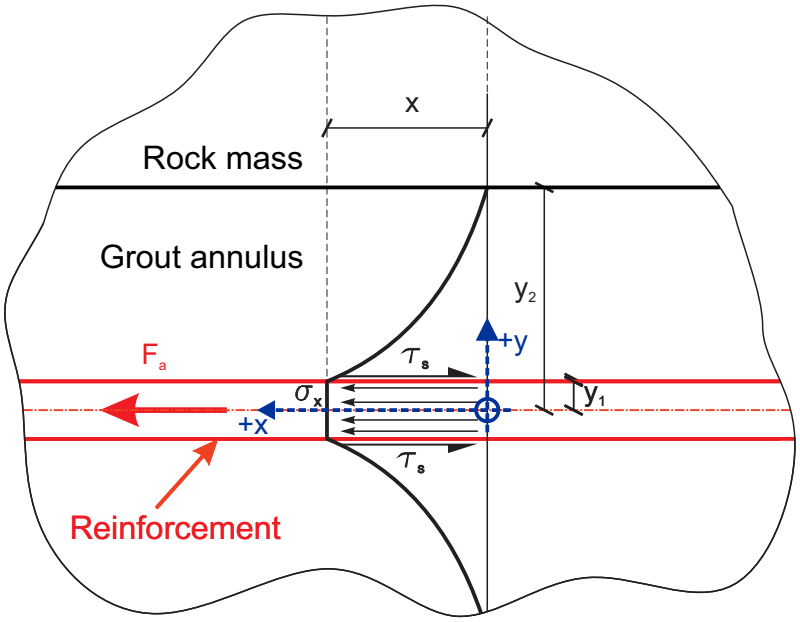

Figure 91: Stress situation around the rock bolt. F_a – axial force acting on the reinforcement, σ_x – normal stress acting within the reinforcement due to the axial force F_a, $\tau_s(y)$ – shear stress in the concrete section at the distance y from the datum axis, y_1 – reinforcement radius, x – considered longitudinal extent,z_{min} – minimal concrete cover.

Since the stiffness is an extensive property, it is influenced by the shear modulus as well as the given geometry implemented in the constitutive model for cable elements within FLAC^{3D}. The bond stiffness is defined as:

$$k_b = \frac{2 \cdot \pi \cdot G}{\ln\left(\frac{y_2}{y_1}\right)} \tag{24}$$

where:
- k_b ..... Bond stiffness [MN/m]
- G ..... Shear modulus of grout [MPa]
- y_1 ..... Reinforcement radius [m]
- y_2 ..... Borehole radius [m]

With the given situation of a direct contact between reinforcement and concrete, the annulus reduces to zero. Hence, the bond stiffness increases to infinity according to equation 24, thus it was limited with a certain value (see Table 10).

Since the bond strength between cable elements and the finite difference grid is characterised by a Mohr – Coulomb strength criterion, friction angle and cohesion

have to be provided. According to ÖNORM EN 1992-1-1 (2015) the ultimate bond strength between concrete and reinforcement can be determined based on the characteristic axial tensile strength (5 % quantile) formulated in equation 25.

$$f_{ctk,0,05} = 0.7 \cdot f_{ctm} \tag{25}$$

where: $f_{ctk,0,05}$ ..... Characteristic axial tensile strength of concrete [MPa] (5 % quantile)
f_{ctm} ..... Mean value of axial tensile strength of concrete [MPa]

Hence, the ultimate bond strength is given as:

$$f_b = 2,25 \cdot f_{ctk,0,05} \quad (\text{for } \varnothing \leq 32mm \text{ and good bond conditions}) \tag{26}$$

where: f_b ..... Bond strength between rebar and mortar [MPa]
$f_{ctk,0,05}$ ..... Characteristic axial tensile strength of concrete [MPa] (5 % quantile)

Neglecting frictional effects due to the low confinement pressure within the segmental lining the cohesive strength is calculated straightforward (St. John & van Dillen, 1983) from:

$$c_{peak} = \pi \cdot 2 \cdot y_1 \cdot Q_B \tag{27}$$

where: c_{peak} ..... Peak shear strength between concrete and rebar [MPa]
y_1 ..... Rebar diameter [m]
Q_B ..... Quality of bond between rebar and concrete [-]

Q_B describes the quality of the bond between the cable element and the finite difference grid and equals 1 for good bonding. Hence, the value is set to 1 since the production conditions of reinforced lining segments are favourable compared to rock bolts.

Table 10: Parameters for shear interaction between rebars and concrete.

Description	Unit	
Diameter of the bar	[cm]	1.00
Circumference of the bar	[cm]	3.14
Bond stiffness	[MN/m]	392.50
Bond cohesion	[MPa/m]	0.12
Bond friction angle	[°]	0

6.1.1.3 Verification

The use of the "cable elements" as reinforcement in FLAC^{3D} was verified investigating the behaviour of reinforced concrete beams. A uniaxial tensile test and a

bending test exceeding the tensile strength of concrete were simulated numerically. Both were verified by means of analytical calculation methods. For both cases, the degree of reinforcement is

$$\rho = \frac{A_s}{A_c} = 0.0045 \tag{28}$$

where: ρ ..... Reinforcement degree [-]
A_s ..... Reinforcement cross-sectional area [m^2]
A_c ..... Concrete cross-sectional area [m^2]

and the ration of the elastic moduli can be written as:

$$\alpha_e = \frac{E_s}{E_c} = 5.37 \tag{29}$$

where: ρ ..... Ratio of elastic moduli [-]
E_s ..... Young's modulus of reinforcement [MPa]
E_c ..... Young's modulus of concrete [MPa].

Distribution of the forces under elastic axial compression

Assuming the compatibility condition $\varepsilon_s = \varepsilon_c$ and a linearly elastic material behaviour, the following occurs:

$$\frac{\sigma_c}{E_c} = \frac{\sigma_s}{E_s} \tag{30}$$

where: σ_c ..... Concrete stress [MPa]
E_c ..... Young's modulus of concrete [MPa]
σ_s ..... Reinforcement stress [MPa]
E_s ..... Young's modulus of reinforcement [MPa]

The equilibrium condition is expressed as:

$$F = F_c + F_s \tag{31}$$

where: F ..... Total force [MN]
F_c ..... Concrete force [MN]
F_s ..... Reinforcement force [MN]

Hence, the concrete and reinforcement force can be reformulated as shown below:

$$F_c = \frac{F}{1 + \alpha_e \cdot \rho} \tag{32}$$

$$F_s = F \cdot \frac{\alpha_e \cdot \rho}{1 + \alpha_e \cdot \rho} \tag{33}$$

where:
F ..... Total force [MN]
F_s ..... Reinforcement force [MPa]
F_c ..... Concrete force [MPa]
α_e ..... Ratio of elastic moduli [-]

Figure 92 depicts the load distribution in concrete and reinforcement due to axial compression. The numerical results correspond well with the analytical values. Hence, the applicability of the "cable elements" has been proven for the elastic state.

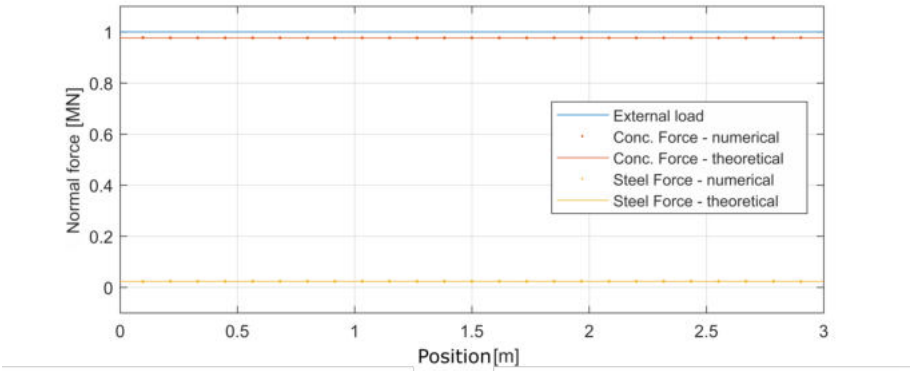

Figure 92: Load distribution within an elastic beam.

Bending moment development with plastic deformation

The concrete – reinforcement interaction in plastic conditions was verified with a gradual increase of a uniformly distributed load on a beam (see Figure 93). The deflections in the center of the beam calculated for each load step were compared with the analytical solution of the corresponding analytical solution for the bending deformation and the concrete reinforcement interaction, based on König et al. (2008).

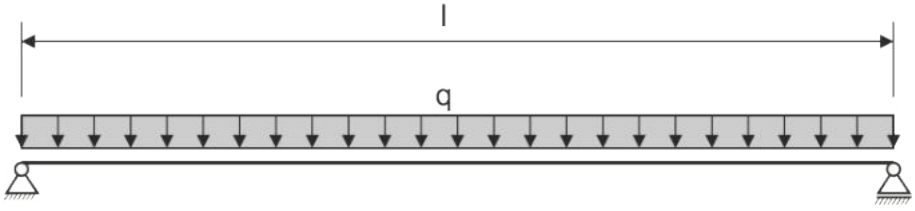

Figure 93: Static model for the investigation of the reinforcement – concrete interaction.

After applying the described method, the cracking development due to tensile loads can be reproduced in FLAC^{3D}. Figures 94 and 95 show the beam in the uncracked and cracked state.

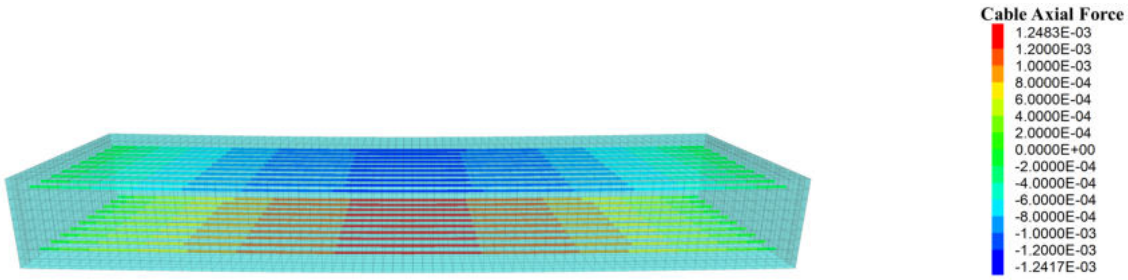

Figure 94: Bending beam with elastic deformation. Reinforcement forces in MN.

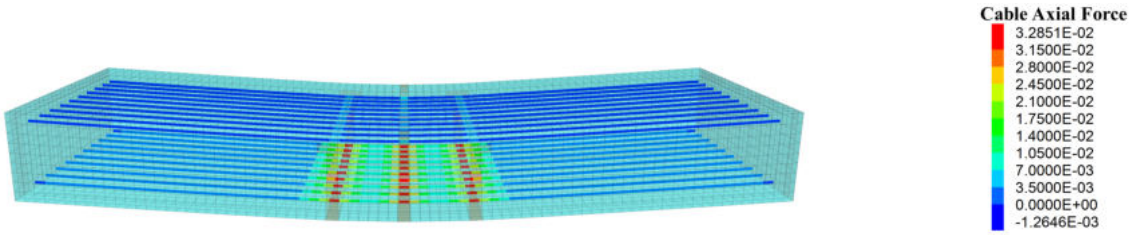

Figure 95: Bending beam with plastic deformation. Reinforcement forces in MN.

The results obtained show an excellent agreement between the numerical results and the analytical solution in elastic conditions. With plastic deformations only minor discrepancies can be captured between the two results (see Figure 96). On the basis of this calculation result, the applied concrete – reinforcement modelling method is considered as verified.

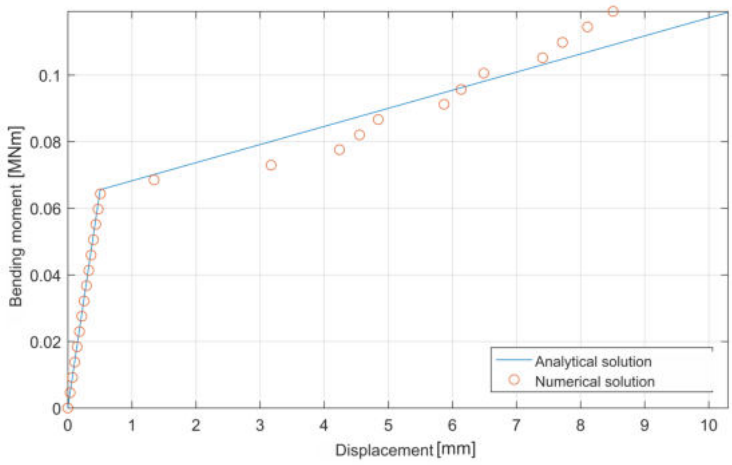

Figure 96: Deflection – bending moment relationship of a reinforced concrete beam. Comparison between the analytical solution and the numerical results.

6.1.2 Contact interactions

In order to simulate discrete contact behaviour between different finite bodies numerically, FLAC^{3D} provides interface elements that are characterized using the Mohr – Coulomb shear strength criterion. The elastic behaviour is described by the normal and shear stiffness. The shear strength limit is defined by the cohesion and friction angle. The dilation angle causes an increase of normal force after the shear strength limit is reached. The tensile behaviour is solely influenced by the tensile strength. Figure 97 illustrates the relevant components for the interaction between two surfaces.

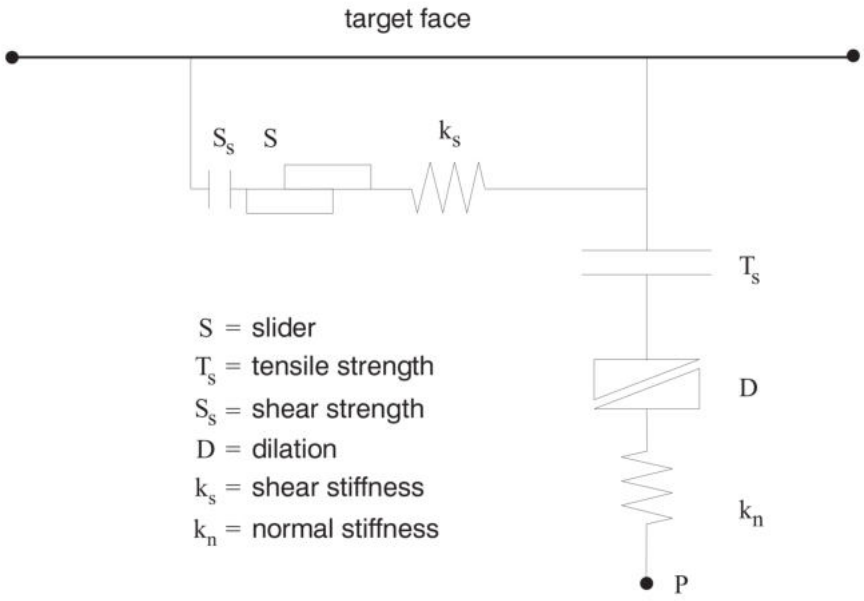

Figure 97: Components of the bonded interface constitutive model (taken from Itasca Consulting Group, 2017).

Interfaces have been used to simulate the interaction between pea gravel and segmental lining, as well as the excavation boundary. In addition, they have been introduced along the contact joints of adjacent lining segments.

6.1.2.1 Concrete joints

The deformation kinematics of the segmental lining is influenced by the longitudinal and radial joints to a considerable extent. Within the numerical model, the concrete joints were introduced in a discrete form as they are supposed to be.

The longitudinal joints were evaluated according to the analytical approach by Leonhardt & Reimann (1965). Figure 98 depicts the deformation characteristic of the longitudinal joint. The approach is based on the assumption that the Young's modulus is constant and that the adjacent region participating in the deformation equals the width of the joint.

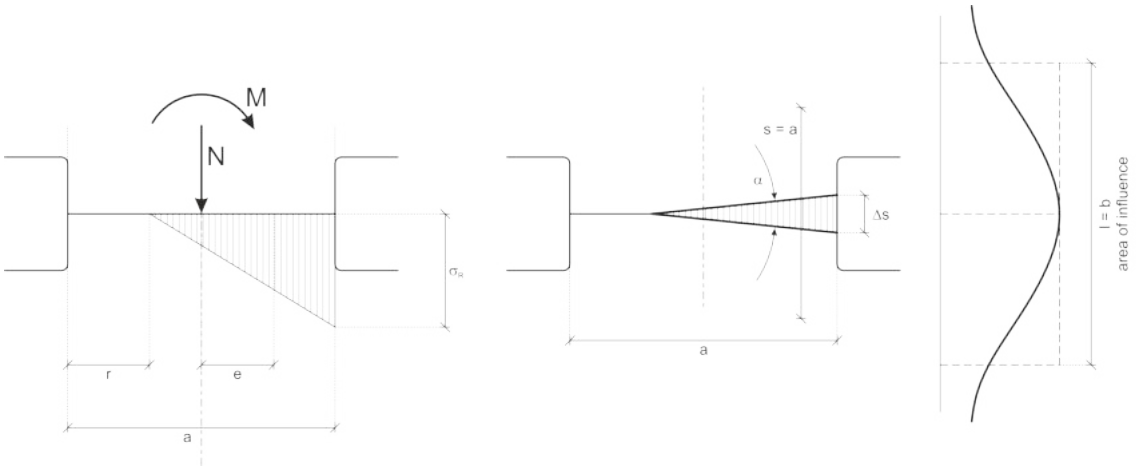

Figure 98: Approach for estimating the rotational resistance of concrete joints (amended after Leonhardt & Reimann, 1965).

Assuming an eccentric load, an uneven stress distribution develops. The normalized eccentricity is defined as:

$$m = \frac{e}{b} = \frac{M}{N \cdot b} = \frac{1}{6} \cdot \left(2 \cdot \frac{a}{b} + 1\right) \tag{34}$$

where:
- m ..... Normalized eccentricity [-]
- e ..... Eccentricity of resulting force [m]
- a ..... Joint width [m]
- b ..... Joint depth [m]
- M ..... Bending moment [kNm]
- N ..... Normal froce [kN]

The normalized rotation angle is given as follows:

$$\frac{\alpha}{K} = \frac{1}{(1-2 \cdot m)^2} \qquad \text{with } K = \frac{8 \cdot N}{9 \cdot a \cdot b \cdot E} \tag{35}$$

where:
- α ..... Rotation angle [°]
- m ..... Normalized eccentricity [-]

Hence, the angle of rotation of the joint is:

$$\alpha = \frac{1}{b-a} \cdot \frac{\sigma_R \cdot b}{E} = \frac{K}{(1-2 \cdot m)^2} \tag{36}$$

where:
- b ..... Joint depth [m]
- a ..... Joint width [m]
- σ_R ..... maximum stress with joint (at the edge) [MPa]
- E ..... Young's modulus of concrete [MPa]
- m ..... Normalized eccentricity [-]

To investigate the influence of the interface normal stiffness on the rotation, a numerical model was again generated in FLAC^{3D}. In this case, the applied bending moment was varied for two Young's moduli according to ÖNORM EN 1992-1-1 (2015) for the concrete classes C35/45 and C50/60.

Figures 99 and 100 show the relationship between normalized eccentricity and the related angle of rotation. In this case, the theoretical development according to Leonhardt & Reimann (1965) is compared with the numerical results as a function of the normal stiffness of the interface.

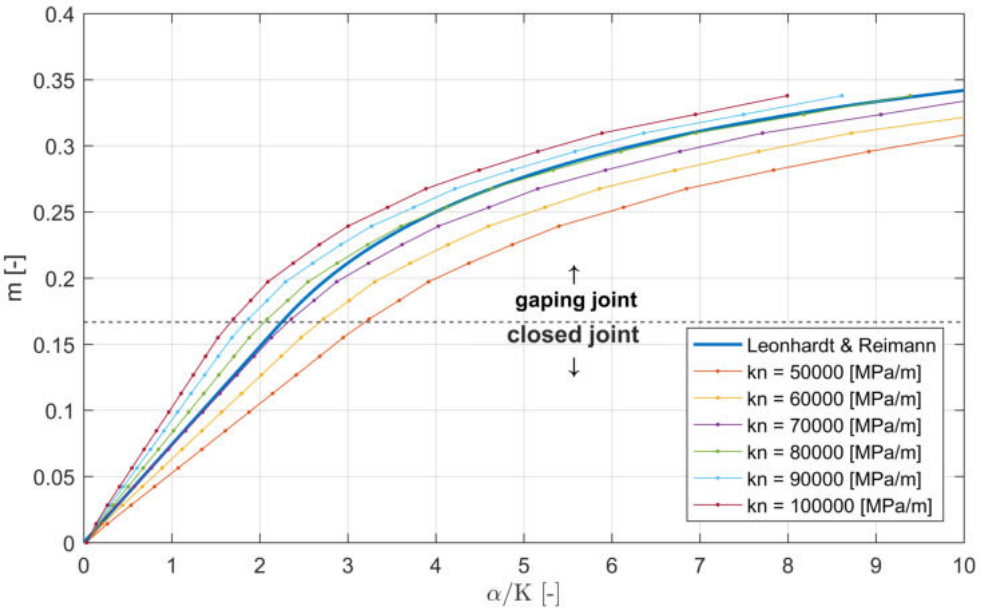

Figure 99: Normalized eccentricity – related angle relationship for concrete class C35/45

The simulations show that for concrete strength classes C35/45 and C50/60 the normal stiffnesses 100,000 and 110,000 MPa/m respectively provide the best agreement with the theoretical results.

The remaining parameters, with the exception of the tensile strength, have no influence on the results. However, the assumption is that the tensile strength is zero. The friction angle between two concrete surfaces varies between 37°and 45°. The shear stiffness was assumed to be sufficiently accurate with 1/10 of the normal stiffness. The input parameters are listed in Table 11.

The deformation behaviour of the radial joints is essentially influenced by the prop-

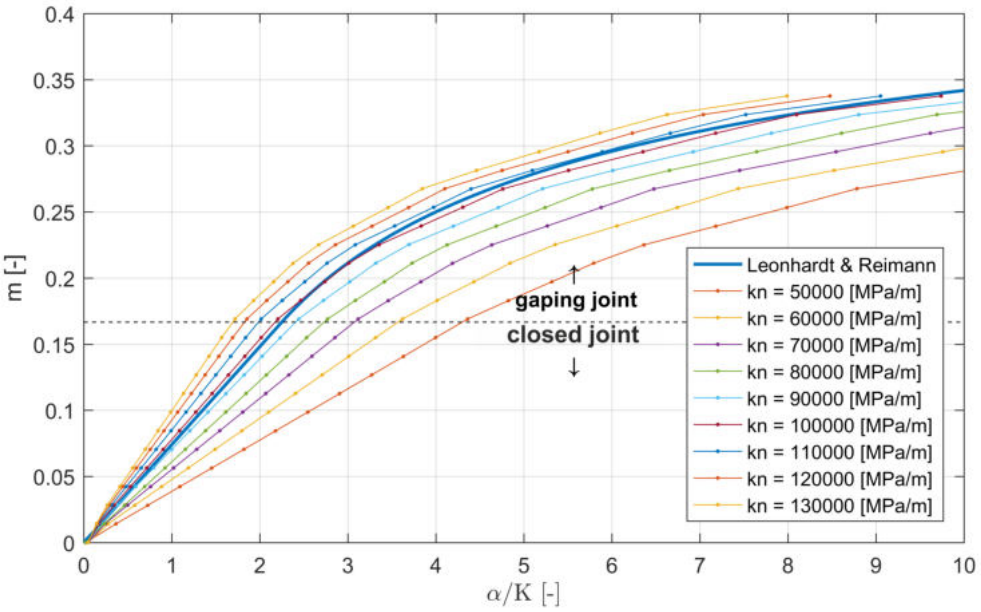

Figure 100: Normalized eccentricity – related angle relationship for concrete class C50/60

Table 11: Parameters of the longitudinal joints.

Description	Unit	C35/45	C50/60
Normal stiffness	MPa/m	100.000	110.000
Shear stiffness	MPa/m	10.000	11.000
Cohesion	MPa	0	0
Friction angle	°	37	37
Dilation angle	°	0	0
Tensile strength	MPa	0	0

erties of the hardboard inlays. For the given situation two hardboard inlays with an area of 0.199 m^2 and a thickness of 3.2 mm have been used. With a Young's modulus of 100 MPa, a shear modulus of 80 MPa and a friction coefficient of 0.5 - 0.7 between concrete and hardboard, the contact conditions can be directly derived (Fischer et al., 2013). The normal stiffness results from:

$$k_n = \frac{E_{hb} \cdot A_{hb}}{t_{hb}} \tag{37}$$

where:
k_n ..... Interface normal stiffness [MPa/m]
E_{hb} ..... Young's modulus of hardboard [MPa]
A_{hb} ..... Contact area of hardboard [m^2]
t_{hb} ..... Thickness of hardoard [m]

The shear stiffness can be expressed as:

$$k_s = \frac{G_{hb} \cdot A_{hb}}{t_{hb}} \tag{38}$$

where: k_s ..... Interface shear stiffness [MPa/m]
G_{hb} ..... Shear modulus of hardboard [MPa]
A_{hb} ..... Contact area of hardboard [m^2]
t_{hb} ..... Thickness of hardoard [m]

To improve the numerical stability, the modelling of the hardboard was omitted. Since the interfaces were modelled along the radial joints, the contact stiffness had to be multiplied by the ratio of the contact area of the hardboard and the contact area of the segmental lining. The input parameters are listed in Table 12.

Table 12: Parameters of the radial joints.

Description	Unit	
Normal stiffness	MPa/m	2.111
Shear stiffness	MPa/m	845
Cohesion	MPa	0
Friction angle	°	27
Dilation angle	°	0
tensile strength	MPa	0

6.1.2.2 Segmental lining – pea gravel – rock mass interaction

In order to properly simulate the interaction between the lining segments, pea gravel and the rock mass, an interface was introduced at both contact boundaries. The numerical parameters had to be chosen without analytical or empirical verification. Since the interface elements were introduced only to allow radial separation of the media, normal stiffness and shear stiffness were set as high as possible. The FLAC^{3D} manual provides a guideline for determining stiffness parameters to construct such functional “interfaces”:

$$k_n = k_s = \frac{K + \frac{4}{3} \cdot G}{\Delta z_{min}} \tag{39}$$

where:
- k_n ..... Interface normal stiffness [MPa/m]
- k_s ..... Interface shear stiffness [MPa/m]
- K ..... Bulk modulus of continuum [MPa]
- G ..... Shear modulus of continuum [MPa]
- Δz_{min} ..... Smallest width of an adjoining zone in the normal direction [m]

The bulk and shear modulus are derived from the stiffest adjacent zone of the interface. Δz_{min} represents the smallest edge length of an adjacent zone (see Figure 101).

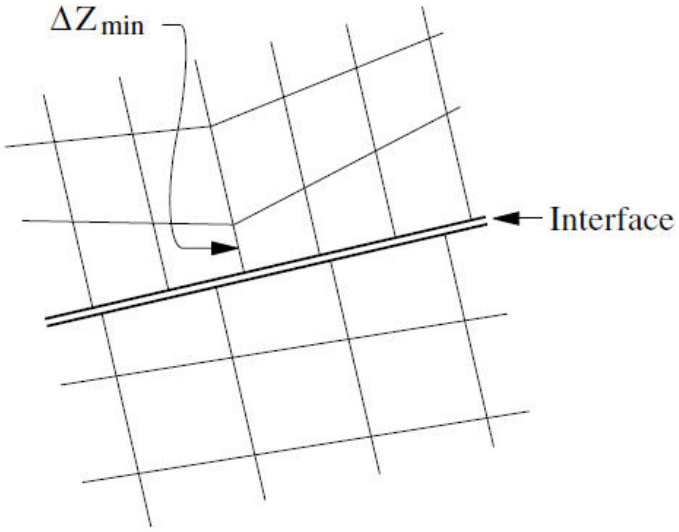

Figure 101: Numerical replica of pea gravel.

All strength parameters except the friction angle were set to 0. The input parameters for these contact conditions are listed in Table 13.

Table 13: Parameters of the contact between lining segments, pea gravel and rock mass.

Description	Unit	
Normal stiffness	[MPa/m]	100.000
Shear stiffness	[MPa/m]	100.000
Cohesion	[MPa]	10
Friction angle	[°]	0
Dilation angle	[°]	0
Tensile strength	[MPa]	0

6.1.3 Pea gravel

As shown in chapter 3, the Young's modulus of pea gravel depends on the stress level and the loading type. For this reason, the "Plastic – Hardening" material

law, recently introduced in the FLA3D code has been used. This constitutive model considers the consolidation of volumetric and deviatoric stress mentioned by Cheng & Detournay (2016). The hyperbolic relationship between axial strain and deviatoric stress is based on the assumption of Duncan & Chang (1970). The nonlinear plasticity is based on the findings of Schanz et al. (1999).

The strength parameters of pea gravel are adopted from the shear test described in chapter 3. Since pea gravel is a non cohesive material, tensile strength equals zero. The dilation angle is also assumed to be zero in order to avoid an overestimation of the shear strength during plastic deformation.

The elasticity parameters can only be derived by numerical simulation of the large oedometer tests shown in chapter 3. The comparison between laboratory and numerical results is shown in Figure 102.

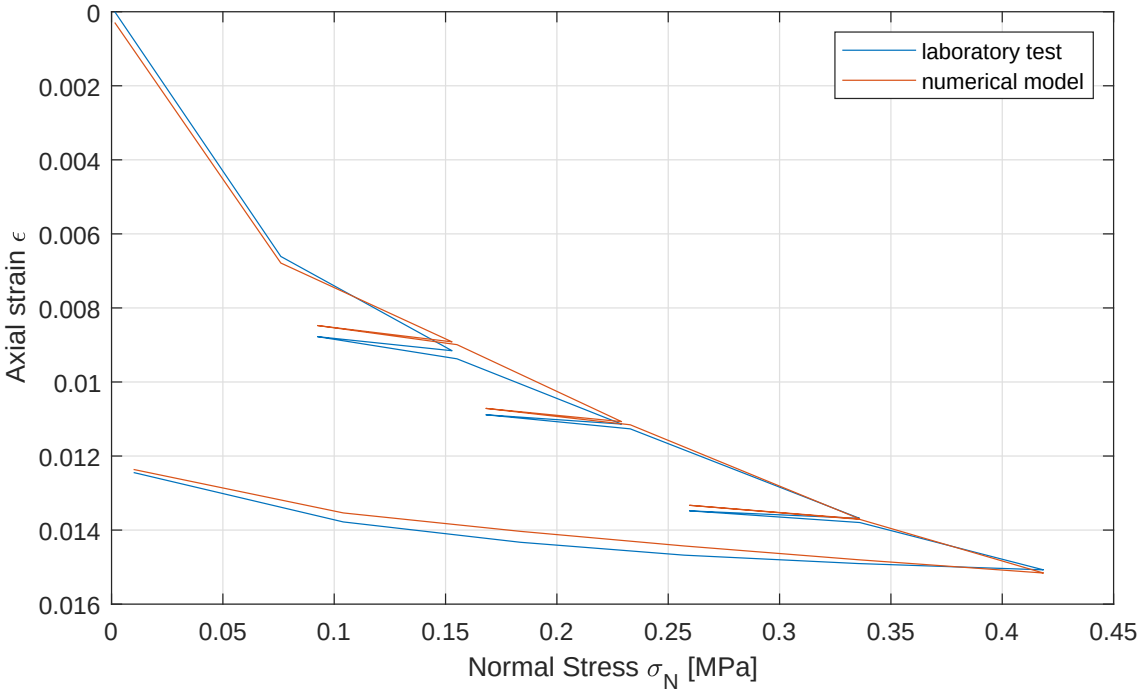

Figure 102: Comparison of laboratory and numerical results for pea gravel.

The input parameters for pea gravel are listed in Table 14.

6.2 Investigation of the bedding influence with a gradual load increase

Along the circumferential extent, concrete cracks significally influence the distribution of bending moment and normal forces in the segmental lining. Hence it was decided to examine the influence of an inhomogeneous loading and bedding condition.

Table 14: Mechanical parameters of pea gravel (“Plastic Hardening”).

Property	Unit	
Dry density	g/cm^3	16
Cohesion	MPa	0.001
Friction angle		38
Dilation angle		0
Tensile strength	MPa	0.0
Secant stiffness – E50	MPa	26
Unloading - reloading stiffness – Eur	MPa	160
Tangent stiffness modulus – Eoed	MPa	26
Poisson’s ratio	-	0.25
Reference pressure	MPa	0.1
Failure ratio	-	0.9
Exponent for elastic moduli	-	0.5

6.2.1 Numerical model

The numerical model consists of 6 segments per ring. In total 6 rings have been simulated. At the rear end facing the tunnel portal a longitudinal boundary condition limits the model. The front end facing the tunnel face is limited either by a longitudinal boundary condition or a homogeneous load representing the load of the thrust cylinders applied on the lining segments.

In order to determine the bending moments, the forces of all zones in tangential direction and those of the reinforcement layers were multiplied with the distance to the center axis of the segment (Figure 103). For the sake of simplicity the neutral axis was assumed in the middle of the segmental lining. Incorporation the axial forces of the reinforcement bars the bending moment at every circumferential position within the concrete structure was calculated.

Starting at 0 kN a uniform load is applied in ten steps each with 50 kN in the top heading (see Figure 103). The mobilized reaction forces along the lining segments were used to calculate the bending moment and the normal forces along the tunnel support.

The different bedding conditions considered are shown in Figure 104. All the load steps have been computed with fully bedded and partially bedded situations, showing the influence of an incomplete bedding.

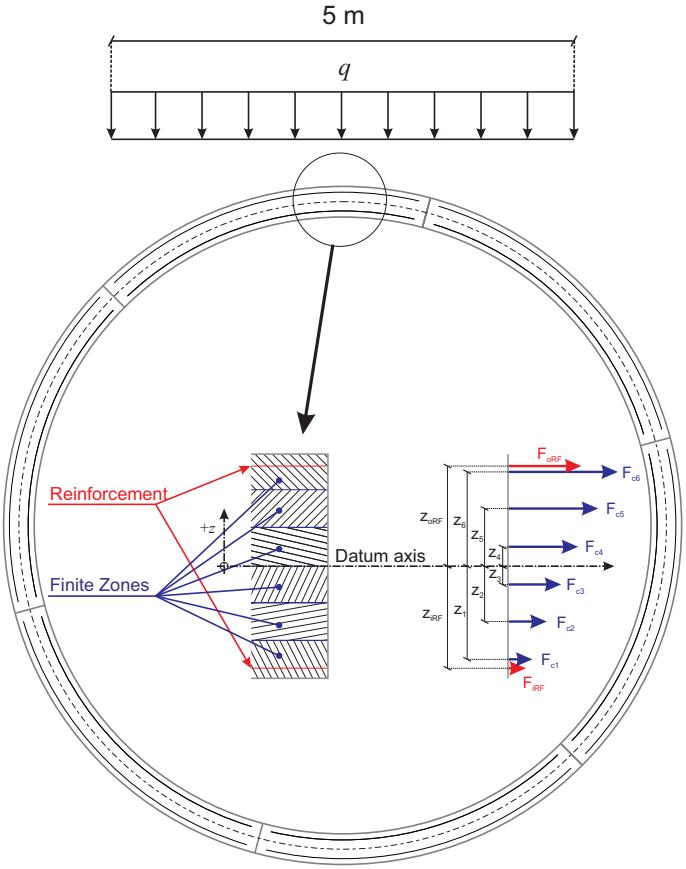

Figure 103: Load distribution along the segmental lining.

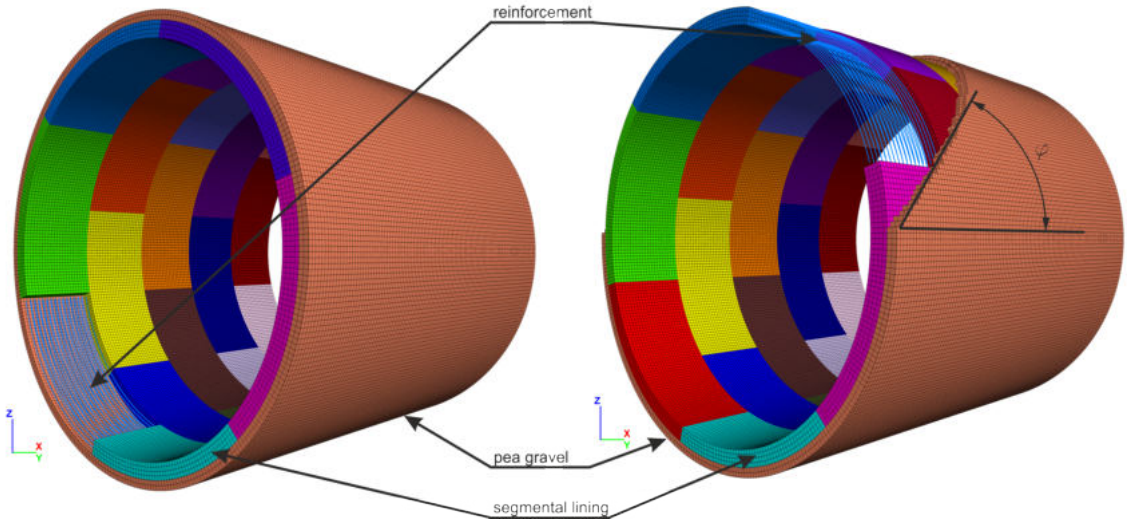

Figure 104: Discretization of the vicinity of the excavation in fully bedded (left) and partially bedded (right) state.

6.2.2 Results

Using FLAC^{3D} the results obtained for each zone in the lining segments have been determined at every load step.

In Figure 105 the bending moment distribution is shown for a bedding angle of 90° and 32° and a thrust force of 10 MN. The bending moment distribution exhibits several discontinuities. These denote tension cracks within the concrete segments.

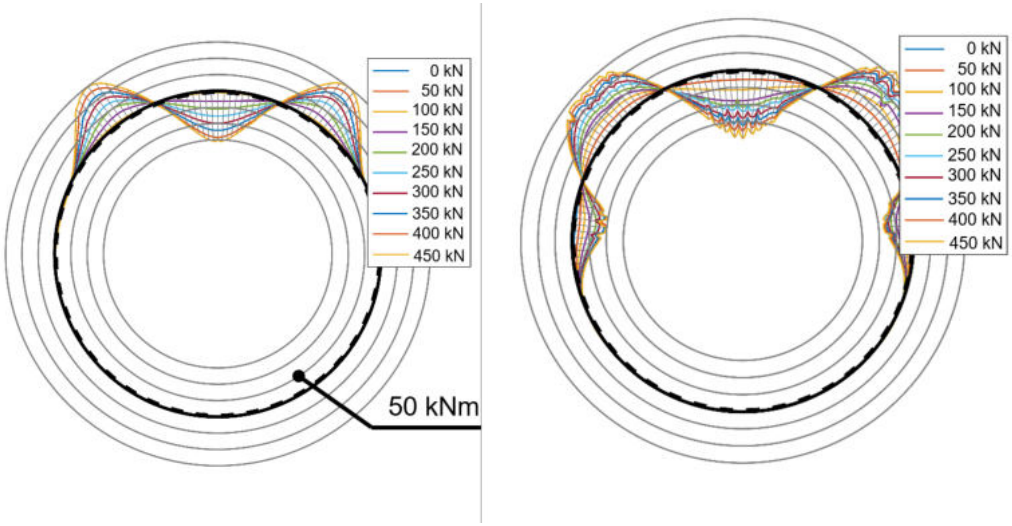

(a) Fully bedded. (b) Partially bedded.

Figure 105: Distribution of bending moment in the middle of the first ring after the shield tail for each load step.

On the inner side of the segmental lining the radial displacements have been plotted as shown in Figure 106. A linear increase of crown settlements correlates with the step wise increase of the vertical load. The plotted results are for a sloped bedding situation with 90° and 32° and a thrust force of 10 MN.

The presented use of continuum elements and discrete reinforcement modelling provides plausible results regarding crack propagation (see Figure 107) which correspond with the on-site observations. A spatial illustration of crack development requires only a small number of additional parameters in comparison to the beam spring model. The actual load capacity is higher than suggested by a design based on ÖNORM EN 1992-1-1 (2015). The crack propagation only indicates an increased utilization and loss of serviceability (in case water tight support is required), but not a risk of the lining stability. As seen in the section forces — as observed in reality — an incomplete bedding situation represents the design relevant case.

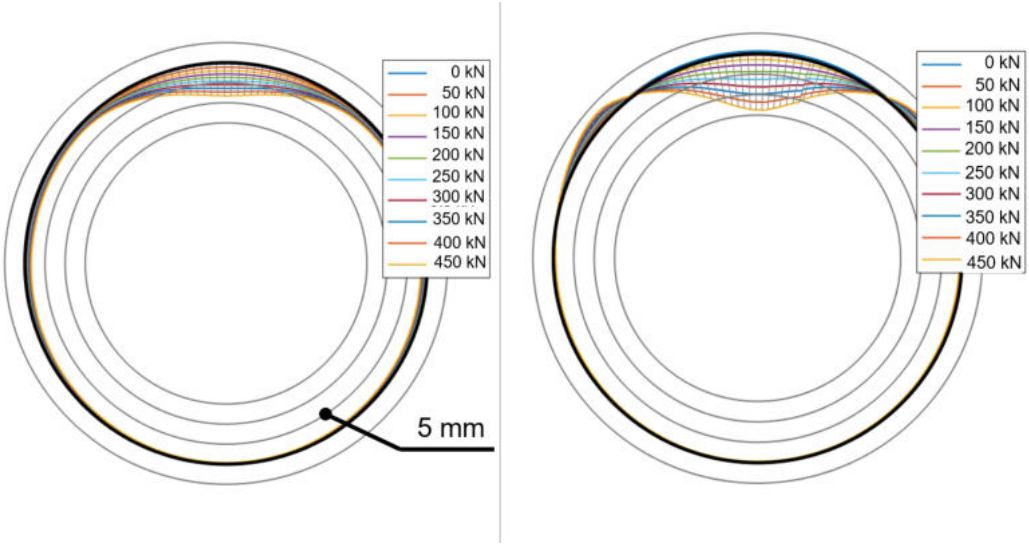

(a) Fully bedded. (b) Partially bedded.

Figure 106: Distribution of radial displacements in the middle of the first ring after the shield tail for each load step.

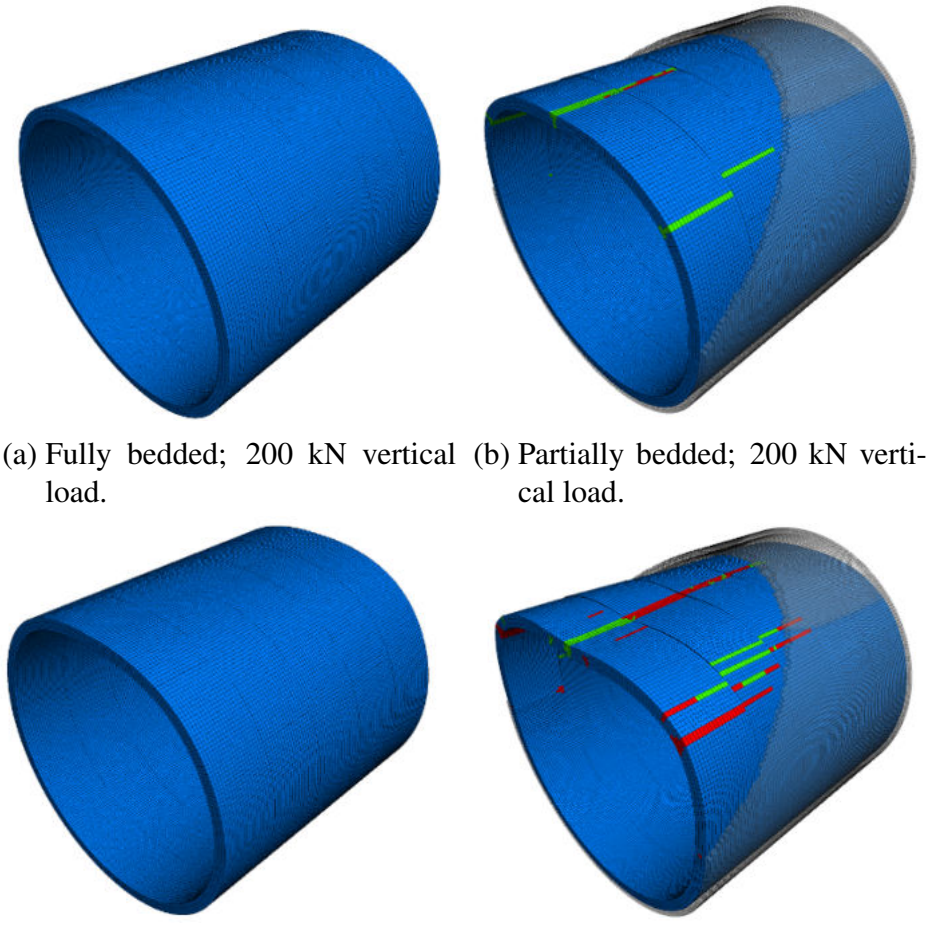

(a) Fully bedded; 200 kN vertical load. (b) Partially bedded; 200 kN vertical load.

(c) Fully bedded; 300 kN vertical load. (d) Partially bedded; 300 kN vertical load.

Figure 107: Crack development in the segmental lining; left: fully bedded; right: partially bedded (upscaled deformation).

6.3 Ovalization

In order to show the influence of the bedding improvements using geotextile tubes on the degree of ovalization, a more detailed model was created as described in the following.

6.3.1 Numerical model

By using again the FLAC^{3D} code the numerical model shown in Figure 108 was created. Due to the complex geometry and the joint configuration of the segmental lining, no symmetry axis could be introduced.

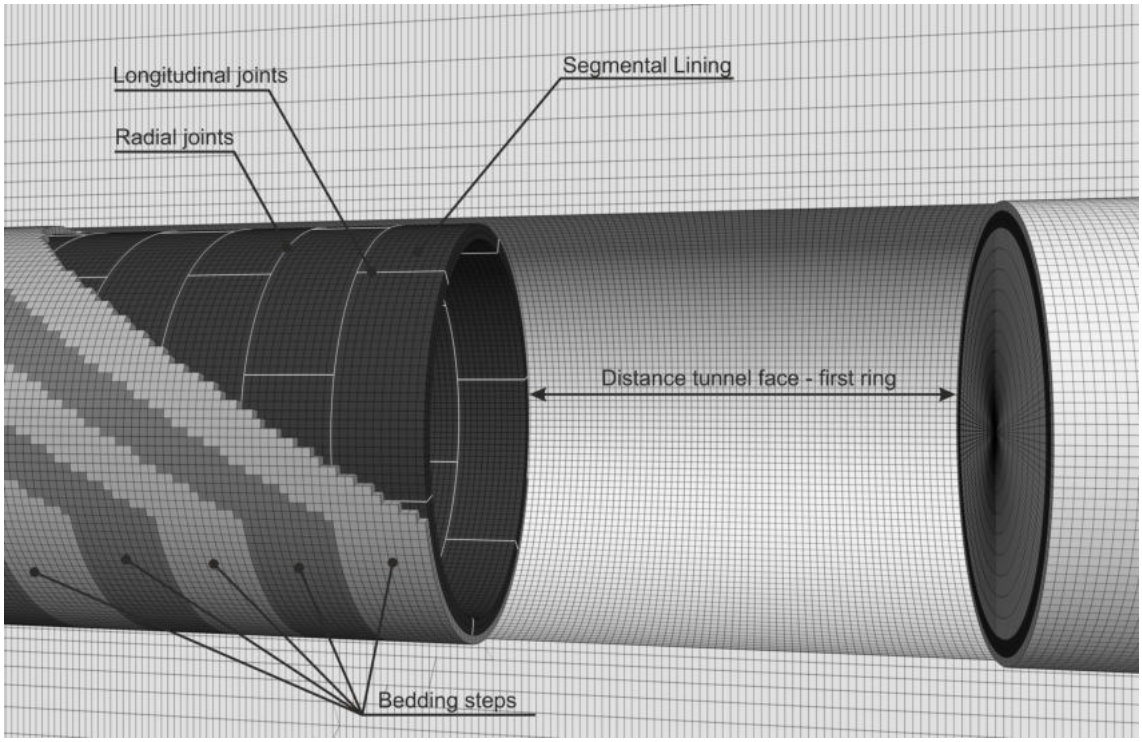

Figure 108: Numerical model for the simulation of the supported excavation.

In order to minimize the influence of the artificial model boundaries, the model dimensions have been chosen as large as possible. With an expansion factor of four times the excavation diameter, the interaction between the failure zone and the boundary could be reduced to a negligible extent. The model boundaries are illustrated in Figure 109

The lining segmentation and pattern used in the model correspond to the support applied at the site. Since shield jamming is not within the focus of the investigation, the TBM (shield) itself was not modelled. The segmental lining was installed 12 m behind the tunnel face according to the shield length on site.

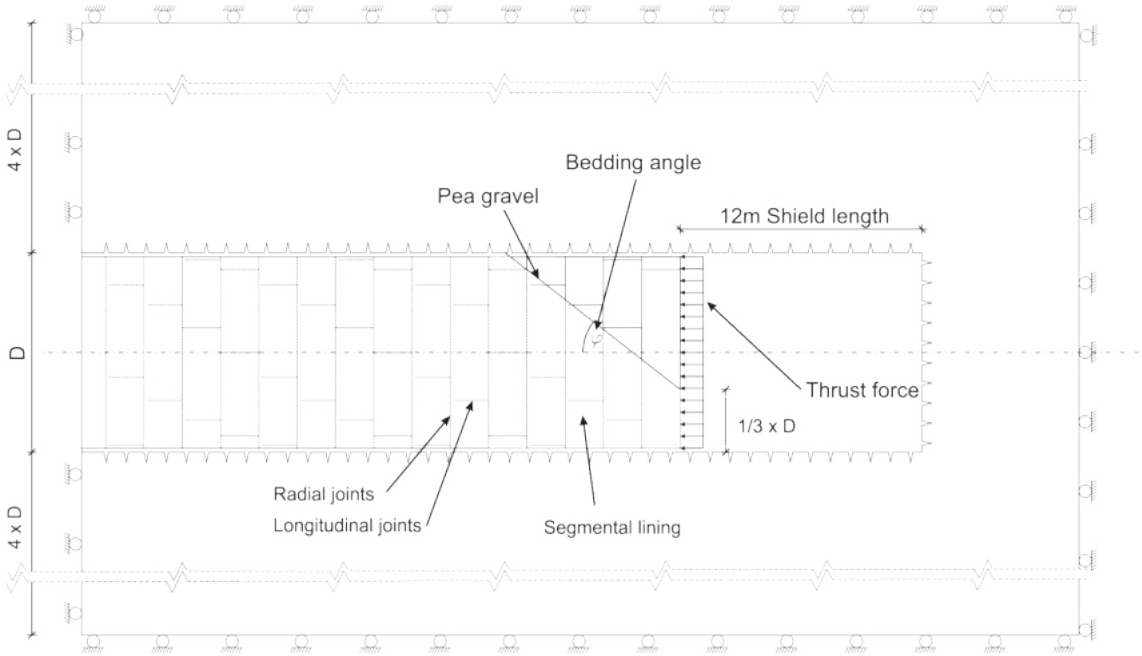

Figure 109: Model discretization and boundaries.

6.3.2 Overview of examined cases

All boundary conditions (dimensions, excavation process, geometry of support, support parameters) have been kept constant in order to qualitatively examine the influence of one ring of segments equipped with bedding tubes located at the center the numerical model.

Three scenarios have been simulated in order to capture the positive effect of the bedding improvements. Every scenario consists of two simulations with and without bedding improvements. Hence, six models have been considered as shown in Table 15. For all the simulations, gravity has been applied in vertical direction in order to account for the dead weight of the segments.

Table 15: Overview of numerical simulations

Series	Overburden [m]	In-situ stress ratio [-]	Geotextile tube	comment
1	1,000	1.0	No	-
2	1,000	1.0	Yes	-
3	1,000	0.5	No	-
4	1,000	0.5	Yes	-
5	954	individual	No	on site test
6	954	individual	Yes	on site test

6.3.2.1 Series 1 to 4

To illustrate the bedding effect, a reference case, series 1 to 4, with an overburden of 1,000 m and values for K_0 of 0.5 and 1 is considered in the following. The principal stresses are oriented vertically, in longitudinal direction of the tunnel and perpendicular to the tunnel axis. The rock mass parameters for the "Mohr – Coulomb" model adopted in the FLAC^{3D} code are listed in Table 16.

Table 16: Rock mass parameters for Series 1 to 4 for "Mohr – Coulomb" model.

Description	Unit	
Density	[g/cm^3]	2.75
Cohesion	[MPa]	2
Friction angle	[°]	35
Dilation angle	[°]	0.0
Tensile strength	[MPa]	0.5
Young's modulus	[MPa]	15,000
Poisson's ratio	[-]	0.15

6.3.2.2 Series 5 to 6

Table 17 summarizes the rock mass parameters for the on site bedding improvement test. To realistically simulate the rock mass, the "Ubiquitous Joint" model available in FLAC^{3D} was used. This model extends the "Mohr Coulomb" failure criterion with one anisotropy direction by means of different strength and deformability properties. The principal stresses were chosen and oriented according to the pressuremeter tests. The purpose of this model is to simulate the influence of foliation in the rock mass considered.

In the course of the exploration campaign for the given project, the at-rest horizontal earth pressure was determined by borehole pressuremeter tests. For the numerical evaluation, the in-situ measurement test results at a depth of 990 m have been used. The orientation of the principal stress directions, the tunnel axis and the foliation are provided in Table 18. The principal stress situation can be calculated with the provided gradient and the overburden for the given situation.

The numerical model considered an overburden of 954 m and a thrust force of 22 MN.

6.3.3 Results

Within the numerical study, several scenarios were simulated and the influence of the numerical eccentricity ε in relation to the distance to the initial lining installation was investigated. Hence, the methodology described in chapter 4 was applied.

Table 17: Rock mass parameters for Series 5 to 6 for “Ubiquitous Joint model”.

Description	Unit	
Density	[g/cm^3]	2.75
Cohesion	[MPa]	43
Friction angle	[°]	38
Dilation angle	[°]	0.0
Tensile strength	[MPa]	5
Young’s modulus	[MPa]	56,000
Poisson’s ration	[-]	0.15
Joint – Cohesion	[-]	17
Joint – Friction angle	[°]	30
Joint – Dilation angle	[°]	0
Joint – Tensile strength	[MPa]	0
Joint – Young’s modulus	[MPa]	56,000
Joint – Poisson’s ratio	[MPa]	0.15

Table 18: Primary stress orientation.

Element	Dip direction [°]	Dip angle [°]	Gradient [-]
maximum principal stress	140	00	1.67
intermediate principal stress	000	90	1.00
minimum principal stress	230	00	0.81
Tunnel axis	262	00	-
Foliation	133	36	-

The results were compared with the reference simulations, which are shown in Figure 110. These confirm the positive temporary bedding effect of the geotextile tubes, which counteracts the ovalization of the segmental lining.

The comparison of the individual bedded and unbedded cases draws a clear picture regarding the positive influence of the bedding improvements on the ovalization. It can be seen that higher lateral pressure coefficients lead to higher degrees of ovalization.

The unbedded case of the field test yields the highest degree of ovalization compared with the unbedded reference cases (red and blue). On the other hand, the bedded field test depicts lower ovalization degrees than the bedded reference cases. This effect can be attributed to the differing stress situation of the on-site test in comparison to the reference cases.

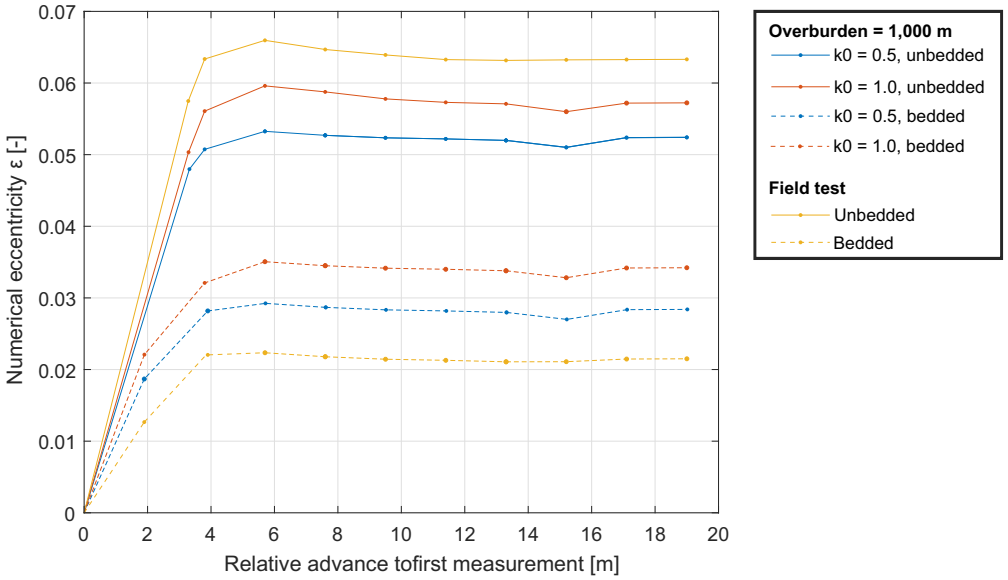

Figure 110: Comparison of numerical eccentricity of the different numerical simulations (the primary stress state of the field tests differs from the 1,000 m overburden case through orientation and value).

7 Conclusions

The backfill of the annular gap plays an important role within the support of Shield TBM driven tunnels. At present, only subordinate attention is given to this medium when it comes to the support – rock mass interaction.

With the literature review presented in chapter 2 it cannot be ignored, that the bedding represents the largest unknown quantity within the support of Shield TBM driven tunnels. The presented research gives an overall insight into the influence of the bedding immediately behind the shield tail.

An extensive laboratory and in-situ testing programme was carried out in order to investigate the elastic response of pea gravel. Hence, three different measurement procedures have been evaluated:

1. The large oedometer tests have shown that the deformability properties of pea gravel depend on the loading type as well as the load level. During primary loading, Young's moduli of approximately 80 MPa are obtained at a load level of 0.3 – 0.4 MPa while reloading and unloading show Young's moduli in the range 200 – 220 MPa and 300 – 420 MPa respectively.
2. An in-situ load plate test apparatus measuring the elastic response of pea gravel through the pea gravel injection openings in the lining segments was developed. The tests provided consistent and plausible results. Nevertheless, the results have to be evaluated with caution. The dependence of the loading type on the deformational behaviour could be confirmed. Compared with the large oedometer tests, the stress dependency is shown to be not as significant.
3. Standard load plate tests with a layer thickness of approximately 1 m lead to unsatisfactory results. This is attributed to the cohesionless character of pea gravel which is cause of instant excess of the shear strength. Hence, the unconfined deformation behaviour of pea gravel is characterised by a displacement of continuous soil bodies.

The ground penetrating radar (GPR) measurements on both an analogue model and in the tunnel itself have shown that it is possible to detect voids (absence of pea gravel) in the annular gap. An antenna frequency of 1,600 MHz has been found to be most suitable under the given boundary conditions. The age or the associated moisture content of the concrete of the segmental lining has a major influence on the data which can be obtained with the radar measurements. High moisture content leads to a strong damping of the radar waves and limits the reliability of the measurement results. The knowledge of the reinforcement allocation is required in advance. With a lateral reinforcement distance of 240 mm and a transverse reinforcement with a distance of approximately 160 mm, the measurement could

be carried out successfully. The segmental lining had a thickness of 35 cm. Further investigations are needed in order to be able to state the limitations of the GPR method regarding age of concrete, spacing of reinforcement, segment thickness and material characterization when evaluating the annular gap backfill.

With the presented scaled model tests the relocation process was confirmed qualitatively. Relationships between annular gap width, grain size and friction angle have been shown and quantified. The need for adding mortar in the invert area has been confirmed. In combination with the GPR measurements, the repose angle of pea gravel within the annular gap behind the shield tail was measured to be approximately 32°.

The displacement behaviour of a segmental ring can be described with the deviation from a circle in terms of numerical eccentricity of an ellipse. Displacement measurements have shown that the segmental lining undergoes a rigid body motion after leaving the shield tail with only slight angular distortions. The maximum numerical eccentricity increases with decreasing rock mass strength and spacing of the discontinuities.

Two bedding improvements have been developed. Geotextile bedding tubes, installed on the exterior surface of the lining segments, have been implemented onsite. Deformation measurements have shown that the ovalization represented by the numerical eccentricity can be reduced to an acceptable level. The filling and the resulting expansion of the geotextile tube results in a partition of the annular gap. The pea gravel is thereby prevented from relocating in longitudinal direction (rearrangement).

The presented research has shown, that the simulation of a segmental lining reinforcement using FLAC^{3D} (Itasca Consulting Group, 2017) can be implemented. The load redistribution in case of crack formation within the segments can be observed. The numerical simulations have shown that modelling of a segmental support using FLAC^{3D} provides plausible and interesting results. Although appearing as a trivial conclusion, the role of proper backfill must be properly addressed during the design stage. The results have shown that a proper backfilled annular gap decreases the maximum bending moments in the segmental lining and contributes to reduce the induced displacements. Furthermore the radial convergences decrease significantly with a more complete annular backfill. Crack propagation is more likely in uncomplete bedding situations. The results show that cracks within the support indicate a higher utilization but do not decrease the load capacity. Hence conclusions are drawn regarding a simple structural analysis according to ÖNORM EN 1992-1-1 (2015). The evaluation of the numerical eccentricity of the lining, with and without geotextile tubes as bedding improvement, was evaluated quantitatively for three cases. Two reference models and the remodelled field test have shown that the ovalization is significantly reduced with the bedding improvement.

The quantification of the influence of the bedding into the design of the lining is still a challenging task. Nevertheless, the findings within this thesis improve the assessment of the behaviour of pea gravel. The novel data and information provided in this thesis contribute to a better understanding of the behaviour of pea gravel.

It is stressed that the backfill as intermediate layer between rock mass and segmental lining is of great importance and a proper investigation is inevitable for appropriate support design. Common sense, simple and unpretentious design approaches and fundamental laboratory tests are required in order to improve segmental lining design.

Bibliography

Aggelis, D. G., Shiotani, T., & Kasai, K. (2008). Evaluation of grouting in tunnel lining using impact-echo. *Tunnelling and Underground Space Technology*, *23*(6), 629–637.

Ahrens, H., Lindner, E., & Lux, K.-H. (1982). Zur Dimensionierung von Tunnelausbauten nach den Empfehlungen zur Berechnung von Tunneln im Lockergestein (1980). *Die Bautechnik*, *59*(8), 260–273, 303–311.

Anagnostou, G. & Pimentel, E. (2012). Zu den Felsklassifikationen mit Indexwerten im Tunnelbau. *geotechnik*, *35*(2), 83–93.

Austrian Societey for Concrete- and Construction Technology (2011). Guideline Concrete Segmental Lining Systems.

Austrian Society for Geomechanics (2010). Guideline for the Geotechnical Design of Underground Structures with Conventional Excavation.

Austrian Society for Geomechanics (2014). *Geotechnical Monitoring in Conventional Tunnelling: Handbook*. Salzburg.

Austrian Standards Institut (2017). ÖNORM EN ISO 17892-5: Geotechnical investigation and testing - Laboratory testing of soil - Part 5: Incremental loading oedometer test.

Austrian Standards Institut (2018). +: 2018 05 01: Geotechnics - Soil investigation - Plate loading test (Static load plate test).

Bach, D., Fuchs, W., Lehner, W., & Obermeier, O. (2008). Tunnelkette Perschling - Reiserbergtunnel and Stierschweiffeldtunnel: TBM Success under Difficult Ground Conditions. *Geomechanik und Tunnelbau*, *1*(6), 567–575.

Barton, N. (1999). TBM performance in rock using QTBM. *Tunnels & Tunnelling International*, *31*(9), 30–34.

Barton, N., Lien, R., & Lunde, J. (1974). Engineering classification of rock masses for the design of tunnel support. *Rock Mechanics Felsmechanik Mcanique des Roches*, *6*(4), 189–236.

Baumann, L. & Zischninsky, U. (1994). Neue Löse- und Ausbautechniken zur maschinellen Fertigung von Tunneln in druckhaftem Fels. *Felsbau*, *12*(1), 25–29.

Behnen, G., Fischer, O., & Hestermann, U. (2010). Technische Herausforderungen beim PPP Großprojekt CLEM7 in Australien. In Universität der Bundeswehr München und STUVA (Ed.), *Tagungsband zum „2. Münchener Tunnelbausymposium“*.

Behnen, G., Nevrly, T., & Fischer, O. (2012). Einfluss der Ringspaltverfüllung auf die Bemessung von Tunnelschalen. In *16. Münchener Massivbau Seminar*.

Behnen, G., Nevrly, T., & Fischer, O. (2013). Bettung von Tunnelschalen. In Deutsche Gesellschaft für Geotechnik e.V. DGGT (Ed.), *Taschenbuch für den Tunnelbau*. VGE Verlag.

Behnen, G., Nevrly, T., & Fischer, O. (2015). Soil-structure interaction in tunnel lining analyses. *geotechnik*, *38*(2), 96–106.

Benedikt, J., Lemmerer, J., Köpf, M., & Obermeier, O. (2016). Excavation of the Perschling Tunnels by TBM - expectations and reality - lessons learned / TBM-Vortrieb Tunnelkette Perschling - Erwartung und Wirklichkeit - Erfahrungen und Erkenntnisse. *Geomechanics and Tunnelling*, *9*(5), 580–594.

Billig, B., Ebsen, B., Gipperich, C., Schaab, A., & Wulff, M. (2007). DeCo-Grout - innovative grout to cope with rock deformations in TBM-tunnelling. In Barták, J., Hrdina, I., Romancov, G., & Zlámal, J. (Eds.), *Underground Space - The 4th Dimension of Metropolises*, volume 2, (pp. 1487–1492)., Hoboken. Taylor and Francis.

Bonart, T. & Bär, J. (2018). *Quantitative Betriebswirtschaftslehre, Band I: Grundlagen, Operations Research, Statistik*. Wiesbaden: Springer Gabler.

Boussinesq, J. (1885). *Application des potentiels à l'étude de l'équilibre et du mouvement des solides élastiques*. Paris: Gauthier-Villars.

Brunar, g. & Powondra, F. (1985). Nachgiebiger Tübbingausbau mit Meypo-Stauchelementen. *Felsbau*, *3*(4), 225–229.

Bull, A. (1946). Stresses in the Linings of Shield-Driven Tunnels. *Transactions of the American Society of Civil Engineers*, *111*(1), 443–474.

Cantieni, L. & Anagnostou, G. (2009). The interaction between yielding supports and squeezing ground. *Tunnelling and Underground Space Technology*, *24*(3), 309–322.

Cheng, Z. & Detournay, C. (2016). Plastic hardening model I: Implementation in FLAC3D. In Itasca International, I. (Ed.), *APPLIED NUMERICAL MODELING IN GEOMECHANICS - 2016*, (pp. 267–276)., Minneapolis.

Daller, J., Diewald, M., Lemmerer, J., & Zwittnig, G. (2016). Expectations and reality of the mechanised tunnel drives for the Wienerwald Tunnel / Erwartung und Wirklichkeit der TBM-Vortriebe am Wienerwaldtunnel. *Geomechanics and Tunnelling*, *9*(5), 547–555.

Dehn, F. (2003). Herstellung, Verarbeitung und Qualitätssicherung von UHPC. In M. Schmidt & E. Fehling (Eds.), *Ultra-hochfester Beton*, Schriftenreihe Baustoffe und Massivbau (pp. 37–47). Kassel: Kassel Univ. Press.

Deutsche Gesellschaft für Erd- und Grundbau (1980). Empfehlungen zur Berechnung von Tunneln im Lockergestein. *Die Bautechnik*, *57*(10), 349–356.

Distelmeier, H. (1975). Montage von Stahlbetontübbings bei Tunnelbauten mit Schildvortrieb. *Beton- und Stahlbetonbau*, *70*(5), 120–125.

Duncan, J. M. & Chang, C.-Y. (1970). Nonlinear Analysis of Stress and Strain in Soils. *Journal of the Soil Mechanics and Foundations Division*, *96*(5), 1629–1653.

Farmer, I. W. (1975). Stress distribution along a resin grouted rock anchor. (12), 347–351.

Fischer, O., Nevrly, T., Behnen, G., Schmidt-Thrö, G., & Schmidt-Thrö, G. (2013). Fertigteile im Tunnelbau. In K. Bergmeister, F. Fingerloos, & J.-D. Wörner (Eds.), *Beton-Kalender 2014*, Beton-Kalender. Berlin: Ernst, Wilhelm & Sohn.

Gamper, C., Knapp, M., & Fiest, T. (2009). Jenbach Tunnel - a shallow hydroshield drive. *Geomechanik und Tunnelbau*, *2*(5), 494–501.

Gehring, K. (1995). Leistungs- und Verschleißprognose im maschinellen Tunnelbau. *Felsbau*, *13*(6), 439–448.

German Tunnelling Committee. Recommendations for the design, production and installation of segmental rings.

Grandori, R. & Antonini, F. (1994). Double Shield TBM Excavation Technique. *Felsbau*, *12*(6), 490–494.

Grübl, F. (1998). Einschaliger Tunnelausbau mit Stahlbetontübbingen - Welche lasten sind maßgebend, wie kann man Schäden vermeiden? In Deutsche Gesellschaft für Geotechnik e.V. DGGT (Ed.), *Taschenbuch für den Tunnelbau*.

Hain, H. (1968). *Zur Stabilität elastisch gebetteter Kreisringe und Kreiszylinderschale*. PhD thesis, Technische Universität Hannover, Hannover.

Hain, H. & Falter, B. (1975). Stabilität von biegesteifen oder durch Momentgelenke geschwächten und auf der Außenseite ealstisch gebetteten Kreisringen unter konstanten Außendruck. *Straße Brücke Tunnel*, (4), 98–105.

Haws, E. T. & Mackenzie, C. (1979). GB 2013757 A.

Henzinger, M. R., Lange, A., Volkmann, G. M., Moritz, B. A., & Schubert, W. (2018). Bedding improvement of lining segments using geotextile tubes. *Geomechanics and Tunnelling*, *11*(5), 589–598.

Henzinger, M. R., Pejić, D., & Schubert, W. (2017). Design Improvements of Segmental Linings Due to Unfavorable Bedding Situations. *Procedia Engineering*, *191*, 729–734.

Henzinger, M. R., Radončić, N., Moritz, B. A., & Schubert, W. (2016). Backfill of segmental lining - State of the art, redistribution behaviour of pea gravel, possible improvements / Tübbingbettung - Stand der Technik, Umlagerungsverhalten von Perlkies, Verbesserungspotenzial. *Geomechanics and Tunnelling*, *9*(3), 188–199.

Henzinger, M. R., Willmes, M., Lagger, M., Kathage, A. F., Moritz, B. A., & Schubert, W. (2018). Detection of voids in the annular gap using ground penetrating radar and determination of the in-situ deformation properties of pea gravel. *Geomechanics and Tunnelling*, *11*(3), 236–250.

Herrenknecht AG (2012). *PRODUKT PORTFOLIO: Pioneering Underground Technologies*. Schwanau, Germany: Corporate Communications Herrenknecht AG.

Hewett, B. & Johannesson, S. (1922). *Shield and Compressed Air Tunneling*. New York, USA: McGraw-Hill book Company, Incorporated.

ITA working group on general approaches to the design of tunnels (1988). Guidelines for the design of tunnels. *Tunnelling and Underground Space Technology*, *3*(3), 237–249.

Itasca Consulting Group, I. (2017). FLAC3D 6.0 — Fast Lagrangian Analysis of Continua in Three-Dimensions, Ver. 6.0.

Jol, H. M. (2009). *Ground penetrating radar: Theory and applications* (1. ed. ed.). Amsterdam: Elsevier.

Karlovsek, J., Scheuermann, A., & Willimas, D. J. (2012). Investigation of voids and cavities in bored tunnels using GPR. In *2012 14th International Conference on Ground Penetrating Radar (GPR)*, (pp. 496–501).

Kathage, A. F. (2016). Prinzipielle Modellierung von lokalen Defekten in der Ummantelung von Tübbingen mit dem Ray-Tracing- und dem FD-Verfahren für die Georadar-Antennen-Frequenzen 1600 MHz, 1000 MHz, 900 MHz sowie 400 MHz.

Knödel, K., Krummel, H., & Lange, G. (2005). *Handbuch zur Erkundung des Untergrundes von Deponien und Altlasten: Geophysik (German Edition)* (2nd ed. ed.). Dordrecht: Springer.

König, G., Tue, N. V., & Schenck, G. (2008). *Grundlagen des Stahlbetonbaus: Einführung in die Bemessung nach DIN 1045-1* (3., aktualisierte Aufl. ed.). Bauwesen. Wiesbaden: Vieweg + Teubner.

Kovári, K. (1998). Tunnelling in squeezing rock. *Tunnel*, *17*(5), 12–31.

Lagger, M. (2016). *Entwicklung einer Messvorrichtung zur Ermittlung der Verformungseigenschaften von Perlkiesverfüllungen*. Master Thesis, Graz University of Technology, Graz.

Lalagüe, A. (2015). *Use of Ground Penetrating Radar for Transportation Infrastructure Maintenance*. Doctoral Thesis, NTNU Trondheim, Trondheim.

Lalagüe, A., Lebens, M. A., Hoff, I., & Grøv, E. (2016). Detection of Rockfall on a Tunnel Concrete Lining with Ground-Penetrating Radar (GPR). *Rock Mechanics and Rock Engineering*, *49*(7), 2811–2823.

Lamé, G. (1852). *Leçons sur la théorie mathématique de l'élasticité des corps solides*. Paris: Bachelier.

Lammer-Stecher, J. (2017). *Anwendung von geophysikalischen Messmethoden zur Überprüfung der Ringspaltverf¨ullung mittels Perlkies*. Master Thesis, Graz University of Technology, Graz.

Lenk, K. (1931). *Der Ausgleich des Gebirgsdruckes in großen Teufen beim Berg- und Tunnelbau*. Berlin, Heidelberg: Springer Berlin Heidelberg.

Leonhardt, F. & Reimann, H. (1965). Betongelenke: Versuchsbericht, Vorschläge zur Bemessung und konstruktiven Ausbildung. *Deutscher Ausschuss für Stahlbeton (DAfStb)*, (Heft 175).

Maidl, B. (2008). *Hardrock tunnel boring machines*. Berlin: Ernst & Sohn.

Maidl, B., Herrenknecht, M., Maidl, U., Wehrmeyer, G., & Sturge, D. (2013). *Mechanised Shield Tunnelling* (2nd ed. ed.). Hoboken: Wiley.

Meldner, V. (1975). Zur Statik der Tunnelauskleidungen mit Stahlbetontübbings. *100 Jahre Wayss & Freytag*, 231–237.

Mezger, F., Ramoni, M., & Anagnostou, G. (2018). Options for deformable segmental lining systems for tunnelling in squeezing rock. *Tunnelling and Underground Space Technology*, *76*, 64–75.

Mezger, F., Ramoni, M., Anagnostou, G., Dimitrakopoulos, A., & Meystre, N. (2017). Evaluation of higher capacity segmental lining systems when tunnelling in squeezing rock. *Tunnelling and Underground Space Technology*, *65*, 200–214.

Moritz, A. B. (1999). *Ductile Support System for Tunnels in Squeezing Rock*. Doctoral Thesis, Technische Universität Graz, Graz.

Moritz, B. (2011a). Yielding elements - requirements, overview and comparison / Stauchelemente - Anforderungen, Überblick und Vergleich. *Geomechanics and Tunnelling*, *4*(3), 221–236.

Moritz, B. (2011b). Yielding elements - requirements, overview and comparison / Stauchelemente - Anforderungen, Überblick und Vergleich. *Geomechanics and Tunnelling*, *4*(3), 221–236.

Muir Wood, A. M. (1975). The circular tunnel in elastic ground. *Geotechnique*, *25*(1), 115–127.

Österreichische Gesellschaft für Geomechanik (2013). Richtlinie für die geotechnische Planung von Untertagebauten mit kontinuierlichem Vortrieb.

Österreichische Vereinigung für Beton- und Bautechnik (2009). Richtlinie Schildvortrieb.

Österreichisches Normungsinstitut (1978). ÖNORM B 4416: 1978 06 01.

Österreichisches Normungsinstitut (2005). ÖNORM B 2203-2: 2005-01-01: Untertagebauarbeiten - Werkvertragsnorm Teil 2: Kontinuierlicher Vortrieb.

Österreichisches Normungsinstitut (2014). ÖNORM EN 12620: 2014 02 15: Gesteinskörnungen für Beton.

Österreichisches Normungsinstitut (2015). ÖNORM EN 1992-1-1: 2015-02-15: Eurocode 2: Bemessung und Konstruktion von Stahlbeton- und Spannbetontragwerken.

Palmstrom, A. & Broch, E. (2006). Use and misuse of rock mass classification systems with particular reference to the Q-system. *Tunnelling and Underground Space Technology*, *21*(6), 575–593.

Peck, R. B. (1969). Advantages and Limitations of the Observational Method in Applied Soil Mechanics. *Géotechnique*, *19*(2), 171–187.

Pejić, D. (2016). *Duktile Ausbauelemente zur unmittelbaren Tübbingbettung*. Master Thesis, Graz University of Technology, Graz.

Pilgerstorfer, T. (2014). *Mechanical Characterization of Fault Zones*. Doctoral Thesis, Graz University of Technology, Graz.

Podjadtke, R. & Weidig, G. (2010). Adjustable flexible segment lining. *Tunnelling and Underground Space Technology*, *29*(7), 37–42.

Preschan, M. (2018). *Radial bedding of segmental linings at shield TBM driven tunnels*. Master Thesis, Graz University of Technology, Graz.

Rabcewicz, L. (1944). *Gebirgsdruck und Tunnelbau*. Wien: Springer.

Radončić, N. (2011). *Tunnel design and prediction of system behaviour in weak ground*. Doctoral Thesis, Graz University of Technology, Graz.

Schanz, T., Vermeer, P. A., & Bonnier, P. G. (1999). The hardening soil model: Formulation and verification. *Beyond 2000 in Computational Geotechnics - 10 Years of PLAXIS*.

Schneider, E., Rotter, K., Saxer, A., & Röck, R. (2005). COMPEX SUPPORT SYSTEM - A new method for driving tunnels through zones of squeezing rock with shielded TBMs and subsequent segment-lining. *Felsbau*, *23*(5).

Schneider, E. & Spiegl, M. (2010). Nachgiebiger Ausbau für druckhaftes Gebirge: Gestern – Heute – Morgen Lösungen für den Brenner-Basistunnel. *Brenner Base Tunnel and Access Routes, Brenner Congress*, 64–67.

Schubert, W. (1996). Dealing with squeezing conditions in Alpine tunnels. *Rock Mechanics and Rock Engineering*, *29*(3), 145–153.

Schultze, E. & Muhs, H. (1967). *Bodenuntersuchungen für Ingenieurbauten* (Zweite völlig neubearbeitete und erweiterte Auflage ed.). Berlin, Heidelberg and s.l.: Springer Berlin Heidelberg.

Schulze, H. & Duddeck, H. (1964a). Spannungen in schildvorgetriebenen Tunneln. *Beton- und Stahlbetonbau*, *8*(59), 169–176.

Schulze, H. & Duddeck, H. (1964b). Statische Berechnung schildvorgetriebener Tunnel. In *Beton- und Monierbau, Aktien-Gesellschaft: 1889 - 1964* (pp. 87–114). Düsseldorf.

Seeber, G. (1999). *Druckstollen und Druckschächte: Bemessung - Konstruktion - Ausführung*. Stuttgart u.a.: Enke im Georg Thieme Verl.

St. John, C. M. & van Dillen, D. E. (1983). ROCKBOLTS: A NEW NUMERICAL REPRESENTATION AND ITS APPLICATION IN TUNNEL DESIGN. *Proceedings - Symposium on Rock Mechanics*, 13–25.

Strohäusl, S. (1996). Eureka Contun: TBM tunnelling with high overburden. *Tunnels & Tunnelling*, *28*(5), 41–43.

The British Tunnelling Society (2004). *Tunnel lining design guide* (1. publ ed.). London: Thomas Telford Ltd.

Thielicke, W. & Stamhuis, E. J. (2014). PIVlab - Time-Resolved Digital Particle Image Velocimetry Tool for MATLAB (version: 1.35).

Thienert, C. & Pulsfort, M. (2011). Segment design under consideration of the material used to fill the annular gap. *Geomechanics and Tunnelling*, *4*(6), 665–680.

Vigl, A. (2000). Honeycomb Segmental Tunnel Linings - Simple, Econpomical, Successful. *Felsbau*, *18*(6), 24–31.

Vigl, A. (2003). TBM Support in Squeezing Rock - A Convergence-Compatible Segmental Lining System. *Felsbau*, *21*(6), 14–18.

Vigl, A., Gütter, W., & Jäger, M. (1999). Doppelschild-TBM - Stand der Technik und Perspektiven. *Felsbau*, *17*(5), 475–485.

Vigl, A., Schubert, W. Posch, P., Walter, A., & Blümel, M. (2007). Investigations for a Convergence Compatible Lining System. *Flesbau*, *25*(6), 48–53.

Wagner, H. (1964). Beton- und Stahlbetontübbings im Tunnelbau. *Beton- und Stahlbetonbau*, *59*(2,3), 35–42, 56–60.

Warren, C., Giannopoulos, A., & Giannakis, I. (2016). gprMax: Open source software to simulate electromagnetic wave propagation for Ground Penetrating Radar. *Computer Physics Communications*, *209*, 163–170.

Weber, W. (2003). State-of-the-art Double-Shield-Technology is Released in Spain. *Felsbau*, *21*(6), 28–33.

Wieser, P. (2011). *Design of a Large Oedometer for the Determination of Stress Dependent Moduli on Fault Rocks*. Master Thesis, Graz University of Technology, Graz.

Willmes, M. (2018). Prüfbericht: Hohlraumortung Tübbinge.

Windels, R. (1966). Spannungstheorie zweiter Ordnung für den teilweise gebetteten Kreisring. *Die Bautechnik*, *43*(8), 265–274.

Wissmann, W. (1968). Zur statischen Berechnung beliebig geformter Stollen- und Tunnelaushleidungen mit Hilfe von Stabwerkprogrammen. *Der Bauingenieur*, *43*(1), 1–8.

Working Group No. 2, International Tunnelling Association (2000). Guidelines for the design of shield tunnel lining. *Tunnelling and Underground Space Technology*, *15*(3), 303–331.

Xie, X., Liu, Y., Huang, H., Du, J., Zhang, F., & Liu, L. (2007). Evaluation of grout behind the lining of shield tunnels using ground-penetrating radar in the Shanghai Metro Line, China. *Journal of Geophysics and Engineering*, *4*(3), 253–261.

Zhang, F., Xie, X., & Huang, H. (2010). Application of ground penetrating radar in grouting evaluation for shield tunnel construction. *Tunnelling and Underground Space Technology*, *25*(2), 99–107.

Zwittnig, G., Diewald, M., & Hechenblaickner, K. (2008). TBM Wienerwald Tunnel - Steps towards Successful Tunnelling. *Geomechanik und Tunnelbau*, *1*(6), 558–566.

List of Figures

List of Tables